Elastic-Wavefield Seismic Stratigraphy: A New Seismic Imaging Technology

Final Report

DOE Contract: DE-FC26-03NT15396

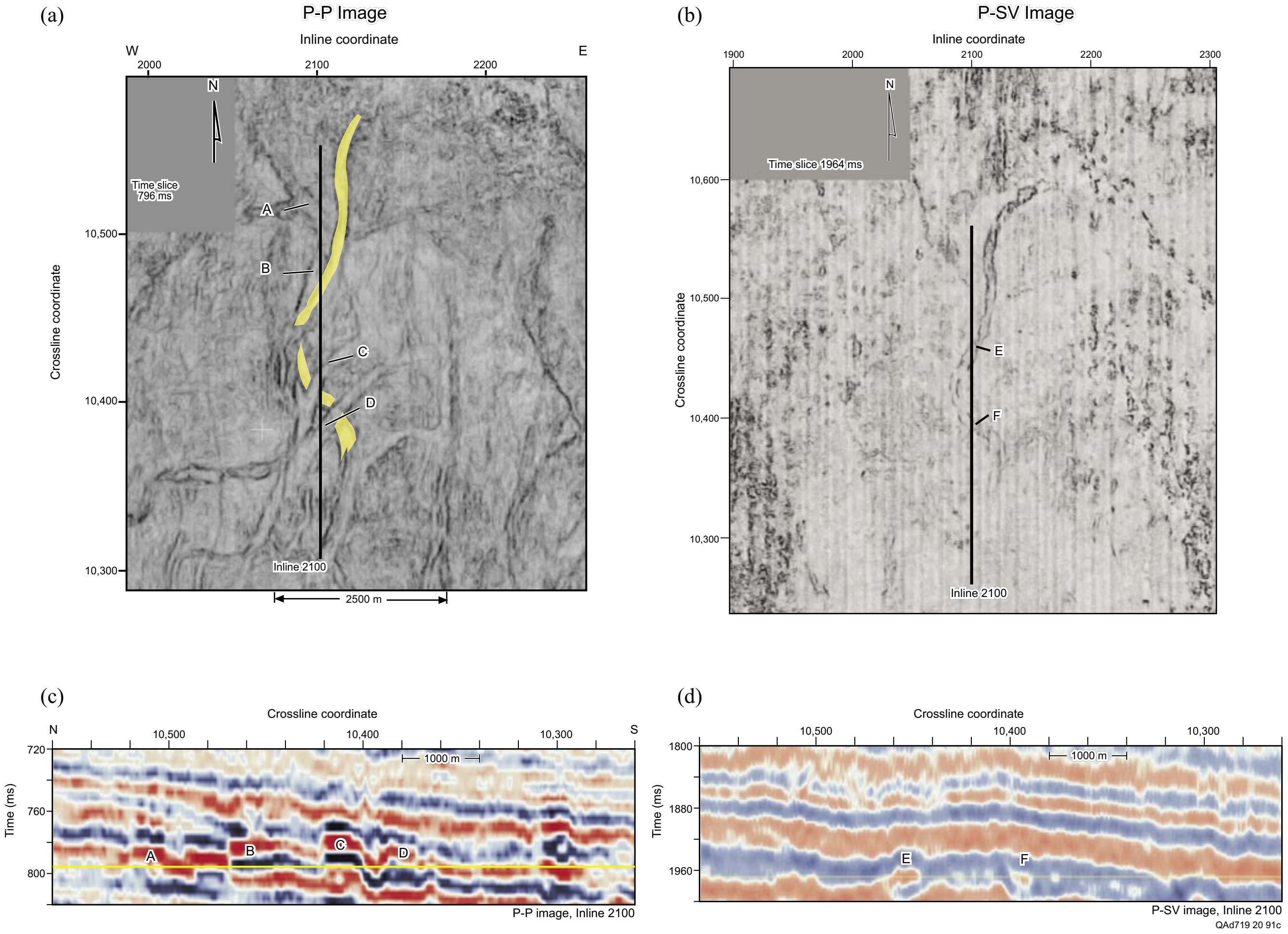

Submitted by:

Bureau of Economic Geology
The University of Texas at Austin
Austin, TX 78713-8924

August 1, 2003–July 31, 2006

Research team: Bob A. Hardage (Principal Investigator), Milo M. Backus, Michael V. DeAngelo, Sergey Fomel, Khaled Fouad, Robert J. Graebner, Paul E. Murray, Randy Remington, and Diana Sava

Disclaimer

Abstract

The purpose of our research has been to develop and demonstrate a seismic technology that will provide the oil and gas industry a better methodology for understanding reservoir and seal architectures and for improving interpretations of hydrocarbon systems. Our research goal was to expand the valuable science of seismic stratigraphy beyond the constraints of compressional (P-P) seismic data by using all modes (P-P, P-SV, SH-SH, SV-SV, SV-P) of a seismic elastic wavefield to define depositional sequences and facies. Our objective was to demonstrate that one or more modes of an elastic wavefield may image stratal surfaces across some stratigraphic intervals that are not seen by companion wave modes and thus provide different, but equally valid, information regarding depositional sequences and sedimentary facies within that interval. We use the term *elastic wavefield stratigraphy* to describe the methodology we use to integrate seismic sequences and seismic facies from all modes of an elastic wavefield into a seismic interpretation.

We interpreted both onshore and marine multicomponent seismic surveys to select the data examples that we use to document the principles of elastic wavefield stratigraphy. We have also used examples from published papers that illustrate some concepts better than did the multicomponent seismic data that were available for our analysis. In each interpretation study, we used rock-physics modeling to explain how and why certain geological conditions caused differences in P and S reflectivities that resulted in P-wave seismic sequences and facies being different from depth-equivalent S-wave sequences and facies across the targets we studied.

Contents

Disclaimer ii
Abstract iii
Abbreviations, Acronyms, and Glossary vii
Introduction 1
Executive Summary 1

Principles

Seismic Reflections and Chronostratigraphic Surfaces 2
Key Concept: Seismic Sequences 6
Time-Rock Stratigraphy 8
Key Concept: Seismic Facies 9
Stratal Slicing 11
Depth Registration of P and S Data 17
    Option 1: Multicomponent VSP Data 17
    Option 2: Map and Section Views of Stratigraphy 18
    Option 3: Numerical Registration of P and S Images 21
P and S Polarization Vectors and Reflectivity 23

Data Examples

Low-Porosity Carbonate System 25
    P and S Sequences and Facies 25
    Rock Physics 31
Fizz-Gas and Commercial-Gas Sandstone Reservoirs 39
    P and S Sequences and Facies 39
    Rock Physics 42
Fracture Systems 46
    P and S Sequences and Facies 46
    Rock Physics 53
Deep-Water, Near-Seafloor Geology 56
    P and S Sequences and Facies 56
    Rock Physics 62
Deep Geology: Northern Shelf of the Gulf of Mexico 65
    P and S Sequences and Facies 65
    Rock Physics 71
Class II Reservoirs 74
    P and S Sequences and Facies 75
    Rock Physics 77
Gas-Charged Sediments 78
    P and S Sequences and Facies 79
        Lithified and stratified sediment 79
        Mobilized sediment 80

Rock Physics 80
Conclusion 81
Acknowledgments... 82
References 82

List of Figures

1. Distinction between chronostratigraphic and lithostratigraphic surfaces 2
2. Chronostratigraphic Earth model 3
3. Synthetic seismic response: target overlap = seven wavelengths 4
4. Synthetic seismic response: target overlap = five wavelengths 4
5. Synthetic seismic response: target overlap = two wavelengths 5
6. Seismic sequence interpretation 7
7. Concept of XYZ seismic facies mapping 10
8. Contrast between vertical viewing and horizontal viewing 12
9. Distinctions among time slices, horizon slices, and stratal slices 13
10. Stratal surfaces across a vertical slice 14
11. Examples of stratal-slice amplitude attributes 16
12. Multicomponent VSP images of Morrow targets 19
13. Map and section views of P-P and P-SV thin-bed stratigraphy 20
14. Numerical depth registration of P-P and P-SV images 22
15. Displacements of a layered medium 23
16. Comparison of P-P and S-S reflectivities 24
17. Location of West Texas 3C3D seismic survey 26
18. P-P and P-SV structure maps of Strawn Formation 27
19. Strawn P-P and P-SV seismic amplitude facies 28
20. Strawn well log cross section 29
21. Reflection waveshape used as a seismic facies 30
22. Contrast of P-P and P-SV images across the Wolfcamp 31
23. Photographs of Strawn cores 32
24. Photographs of Strawn cores 34
25. V_P and V_S well log data across low-porosity carbonates 35
26. Well log data converted to averaged curves 36
27. P-P and P-SV reflectivities for fractured and unfractured carbonates 36
28. V_P, V_S, and ρ log data across the Wolfcamp Formation 38
29. P-P and P-SV reflectivities of Wolfcamp interval 39
30. Petrophysical model for commercial- and fizz-gas reservoirs 40
31. P-P and P-SV images across commercial-gas and fizz-gas reservoirs 42
32. P-P and P-SV images across commercial-gas and fizz-gas reservoirs 43
33. Fluid-substitution adjustments of log data 44
34. AVA behaviors for fizz- and commercial-gas reservoirs 45
35. P-P and P-SV azimuth-dependent velocities and reflectivities 47
36. Azimuths of maximum P-SV reflectivity from fracture intervals 49

37. S1 and S2 profiles 52
38. Fracture model for HTI medium 53
39. P and S reflectivities for HTI medium 54
40. Effects of fracture density and fracture fluid on reflectivities 55
41. Locations of deep-water study areas 56
42. P-P profile along OBC line 288 57
43. P-SV profile along OBC line 288 58
44. Detailed images of near-seafloor geology 60
45. Gas hydrate models 63
46. V_P and V_S for hydrate-bearing sediment 64
47. P-P and P-SV reflectivities for gas hydrate systems 65
48. Example 1 of P-P and P-SV images of deep geology 67
49. Example 2 of P-P and P-SV images of deep geology 68
50. Example 3 of P-P and P-SV images of deep geology 69
51. Example 4 of P-P and P-SV images of deep geology 70
52. Example 5 of P-P and P-SV images of deep geology 71
53. Two-layered, clay-content Earth model 72
54. Effect of clay content on AVA responses 73
55. P-P AVA responses of Class 1, 2, 3, and 4 reservoirs 75
56. P-P and P-SV profiles across Alba Field 76
57. Well log data across the Alba reservoir interval 77
58. P-P and P-SV AVA responses for Alba target 78
59. P-P and P-SV images across lithified, gas-saturated sediment 79
60. P-P and P-SV reflectivities for gas-charged sediments 81

List of Tables

1. Geologic interpretation of seismic facies patterns 9
2. Terms used to describe the internal form of seismic facies 11

Abbreviations, Acronyms, and Glossary

2D: 2-dimensional

3C: 3-component

3C3D: three-component and three-dimensional

4C: 4-component

9C: 9-component

AUV: Autonomous Underwater Vehicle. An unmanned vehicle that travels near the seafloor in great water depths and collects side-scan sonar, multibeam bathymetry, and chirp-sonar data.

AVA: amplitude-versus-angle, where angle = angle of incidence

bedding plane: a depositional surface created by a single, short-time-period, deposition of sediment. Geologic time can be assumed to be constant along a bedding plane.

chronostratigraphic surface: a depositional surface where geologic time is a fixed, constant value at every coordinate on the surface. Synonymous with **stratal surface** and **bedding plane**.

depositional sequence: a stratigraphic unit composed of a relatively conformable succession of genetically related strata and bounded at its top and base by unconformities or their correlative conformities. See **seismic sequence**.

detected: a geologic target is detected when seismic data indicate the presence of the target but do not allow its physical dimensions to be measured. See **resolved**.

diachronous reflection: a seismic reflection that cuts across stratal surfaces. Geologic time is not constant along a diachronous reflection.

elastic wavefield stratigraphy: a method of seismic interpretation based on the concept that any mode of a seismic wavefield may provide unique seismic sequence information and/or unique seismic facies information across some stratigraphic intervals that cannot be observed with other modes of the wavefield. See **seismic stratigraphy**.

facies: a unique aspect or recognizable property of an object. See **seismic facies**.

FMI: Formation Multi-Imager log

GOM: Gulf of Mexico

horizon slice: a surface that cuts through a seismic image at a constant image-time offset from a selected seismic reflection event. Contrast with **stratal slice**.

HTI medium: a medium having **horizontal transverse isotropy**, meaning the medium is isotropic when viewed in a direction transverse to a particular horizontal axis of symmetry. The properties of an HTI medium are used to describe vertical fractures.

lithostratigraphic surface: a depositional surface that has a constant rock type at every surface coordinate

OBC: ocean-bottom cable

P: P-wave

P-P: a seismic wave mode involving a downgoing P wave and an upgoing P wave

P-SV: a seismic wave mode involving a downgoing P wave and an upgoing SV wave

p.u.: porosity unit. A p.u. value of 10 equals a porosity of 10 percent.

P-wave wipeout zone: any portion of P-P image space where gas-charged sediment attenuates P-wave reflection signal to such an extent that P-P data can create no image.

resolved: a geologic target is resolved when seismic data allow a physical dimension of the target (either thickness or width) to be measured. See **detected**.

S: S-wave

S_W: water saturation

S1: fast-S shear mode

S2: slow-S shear mode

seismic facies: any seismic attribute that distinguishes one succession of seismic reflections from another succession of seismic reflections

seismic sequence: a succession of relatively conformable seismic reflections bounded by unconformable reflections or their correlative conformable reflections. See **depositional sequence**.

seismic stratigraphy: a method of seismic interpretation based on recognizing seismic sequences and seismic facies and using the spatial geometries, arrangements, and distributions of these sequences and facies to infer depositional environments and lithofacies patterns. See **elastic wavefield stratigraphy**.

SH-SH: a seismic wave mode involving a downgoing SH wave and an upgoing SH wave

stratal slice: a surface that cuts through a seismic image at a constant geologic-time offset from a selected seismic reflection. Contrast with **horizon slice**.

stratal surface: a depositional surface representing a fixed moment in geologic time. See **chronostratigraphic surface**.

SV-P: a seismic wave mode involving a downgoing SV wave and an upgoing P wave

SV-SV: a seismic wave mode involving a downgoing SV wave and an upgoing SV wave

time slice: a surface that cuts through a seismic image at a constant image-time coordinate

time warping: adjustment of the image-time coordinates of one elastic mode of a seismic wavefield to be depth equivalent to the image-time coordinates of another elastic mode of the same wavefield

unconformity: a break in sediment deposition caused by either a loss of section (erosion) or by a loss of geologic time (nondeposition)

V_P: P-wave velocity

V_S: S-wave velocity

XYZ Mapping: a seismic interpretation technique used in the early years of seismic stratigraphy practice to define and display seismic facies

Introduction

The principles of seismic stratigraphy form the basis of modern seismic data interpretation. Seismic stratigraphy was formalized as a science by researchers at Exxon and was made available to the public through Memoir 26 published in 1977 by the American Association of Petroleum Geologists (Payton, 1977). Following the publication of Memoir 26, an intense period of industry education focused on the concepts and applications of seismic stratigraphy in the late 1970's and into the 1980's. Several books were written to promote the science (Sheriff, 1980; Berg and Woolverton, 1985; Hardage, 1987), articles too numerous to cite were published to provide case histories, and short courses were held in many oil companies and among professional societies to implement seismic stratigraphy practice. As a result, the interpretational principles of seismic stratigraphy became the accepted methodology for interpreting seismic images of subsurface geology in the early 1980's, and the science of seismic stratigraphy is now widely and consistently practiced.

Literature searches show that the number of published papers on the topic of seismic stratigraphy number into the many hundreds, which is far too many citations to accumulate into a reference list. However, in our examination of this huge library of scientific writing, we found only a small number of papers that used S-wave seismic data in a seismic stratigraphy application. Until the mid-1990's, there appears to have been only five published papers that considered S-wave data in a classic seismic stratigraphy context (Meissner and Hegazy, 1981; Ensley 1984, 1985; McCormack and others, 1984, 1985). Slowly, a few more examples of S-wave seismic sequences and seismic facies are being inserted into the literature, but, in essence, seismic stratigraphy has to this point in time been exclusively a P-wave seismic technology. Our research expands seismic stratigraphy into the complete seismic elastic wavefield and removes the restriction that the science has to be limited to only the P-P seismic mode. We use the term ***elastic wavefield stratigraphy*** to describe the new seismic interpretation technology that we promote in this report.

Executive Summary

Our research envisions a new approach to seismic interpretation—an approach based on constructing reservoir and geologic models from all seismic elastic modes, not from just the P-P mode as has been done in conventional seismic stratigraphy for the past several decades. Research summarized in this report illustrates the value of elastic wavefield stratigraphy and will aid the hydrocarbon-exploration industry in transitioning from conventional P-P seismic stratigraphy to a more robust, multicomponent, seismic interpretation science. In our study, we have utilized multicomponent seismic data that were acquired across a variety of depositional targets to illustrate principles that we think are important. We make no claim that we have covered all of the key principles and applications that need to be documented. We view our work as a foundation from which we and others can expand this investigation, develop additional case histories, and lead the oil and gas industry toward a new seismic interpretation science.

Principles

Seismic Reflections and Chronostratigraphic Surfaces

A ***chronostratigraphic surface*** is a stratigraphic surface that was deposited at a fixed geologic time. In our usage, the term chronostratigraphic surface is synonymous with ***stratal surface*** and ***bedding plane***. Geologic time is constant along a chronostratigraphic surface; rock type is not. A chronostratigraphic surface may transgress different rock types, but it cannot cut across geologic time lines.

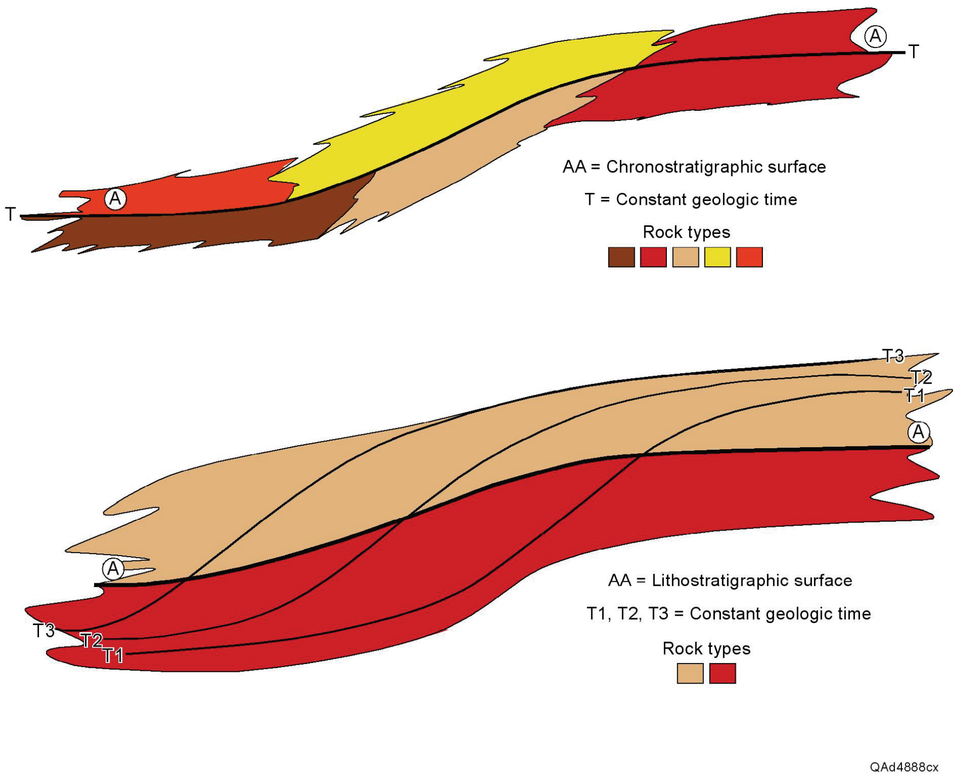

Figure 1. Distinction between a chronostratigraphic surface (top) and a lithostratigraphic surface (bottom). Geologic time is constant along a chronostratigraphic surface; rock type is not constant. Rock type does not change along a lithostratigraphic surface; geologic time does change.

In contrast, a ***lithostratigraphic surface*** is a *stratigraphic surface that defines a specific rock type*. Rock type is constant along a lithostratigraphic surface; geologic time is not. A lithostratigraphic surface may transgress geologic time lines, but it cannot cut across rock types. The diagrams in Figure 1 illustrate the distinctions between a chronostratigraphic surface and a lithostratigraphic surface.

A fundamental premise of seismic stratigraphy is that seismic reflections follow chronostratigraphic surfaces, not lithostratigraphic surfaces (Vail and others, 1977). This concept was hotly debated for a time but is now accepted as a basic principle of seismic interpretation. In 1993, Tipper published an intriguing paper in which the following question was posed and studied, *“Do seismic reflections necessarily image chronostratigraphic surfaces?”* (Tipper, 1993). The analysis presented by Tipper will be repeated so that some of the seismic phenomena that are illustrated in this report can be better appreciated.

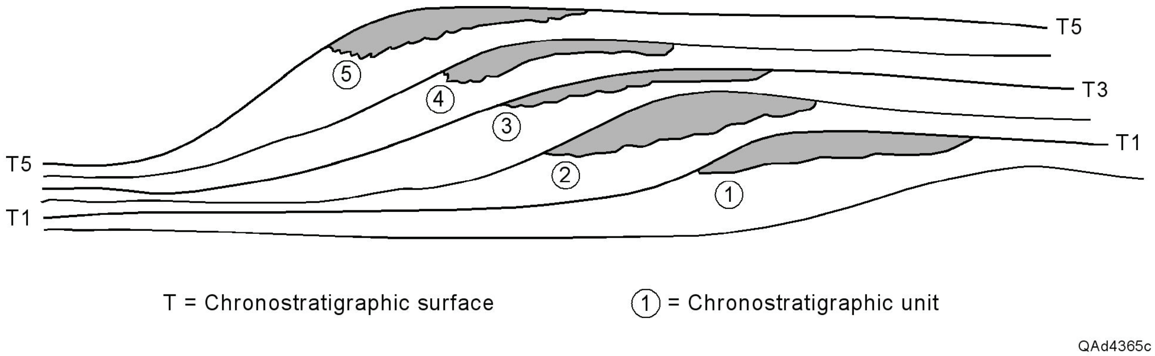

Figure 2. Chronostratigraphic Earth model: five stratigraphic targets (bodies 1 through 5) deposited at five geologic times, T1 through T5.

The stratigraphic model illustrated in Figure 2 will be used as a demonstration. This model shows five rock units deposited at five different geologic times—T1 through T5. These five rock units are shown in the top panels of Figures 3 through 5 as stacked, overlapping targets that are to be imaged. This five-layer stack is then illuminated with seismic wavelets having varying resolution properties.

In Figures 3 through 5, the left column shows the illumination created by a high-resolution wavelet, the center column uses a medium-resolution wavelet for the imaging, and the right column documents the image produced by a low-resolution wavelet. The illuminating wavelet is shown beside each five-layer model for easy comparison of wavelet length with target thickness and target spacing.

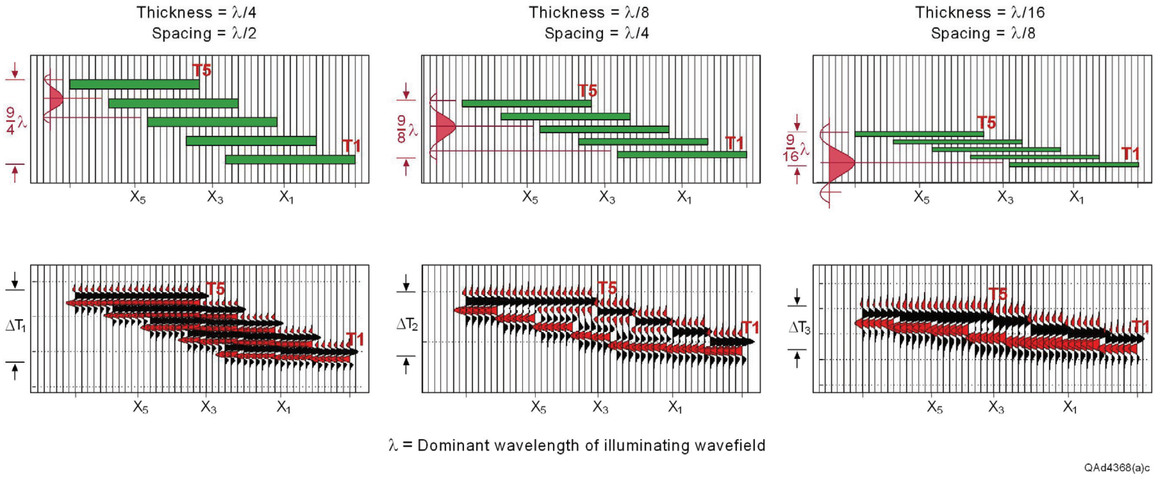

Figure 3. Top row: synthetic models approximating the Earth model in Figure 2. The dominant wavelength λ of each wavelet is the distance between the tic marks drawn on the side-lobe troughs of the wavelet. Bottom row: images produced by forward modeling using the wavelet shown beside each model (top). Here the lateral overlap from unit to unit is seven dominant wavelengths (7λ). X_5 marks the center of depositional unit 5 (Fig. 2); X_3, the center of depositional unit 3, and X_1, the center of unit 1. Labels T1 and T5 show the positions of depositional times T1 and T5 that are defined in Figure 2.

Model calculations are done in a dimensionless way in which key aspects of the model (bed thickness, bed spacing, and target overlap) are defined in terms of the dominant wavelength of the illuminating wavelet. This approach allows one person to think of the analysis as “the wavelet is the same in all cases, but the stratigraphic units have different thicknesses and spacings,” while another person can view the picture as “the target thicknesses and spacings are always the same, but the wavelet varies.” Either view is correct. Relationships between wavelet length, target thickness, and target spacing are defined at the top of each column of each figure. The amount of unit-to-unit overlap decreases as modeling proceeds from Figure 3 to Figure 5.

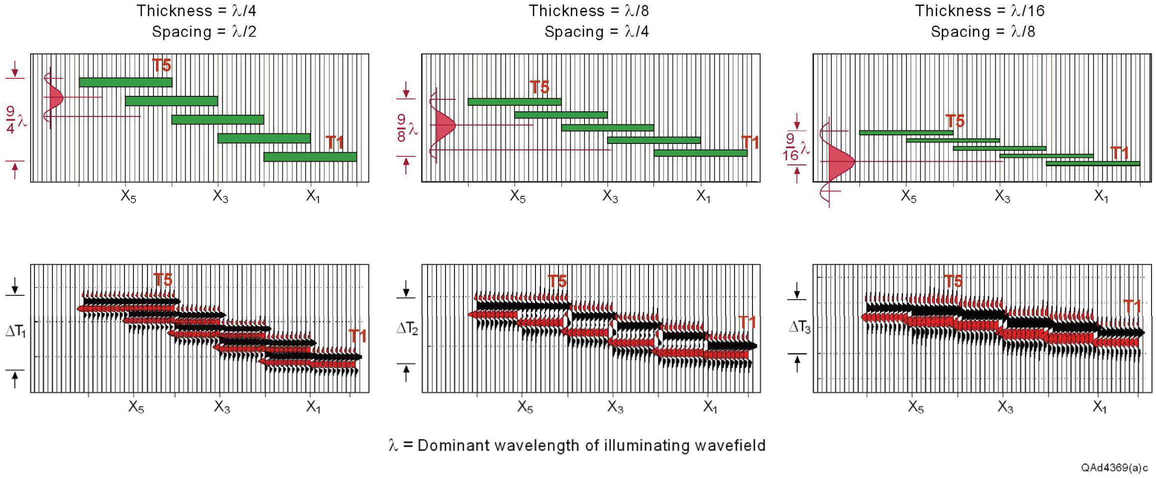

Figure 4. Same modeling exercise described in Figure 3 except the lateral overlap from unit to unit is decreased to five dominant wavelengths (5λ).

The dominant wavelength of each illuminating wavelet is the distance between the tic marks drawn on the two side-lobe troughs of the wavelets displayed along the top row of the models. Using λ to represent this dominant wavelength, we can illustrate some key points of this modeling:

1. When bed thickness is λ/4 or greater and bed spacing is λ/2 or more, there is an individual reflection event for each stratal surface T1 through T5 (left columns of each model). In this case, seismic reflections follow chronostratigraphic surfaces, and unit-to-unit relationships within the five-layer system can be interpreted from the seismic response.
2. When bed thickness is λ/16 or thinner and bed spacing is λ/8 or less (right columns of each model), the five-layer system is represented by a single, slightly erratic, peak/trough response that cuts across depositional time lines T1 through T5. In this case, the seismic response is a ***diachronous reflection*** that defines a lithostratigraphic surface, not a chronostratigraphic surface. We lose the ability to analyze the internal architecture of the layered system, and seismic reflections no longer follow stratal surfaces.
3. Between these two imaging options is the situation in the center column, where imaging indicates that a separate unit is positioned at each depositional time, T1 through T5, even though no image shows the correct lateral dimensions of the depositional bodies. The part of each unit that is overlapped by a younger unit is not imaged. Even though the imaging is not 100-percent correct, there is a reflection event for each chronostratigraphic surface. In this case, we can say that each image in the center columns consists of chronostratigraphic, but incomplete, seismic reflections.

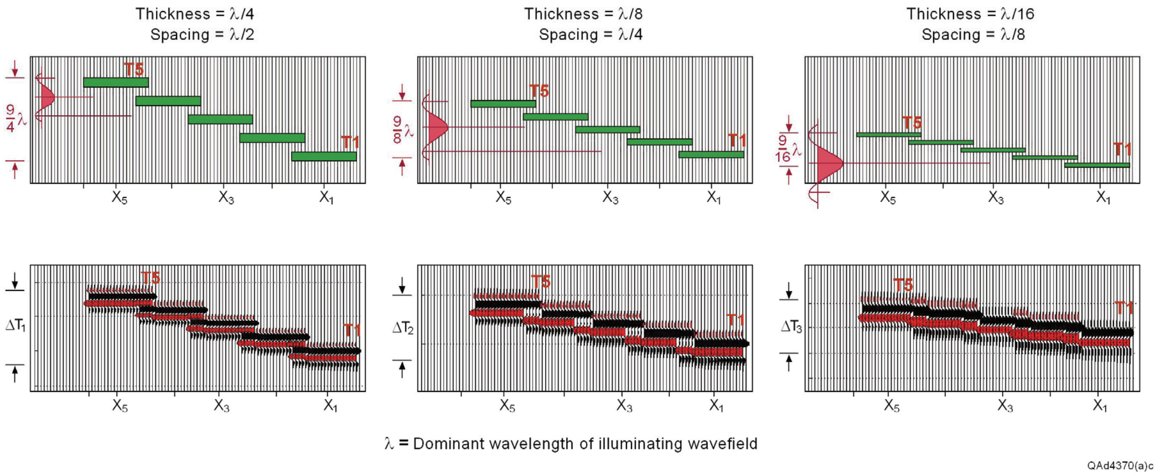

Figure 5. Same modeling exercise described in Figure 3 except the overlap of the units is decreased to two dominant wavelengths (2λ).

Whether seismic reflections follow chronostratigraphic surfaces thus depends on the relative magnitude of the dominant wavelength of the illuminating wavelet compared with the bed thickness deposited at each geologic time, the vertical spacing between successive chronostratigraphic surfaces, and the amount by which younger rock types overlap their older equivalents.

When multicomponent seismic data are processed, a processor's objective should be to produce the same basic wavelet in each elastic mode. If the P-P mode and all of its companion S-wave modes have the same basic wavelet, each mode will react to bed thickness, bed spacing, and target overlap in the same way, and differences in P and S sequences and facies can then be related directly to rock and fluid properties.

Unfortunately, it is not possible to always produce the same basic wavelet in all elastic-mode images created from a multicomponent seismic data set. In some instances, an S-wave basic wavelet will have a shorter dominant wavelength than its companion P-P wavelet, and in other situations, one or more of the S-wave modes (SH-SH, SV-SV, or P-SV) will have a basic wavelet with a longer dominant wavelength than the P-P mode. When there are differences in P and S basic wavelets, the modeling results in Figures 3 through 5 have to be considered. If P and S modes have basic wavelets with different dominant wavelengths, then differences in P and S sequences and facies are related to two causes:

1. fundamental differences in the way rock and fluid properties affect P and S reflectivities and
2. the manner in which each wavelet reacts to bed thickness, bed spacing, and target overlap.

In elastic wavefield stratigraphy, interpreters need to be able to segregate the effects of these two possibilities so that the influences of rock and fluid properties on P and S data are not confused with the interactions of different P and S basic wavelets with a layered stratigraphy. This challenge is not always easy to overcome.

Key Concept: Seismic Sequences

A ***depositional sequence*** is defined as, *"a stratigraphic unit composed of a relatively conformable succession of genetically related strata and bounded at its top and base by unconformities or their correlative conformities"* (Bates and Jackson, 1980) This basic definition of the fundamental unit that stratigraphers use to construct depositional models can be transposed from the world of well log, outcrop, and faunal-assemblage analyses to the world of seismic interpretation by defining a ***seismic sequence*** to be *"a relatively conformable succession of genetically related seismic reflections bounded at the top and base by conformities or their correlative conformities"* (Mitchum, 1977; Mitchum and others, 1977b). Stratigraphic interpretation of seismic data is based on interpreting suites of stratal surfaces across seismic image space and then using these stratal surfaces to construct spatial assemblages of sequences that describe the depositional processes that created stratigraphic intervals of interest (Brown and Fisher, 1977). The concept of a seismic sequence is fundamental to the science of seismic stratigraphy, and interpretation of seismic sequences has been a principal focus of our research as we analyzed various multicomponent seismic data sets.

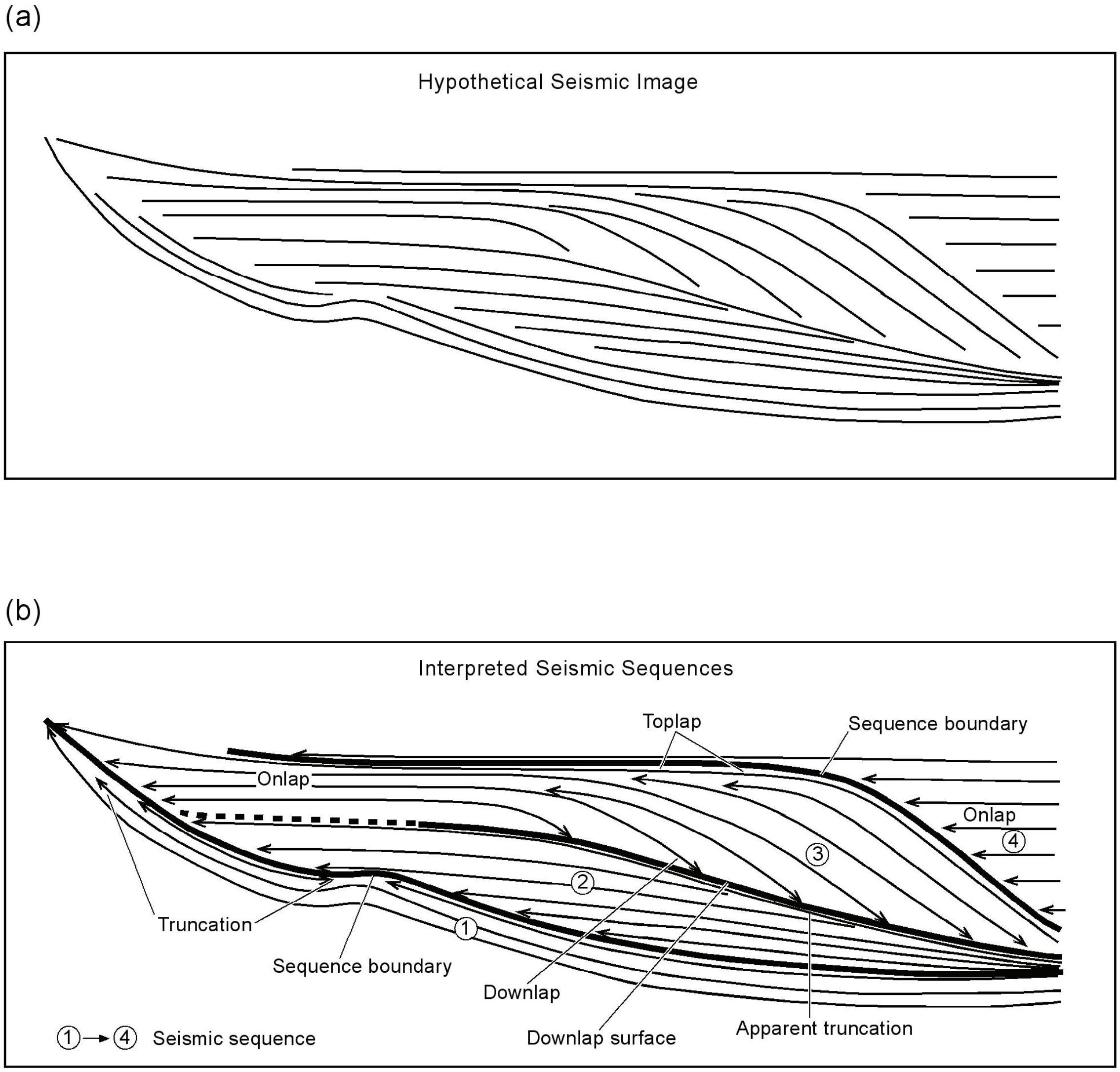

QAd4886cx

Figure 6. (a) A hypothetical seismic image, either P-wave or S-wave. Each line represents a seismic reflection event. (b) Seismic stratigraphy interpretation of the image. Seismic sequence boundaries follow the trends of reflector terminations, which are marked by arrowheads.

Two properties of seismic reflection events are critical for recognizing seismic sequences: (1) reflector angularity and (2) reflection terminations. Each of these reflection properties allows inferences to be made about the geologic conditions that existed when the imaged sediment was deposited. Seismic sequence interpretation concepts are illustrated in Figure 6. The top panel shows a commonly encountered configuration of seismic reflections. The bottom panel shows how reflector angularity and reflection terminations infer unconformity surfaces and allow seismic sequences to be constructed. This interpretation procedure is independent of the type of seismic data that image the geology; the data in Figure 6a can be P-wave seismic data or S-wave data.

The importance of unconformities as the defining boundaries of seismic sequences cannot be overstated (Mitchum and Vail, 1977). By definition, an ***unconformity*** is *a break in sediment deposition*. These sediment breaks can be due to either a loss of section (erosion) or to a loss of geologic time (nondeposition). In either case, major implications are that

- sediment supply was eliminated,
- the paleoenvironment changed,
- active tectonism may have occurred, and
- a time-rock boundary was created.

Specific terminology is used to define the seismic reflectivity patterns that are associated with seismic sequences. A partial list of terms often used to describe reflection character in a seismic sequence interpretation includes

- toplap
- baselap
- onlap
- offlap.
- downlap
- truncation
- internal convergence

Some of these seismic reflection properties are illustrated in Figure 6. This seismic sequence terminology applies to seismic images made with any mode of an elastic wavefield and can be used in elastic wavefield stratigraphy as well as in conventional P-wave seismic stratigraphy.

Time-Rock Stratigraphy

The first step in a geological evaluation of any area, large or small, is to establish which sedimentary units are equivalent in geologic time. Because bedding planes (stratal surfaces) are parallel to geologic time, the critical step in identifying time-equivalent units is to define bedding planes and stratal surfaces across areas of interest. Therein lies the fundamental importance of the assumption of seismic stratigraphy that seismic reflections image chronostratigraphic surfaces (stratal surfaces).

Rock units parallel geologic time only in situations where there is slow sedimentation or rapid transition of depositional environments across an area. Examples of rock units that locally parallel geologic time are thin limestones, thin sandstones, coal beds, and thin bentonite beds. If seismic data can image these targets, the seismic reflection associated with each particular rock unit is both a lithostratigraphic surface and a *local* chronostratigraphic surface. In all seismic interpretations, it is advisable, if at all possible, to correlate seismic reflections to faunal assemblages to confirm the assumption of constant geologic time along the seismic reflection.

Key Concept: Seismic Facies

An important foundation of seismic stratigraphy is the concept of a seismic facies. The original Latin meaning of ***facies*** is *“appearance”* or *“aspect.”* In seismic stratigraphy, a ***seismic facies*** is *“a group of seismic reflections whose parameters (configuration, amplitude, continuity, frequency, and interval velocity) differ from adjacent groups”* (Mitchum and others, 1977a). This definition allows great latitude in selecting criteria to define a seismic facies. In early seismic stratigraphy practice, criteria used to define a seismic facies unit involved definitions of

- the type of reflection terminations occurring at the top and bottom boundaries of the unit,
- the geometrical configuration of the reflection pattern within the unit,
- distinctive characteristics of the internal and bounding reflection events, and
- the geometrical shape (or external form) of the unit.

Table 1. Possible geologic interpretations of seismic facies patterns.

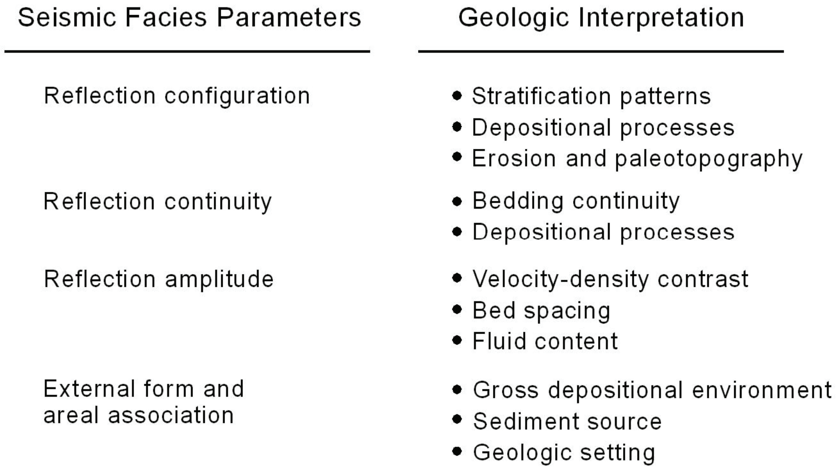

Seismic Facies Parameters	Geologic Interpretation
Reflection configuration	• Stratification patterns • Depositional processes • Erosion and paleotopography
Reflection continuity	• Bedding continuity • Depositional processes
Reflection amplitude	• Velocity-density contrast • Bed spacing • Fluid content
External form and areal association	• Gross depositional environment • Sediment source • Geologic setting

Mitchum and others, 1977a

QAd4884cx

Modern seismic facies interpretation should continue to use these criteria for defining seismic facies, even though numerical, computer-based, facies-recognition algorithms have replaced much of the human interaction with seismic data. Common geologic interpretations that can usually be associated with frequently observed seismic facies parameters are summarized in Table 1.

In the initial practice of seismic stratigraphy, seismic facies interpretation and mapping were done by hand. One of the popular seismic facies classification schemes developed in the 1970's and early 1980's was called ***XYZ Mapping*** (or ABC Mapping by some). That laborious procedure is still valuable for understanding how seismic facies analysis is done and is illustrated in Figure 7.

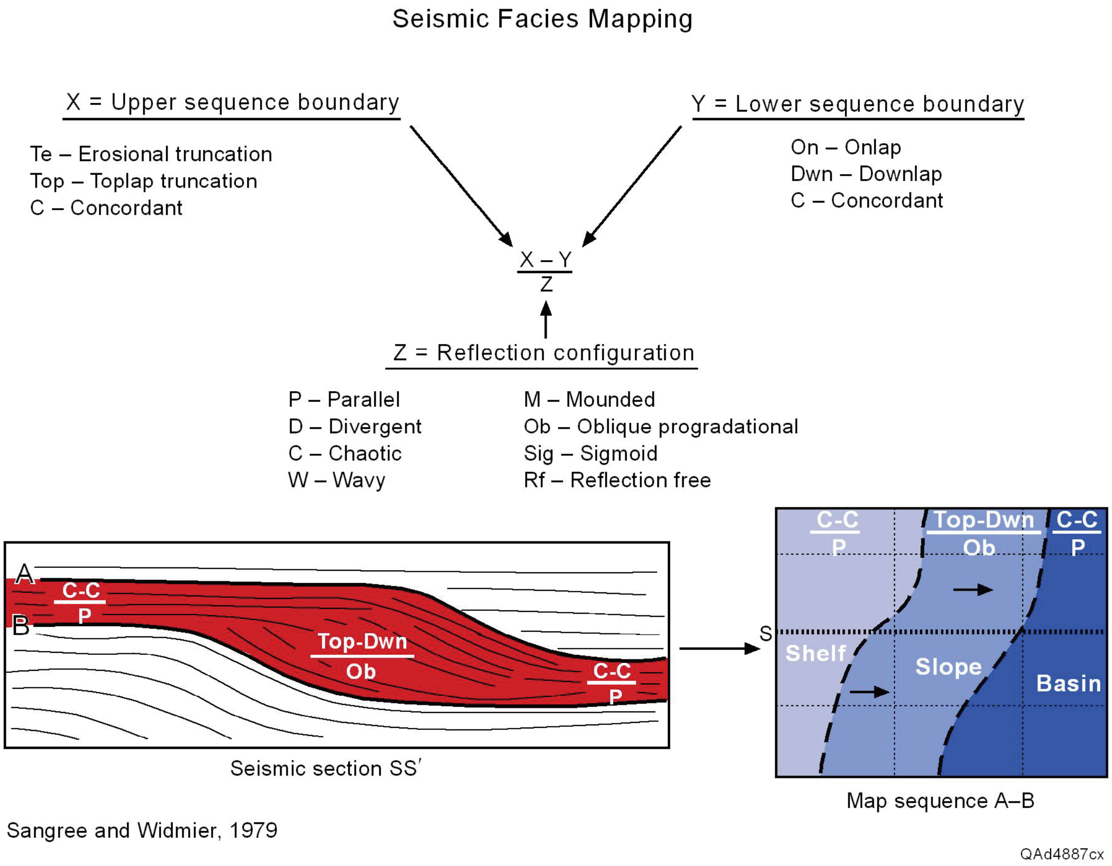

Figure 7. Concept of XYZ seismic facies mapping. In this mapping process, X, Y, and Z are qualitative descriptive terms defined by visual inspection of the seismic data. The lists of X, Y, Z options shown here are arbitrary; each seismic stratigrapher uses different criteria to define distinctive facies. These qualitative and arbitrary choices of seismic facies parameters have now been replaced by numerical algorithms that recognize subtle changes in seismic waveform character across a defined seismic data window. The seismic facies defined on the seismic section (lower left) contribute to the construction of the map of depositional environments (lower right).

The term XYZ Mapping was used to describe this interpretation procedure because the map notations used by numerous seismic stratigraphers were of the form (X - Y)/Z, where X described the type of reflection termination along the top boundary of a seismic sequence, Y defined the type of reflection termination along the lower boundary of the sequence, and Z indicated the geometrical configuration and/or character of the reflections internal to the sequence. The descriptive terms for X, Y, and Z listed in Figure 7 are popular characteristics that have been used by many stratigraphers. This list is suggestive, not exhaustive. Additional terms used to describe the internal form of a seismic facies are listed in Table 2.

Table 2. Descriptive terms for the internal forms of seismic facies.

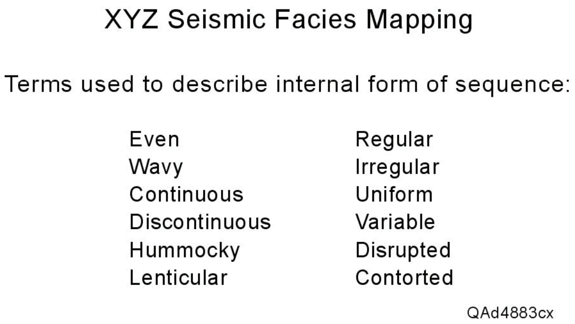

XYZ Seismic Facies Mapping

Terms used to describe internal form of sequence:

Even
Wavy
Continuous
Discontinuous
Hummocky
Lenticular

Regular
Irregular
Uniform
Variable
Disrupted
Contorted

QAd4883cx

Recently, specialized interpretation software has been commercialized that allows seismic facies to be identified numerically, segregated into facies classes, and then mapped to show suggested patterns of sedimentary units. Numerous examples of these modern, numerically defined, seismic facies will be shown throughout this report. These mapped attributes need to be correlated with subsurface geologic and engineering control in order for specific geologic properties to be associated with each class of seismic facies. A large number of published case histories have demonstrated that seismic facies maps are invaluable in constructing spatial distributions of reservoir facies, sealing facies, and depositional system architecture (Sangree and Widmier, 1977, 1979; Roksandic, 1978; Davis, 1984).

All of the seismic facies terminology, principles, and mapping techniques discussed in this section apply to all seismic modes, not just to the P-P mode used in conventional seismic stratigraphy. The same seismic facies technology and language used in conventional P-wave stratigraphy also apply in elastic wavefield stratigraphy, where S modes are interpreted in addition to the P-P mode.

Stratal Slicing

Interpreters who analyze vertical sections of 3-D seismic volumes line by line can find field-scale geologic and depositional features (units 50 m or more thick), but some reservoir-scale features (units 3 to 10 m thick) cannot be resolved and interpreted when interpretation is limited to only vertical sections because of data-bandwidth limitations. For example in the vertical view in Figure 8a, the seismic facies immediately around the horizontal dashed line were interpreted to be fluvial deposits on the basis of the presence of discontinuous, patchy events and frequent lateral changes in P-P reflection amplitudes. Wells drilled through the interval supported this interpretation. However, correlating individual channel-fill sand bodies and marginal facies (such as levees and crevasse splays) on adjacent vertical views is difficult because these facies elements are thin (3 to10 m), and the seismic resolution barely resolves the tops and bases of even the thickest of the units. For example, in this particular section view it is impossible to decide what depositional elements are represented by the circled features in Figure 8a.

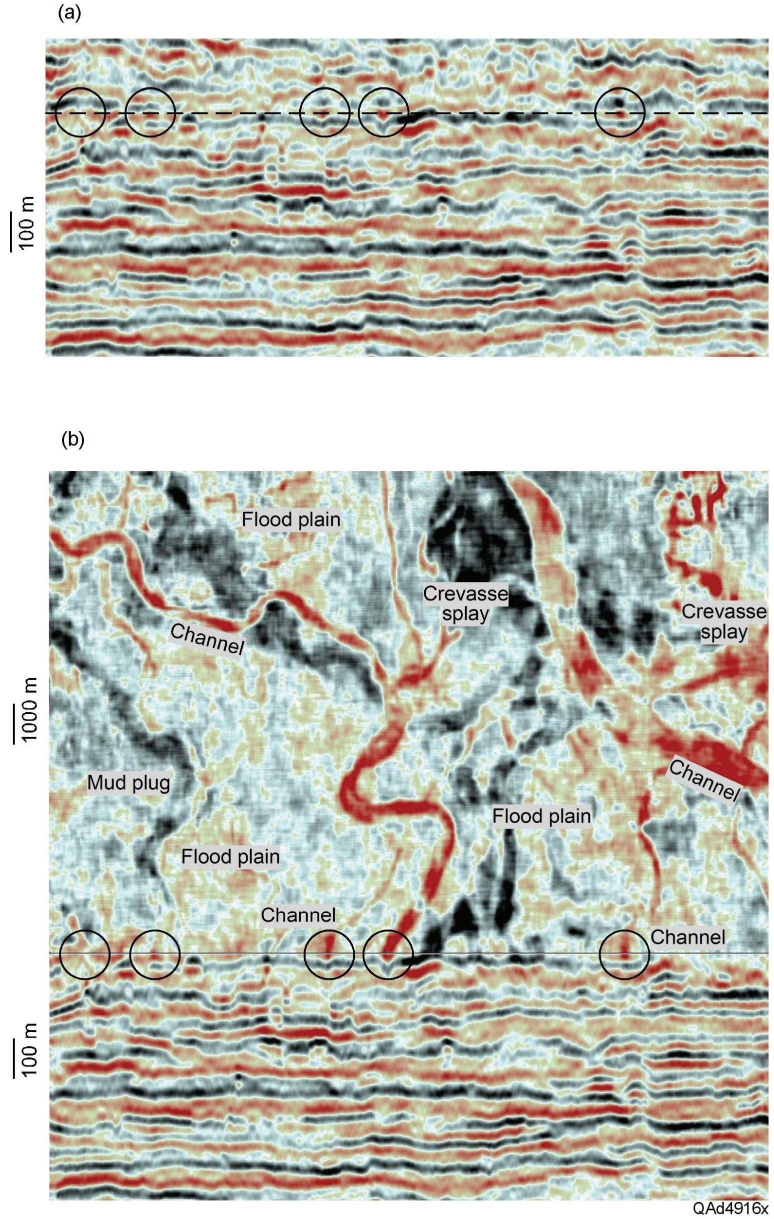

Figure 8. (a) Vertical section view of a fluvial environment imaged with P-P seismic data (interval immediately around the horizontal dashed line). (b) Stratal slice through the dashed-line horizon showing that small depositional features are better seen in horizontal view than in section view. Taken from Zeng (2006).

To map depositional systems with high resolution in a seismic stratigraphy study, one strategy is to change the emphasis of seismic interpretation from vertical sections to horizontal sections. For perfectly migrated 3-D seismic data, horizontal resolution is the same as vertical resolution. Outcrop and subsurface studies show that depositional bodies have horizontal dimensions greater than their vertical dimensions. As a result, small depositional bodies can often be "***resolved***" in plan view when they can only be "***detected***" in vertical view.

To implement a horizontal-view seismic stratigraphy interpretation, we must pick geologic-time surfaces (or stratal surfaces) from 3-D seismic volumes so that seismic attribute (seismic facies) maps across these fixed-geologic-time surfaces can be analyzed in terms of depositional systems. ***Time slices*** and ***horizon slices*** are traditional horizontal-section views used by seismic interpreters (Fig. 9a, b). Time-slice displays of seismic facies are extracted from a data volume by displaying a selected seismic facies behavior across a constant-image-time surface. A horizon slice of this same seismic facies is constructed by extracting a seismic attribute across a surface that is parallel to a picked, time-varying, seismic horizon. For either horizontal view to be an accurate representation of a stratal surface, one must assume the formation being sliced is flat-lying when time slicing is used (Fig. 9a) or that the formation has a sheetlike geometry (Fig. 9b) when horizon slicing is used.

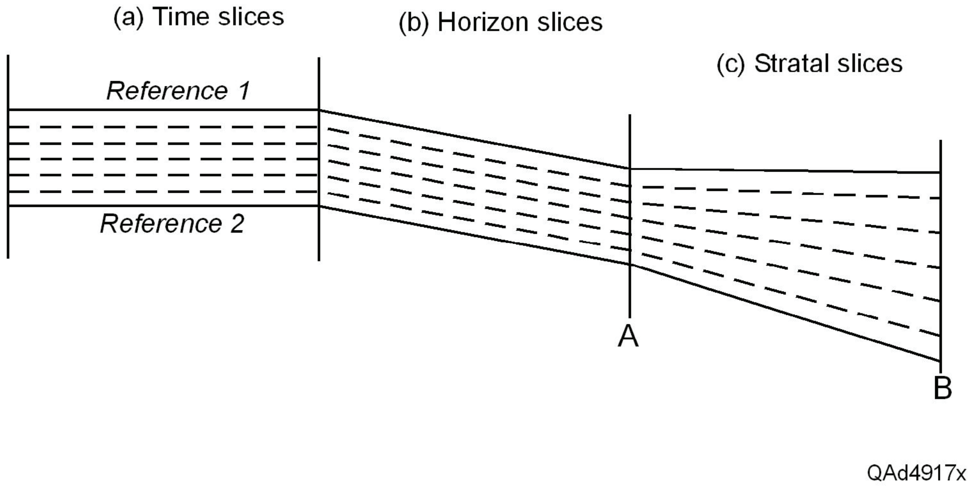

Figure 9. Distinctions among (a) time slices, (b) horizon slices, and (c) stratal slices. A time slice follows a constant image-time coordinate. A horizon slice is positioned at a constant image-time offset from a reference seismic reflection event. A stratal slice is positioned at a constant geologic-time offset from a reference seismic reflection event. Taken from Zeng (2006).

However, many depositional sequences are characterized by thickness changes (Fig. 9c), which cause horizon-slice and time-slice surfaces to sample seismic facies that are associated with strata of different geologic ages. In seismic stratigraphy studies, a different surface extraction method must be used to ensure that an extracted surface follows a fixed-geologic-time surface. One such method is ***stratal slicing*** (Fig. 9c), or proportional slicing, a technique developed by Zeng (2001, 2006), our research colleague at the Bureau. Stratal slicing divides the variable-thickness vertical interval between two seismic reference reflection events into a fixed number of uniformly spaced subintervals. If the number of subintervals is 10 and the time thickness between the reference surfaces at points A and B (Fig. 9c) is 27 ms and 58 ms, respectively, then the thickness of each subinterval at coordinate A is 2.7 ms, and at point B, each subinterval is 5.8 ms thick. The interface between each pair of subintervals (the dashed lines in Fig. 9c) approximates a stratal surface. For stratal slicing to work optimally, Reference Reflections 1 and 2 defined in Figure 9 should be sequence boundaries so that no major angular unconformities (truncations) or other discordant reflections occur between the reference events.

As a demonstration of stratal-slice interpretation, a stratal slice passing through the dashed line in Figure 8 shows high-quality images of fluvial channels, crevasse splays, a floodplain, and a mud plug (Fig. 8b). Although most of these depositional elements are less than 10 m thick and are thus below vertical seismic resolution for these particular P-P data, the units are well resolved in the horizontal dimension in a well-constructed stratal surface.

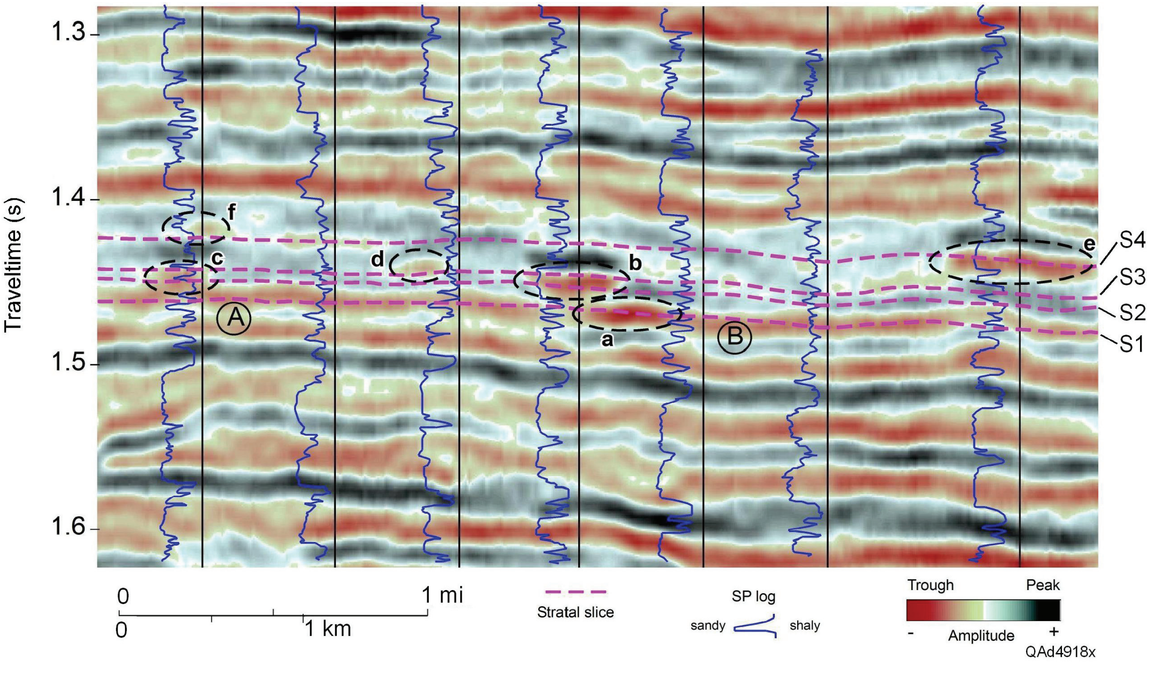

Figure 10. A Pliocene interval from the Gulf of Mexico extracted from a P-P data volume. Dashed horizons S1 through S4 are stratal slices. Time intervals between adjacent stratal slices vary in thickness across seismic image space (Fig. 9c), as seen in this case by comparing the interval between S1 and S2 at points A and B. Circled features **a** through **f** are sandstone units. Each well log is an SP curve. Taken from Zeng (2001).

Stratal slices provide a stratigraphic resolution that cannot be achieved using vertical sections alone. The data in Figure 10 show a Gulf Coast Pliocene sequence in a P-P volume that has a dominant frequency of 30 Hz and a vertical resolution of about 10 m. Four stratal slices were taken inside a time-varying interval that had a thickness of approximately 40 ms (~36 m) and are shown by stratal surfaces S1 through S4. Interpretation of wireline well logs (SP) across the interval shows that the sandstones are fluvial in nature. Some of the sandstone units (**a, b**, and **e**) are thick (20 to 25 m) and create amplitude anomalies. Other units are thin (10 m or less) and subtle (**c**, **d**, and **f**). In map view, the four stratal slices image four episodes of fluvial deposition (Fig. 11). The fluvial systems on stratal slices S1, S2, and S4 are fully resolved without interference from units immediately above or below each stratal surface. Stratal slice S3 shows a narrow (35 to 70 m [1 to 2 traces] wide), well-developed meandering feature interpreted to be a small coastal plain channel (arrows in Fig. 11). Wireline logs indicate that this channel-fill sandstone is about 4 m thick. Image S3 is only 6 ms (7 m) above slice S2 (Fig. 10) and is contaminated by some interference from the S2 fluvial system. Even so, identification of this small, meandering channel across stratal surface S3 is unambiguous. The image resolution achieved in this case is much less than vertical resolution and probably represents the limit of resolution expected from stratal-slice analysis for this data set.

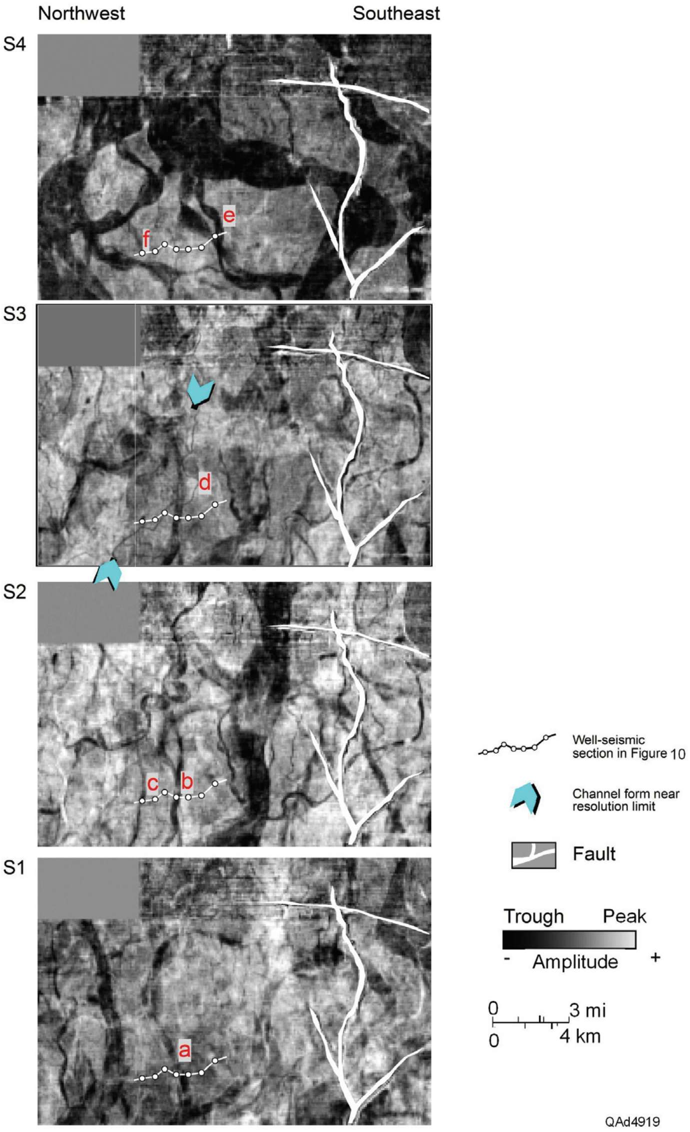

Figure 11. Large-area map views of geology across stratal surfaces S1 through S4 defined in Figure 10. The position of the vertical section in Figure 10 is identified on each map view. Channels **a** through **f** labeled on these surfaces correspond to features **a** through **f** circled in Figure 10. Arrows on surface **S3** mark an extremely narrow meandering channel. Taken from Zeng (2001).

Only P-P seismic data are used in this section to illustrate the value of stratal-slice interpretation. However, stratal-slicing methodology can be applied to seismic images made from any elastic wave mode (P-P or SH-SH, SV-SV, P-SV, and SV-P) and should be the interpretation method of choice in any seismic stratigraphy study. Having said this, we still elected not to utilize stratal-slicing methods to demonstrate the principles of elastic wavefield stratigraphy in the *Data Examples* section of this report. Instead, we use the conventional approaches of time slices, horizon slices, and simple visual inspection of vertical slices to build the evidence that different modes of an elastic wavefield provide an interpreter different, but equally valid, seismic sequences and seismic facies.

We made this choice not to use stratal slicing to emphasize that seismic interpreters can continue to use their traditional tools and still receive great benefit by implementing elastic wavefield stratigraphy rather than conventional P-P seismic stratigraphy. If they combine elastic wavefield stratigraphy with stratal-slicing technology, even more benefits accrue.

Depth Registration of P and S Data

Two critical assumptions are involved in elastic wavefield stratigraphy: (1) across some stratigraphic intervals, one mode of an elastic wavefield may exhibit different seismic sequences and facies than do its companion modes, and (2) S-wave seismic sequences and facies are just as important in geologic interpretation as are P-wave seismic sequences and facies.

Once these two assumptions are accepted, a serious interpretational challenge is then encountered: depth registration of P and S images. An interpreter must be confident that a targeted data window in P-wave image space is depth equivalent to a data window selected from S-wave image space before the seismic sequences and seismic facies created in these respective data windows can be combined into an elastic wavefield stratigraphy analysis. Until depth-equivalent P and S data windows are defined, no meaningful geological interpretation of P and S sequences or facies can be done. Techniques that seismic stratigraphers use to define depth-equivalent Earth coordinates in P-wave and S-wave image spaces include

1. multicomponent vertical seismic profile (VSP) data,
2. map and section views of P and S images of stratigraphy,
3. numerical cross-equalization of P and S images,
4. P-wave and S-wave synthetic seismograms, and
5. map and section views of P and S images of structure.

Options 1, 2, and 3 are discussed in the sections that immediately follow; options 4 and 5 will be illustrated in the *Data Examples* section of this report.

Option 1: Multicomponent VSP Data

Multicomponent VSP data allow rigorous and accurate depth registration of P and S images if the VSP data are acquired with receiver stations distributed over a large vertical interval. The depth origin of a seismic reflection can be determined precisely with VSP data only if closely spaced VSP receivers span the interface that produces that reflection. As the length of a vertical array of VSP receivers increases, more reflecting interfaces are spanned, and an increased number of depth-equivalent P and S reflections are identified.

Examples of 9-component (9C) VSP data used to define depth origins of P-P, SH-SH, and SV-SV reflections across an interval of Morrow channel deposition are shown in Figure 12. These data were created in an early elastic wavefield stratigraphy investigation done by the research team (Hardage and others, 2003). One advantage of VSP data acquisition is that the data are acquired as a function of receiver depth and reflection arrival time, allowing a VSP image to be constructed as a function of either (1) seismic image time or (2) depth. The data in Figure 12 are examples of depth-based VSP imaging. The three VSP wells are in three different states: Texas, Kansas, and Colorado. The images show that at each well, each elastic wave mode images different Morrow-related stratal surfaces and produces a reflection sequence and a seismic facies across the targeted Morrow interval that are different from the sequences and facies produced by its companion wave modes. The different stratal surfaces imaged by each wave mode form the basic building blocks of elastic wavefield stratigraphy. These VSP data are powerful examples of the principle that different elastic wave modes image different stratal surfaces across some stratigraphic intervals.

Option 2: Map and Section Views of Stratigraphy

An example of the use of horizontal time slices through P and S coherency volumes to define depth-equivalent stratigraphy is illustrated as panels a and b of Figure 13. The P-P image shows a system of several intertwined channels. The P-SV image shows only one channel, but that channel tracks one of the P-P channels, leading us to the conclusion that the P-P and P-SV time slices are imaging the same stratigraphy. The channel architecture shown on these two images persists for a narrow vertical range of only two to three data samples in each image space.

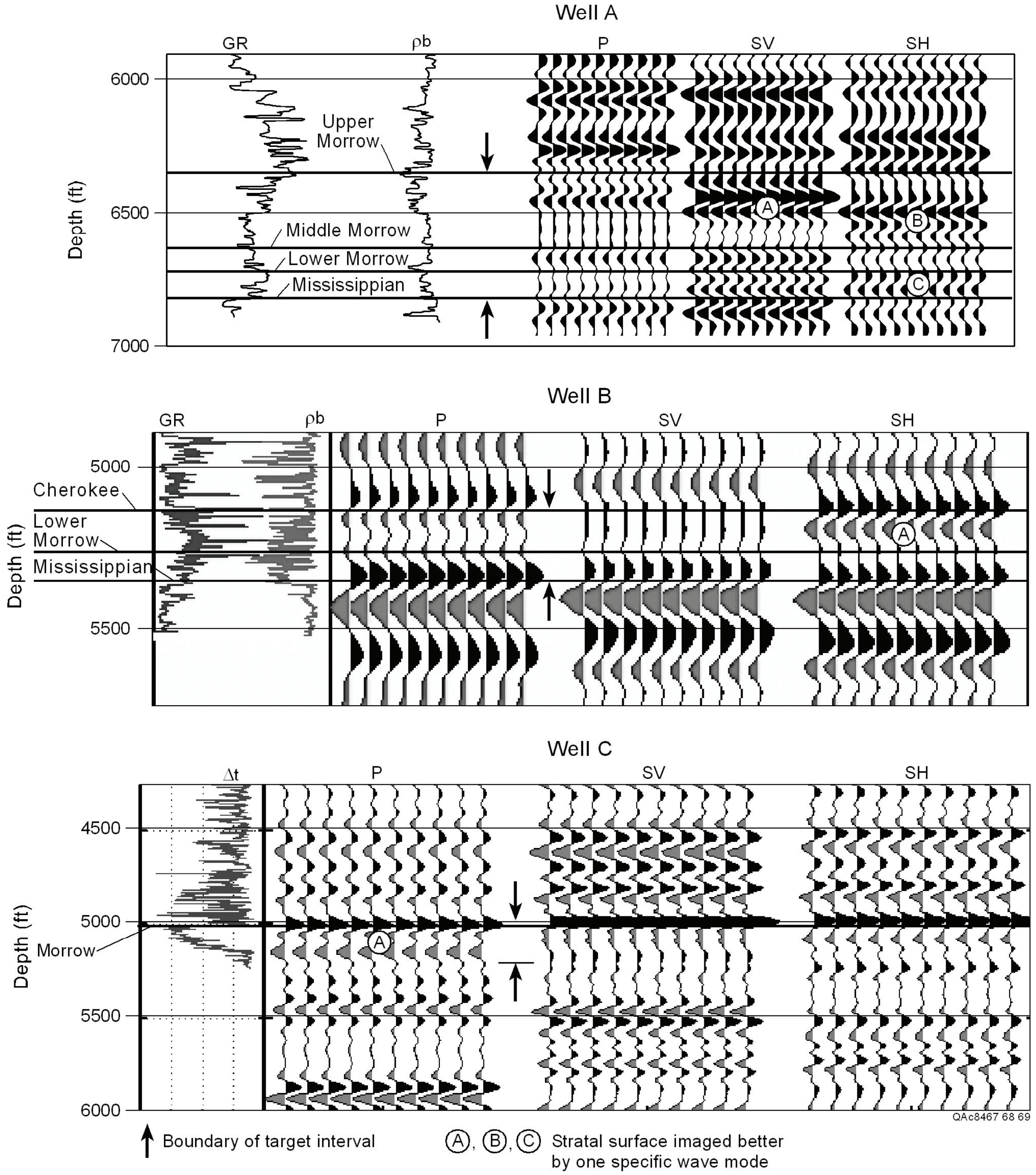

Figure 12. Depth-based P-P, SV-SV, and SH-SH images constructed from 9-component VSP data acquired in three wells penetrating Morrow-channel environments. One wave mode often reveals a key stratal surface within a target interval that its companion wave modes do not. Examples of such surfaces are labeled **A**, **B**, and **C** for Well A (top) and **A** for Well B (center) and Well C (bottom). Taken from Hardage and others (2003).

Two important conclusions can be made: (1) P-P image time 796 ms in Figure 13a is depth equivalent to P-SV image time 1,964 ms in Figure 13b and (2) P-P and P-SV modes often show significantly different sequence and facies pictures of the same geology. This latter conclusion is a fundamental premise of elastic wavefield stratigraphy and is demonstrated in this example by the fact that the P-P mode and the P-SV mode depict a different channel system.

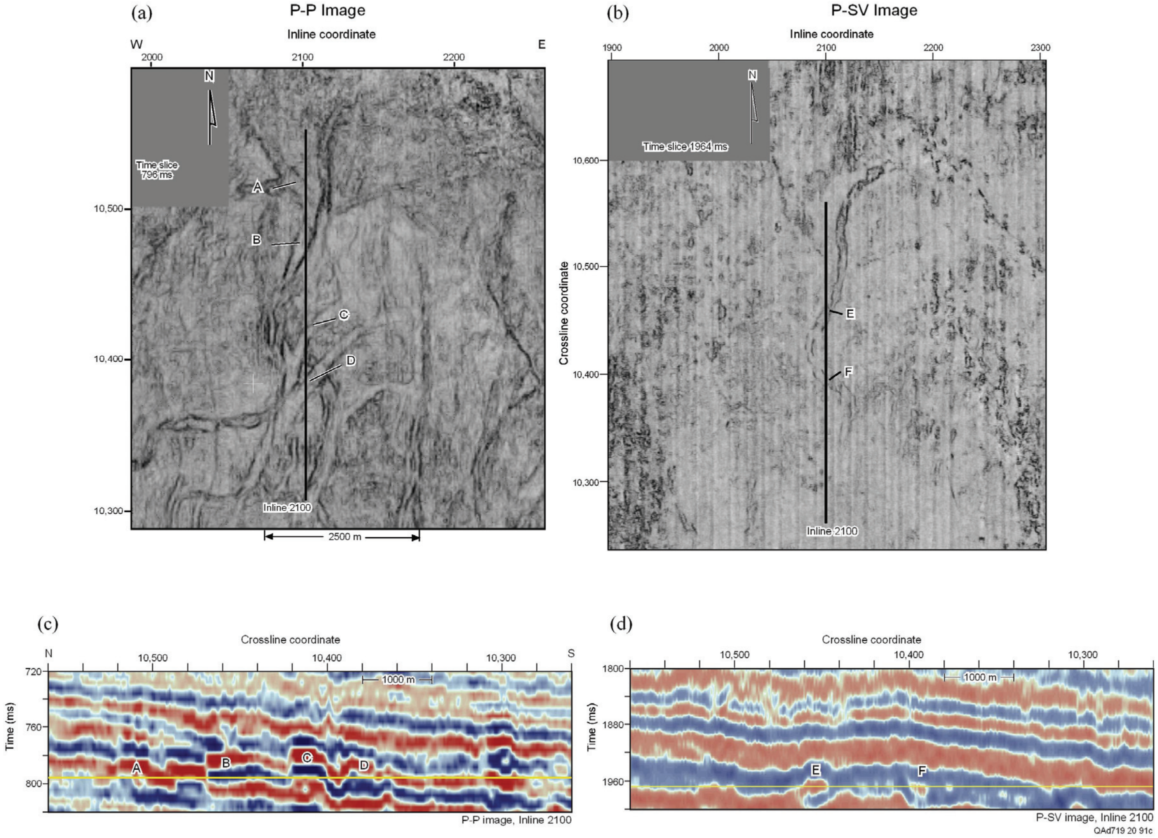

Figure 13. Map views of thin stratigraphy (a) and (b) used to depth register P-P and P-SV images. In map view, the equivalence of thin P-P and P-SV channel features results in P-SV time 1,964 ms (b) being defined to be depth equivalent to P-P time 796 ms (a). It is more difficult to determine depth-equivalent image coordinates using 2-D section views (c) and (d) of this same stratigraphy. The horizontal yellow lines across the section views define positions of the time slices. The vertical sections are positioned along inline coordinate 2100. Channel features **A** through **F** on the map views are the same features labeled **A** through **F** on the vertical sections (DeAngelo and others, 2003).

Shown in panels c and d are vertical slices through these P-P and P-SV volumes along profile 2100, which is labeled on the horizontal slices. The horizontal yellow line across each vertical slice shows where the horizontal slice (either a or b) was taken across each data volume. Using only vertical displays of P-P and P-SV data, an interpreter would have to have great courage to claim that the two yellow horizons are depth equivalent. In contrast, few interpreters object to the statement that the two map views in panels a and b are depth equivalent. These examples lead to the conclusion that map views of stratigraphy, particularly views of thin stratigraphy, can be a rather precise option for depth registering two elastic-mode images, whereas depth registration of P and S data is usually more difficult using vertical section views.

Inspection of the images in panels c and d shows that the P-SV data have a lower frequency waveform at the yellow time-slice level than do the P-P data. This apparent distinction between the P-P wavelet and the P-SV wavelet, when coupled with the modeling results of Figures 3 through 5, suggests that some of the difference between the P-P and P-SV facies depicted on the time slices is caused by inconsistent imaging wavelets.

Option 3: Numerical Registration of P and S Images

One objective of our research has been to develop a numerical method that adjusts S-wave images to be depth equivalent to P-wave images so that depth-equivalent P and S sequences and facies can be analyzed across narrow seismic data windows. We addressed this objective by first developing a technique that worked for a single pair of synthetic P-P and P-SV seismic traces. After appropriate testing, we expanded that algorithm so that we could analyze 2D P-P and P-SV profiles and then advanced the methodology so that it worked with 3D multicomponent seismic data. With each application of the algorithm to real data, we added better analysis methods and convergence steps and are now rather comfortable that we have a unique and valuable tool for assisting elastic wavefield stratigraphy research.

The mathematics of the depth-registration algorithm that we have developed will not be described in this report. The methodology has been published and can be reviewed by interested readers (Fomel and others, 2003). We document here only one example that illustrates the accuracy and quality of the depth registration that was achieved with the algorithm in our interpretation of one 3C3D seismic survey. This example is illustrated as Figure 14.

The method requires that an interpreter first define a small number of depth-equivalent geologic features (at least two or three) in both P-P and P-SV image space. Any of the depth-registration options listed at the beginning of this discussion, or plain guesswork, can be used to identify these features. Once these control points are defined, they are used to do a first-order time warping to convert P-SV image time to P-P image time. This initial depth registration is usually satisfactory for general comparisons of P-P and P-SV seismic sequences and facies, but it is rarely sufficient for detailed P-P and P-SV stratigraphic analysis of thin targets.

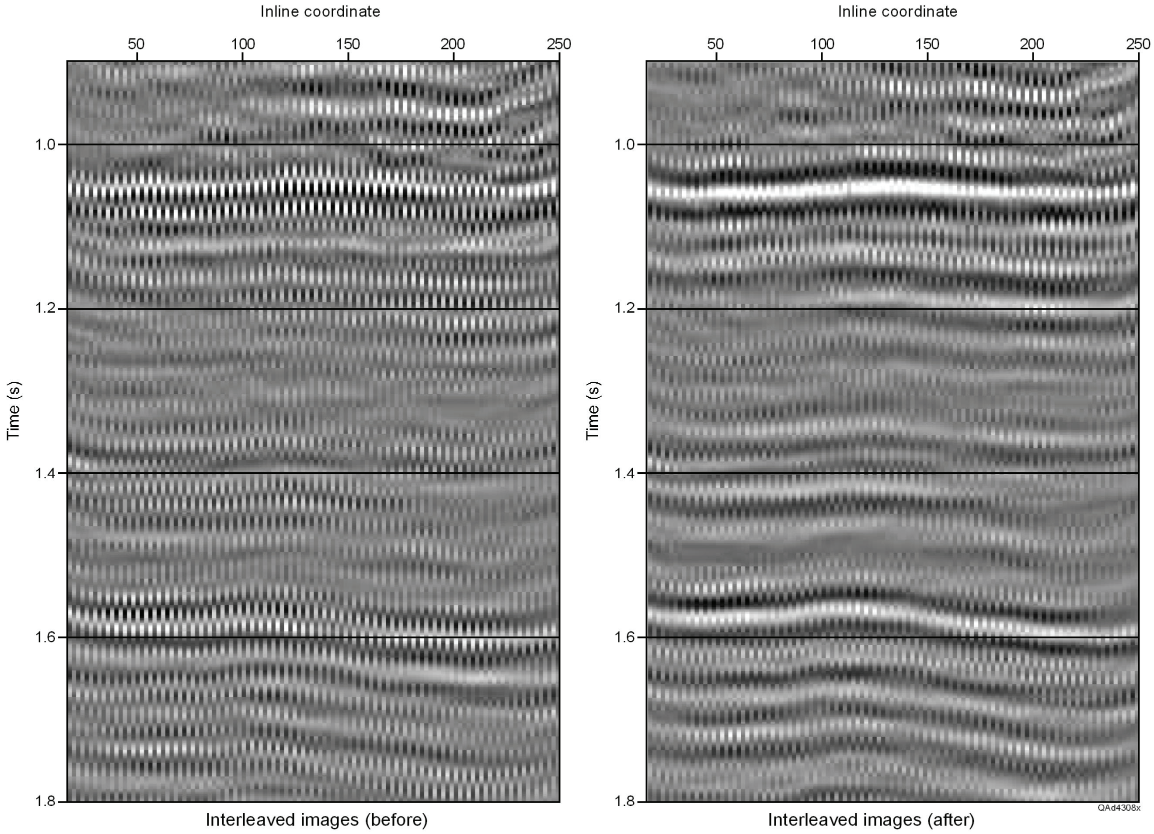

Figure 14. Examples of P-P and P-SV images before and after applying a least-squares-minimization technique to perform a numerical depth registration of elastic-mode images. The P-P and P-SV images are shown as alternate, interleaved traces in each display, which is a display format in which it is easy to visually judge the quality of the image registration.

Data shown in the left panel of Figure 14 are interleaved traces of P-P and P-SV data along the same vertical profile through a West Texas 3C3D seismic data volume after the P-SV data were time warped to P-P image time coordinates by a first-order adjustment function. These adjusted data represent the type of P-P to P-SV depth registration that is commonly practiced across the seismic data-processing industry. In this display, the P-P and P-SV data traces are interleaved to allow a quick, visual judgment about the magnitude of the mismatch between the two images when a typical first-order time-warping correction is done by a data-processing shop. The data in the right panel are the same P-P and P-SV profiles, after the data volumes have been further depth registered according to our numerical procedure that uses a loosely constrained, least-squares-optimization algorithm to adjust the images to an optimal match. This convergence step creates better consistency between the interleaved traces, and we can now determine seismic facies attributes in data windows that are quite thin and be confident that the P-P and P-SV data within these windows span the same depth interval. These depth-registered data will be analyzed again in the discussion of Figures 18 and 19.

P and S Polarization Vectors and Reflectivity

Two arguments help explain why P-wave sequences and facies often differ from S-wave sequences and facies. First, assume an elastic wavefield is traveling vertically through a horizontally layered medium. The P-wave particle-displacement vector associated with that wavefield then senses the fabric of the medium in a direction normal to the layering; whereas, the companion S-wave particle-displacement vector senses the fabric in a direction parallel to layering. The elastic constants of the medium differ in these two displacement directions.

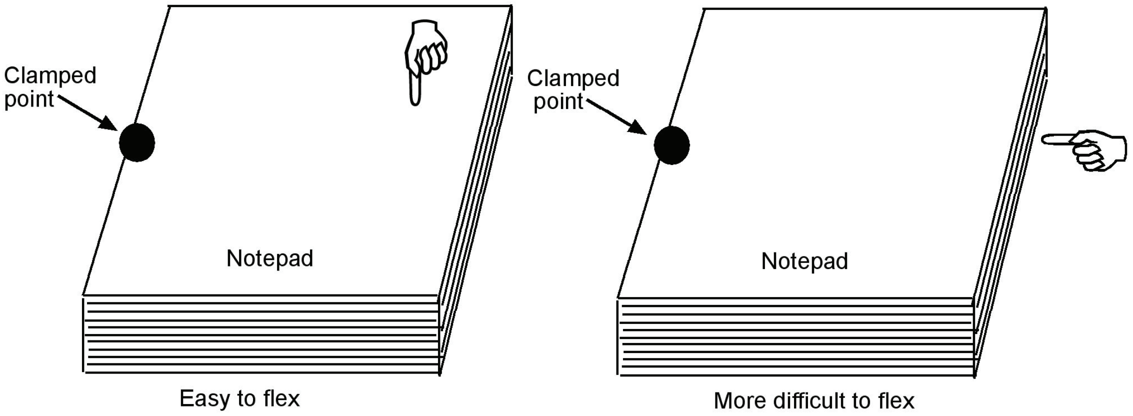

QAd4341

Figure 15. A simple experiment illustrating that a layered medium exhibits a different fabric (or strength) when its elasticity is tested in directions normal and parallel to its layering.

For example, forces of different magnitudes have to be applied to flex a deck of playing cards or the sheets of a notepad when those forces are directed normal to layering and parallel to layering (Fig. 15). In this simple demonstration, the medium is the same at the common point where the forces are applied, but the strength (or fabric) of the material is not the same in the two force directions. Thus, P-wave seismic sequences and facies sometimes differ from S-wave sequences and facies across a stratigraphic interval because a vertical P-wave particle-displacement vector and a horizontal S-wave particle-displacement vector sense and react to different elastic properties of the layered-rock system within that interval.

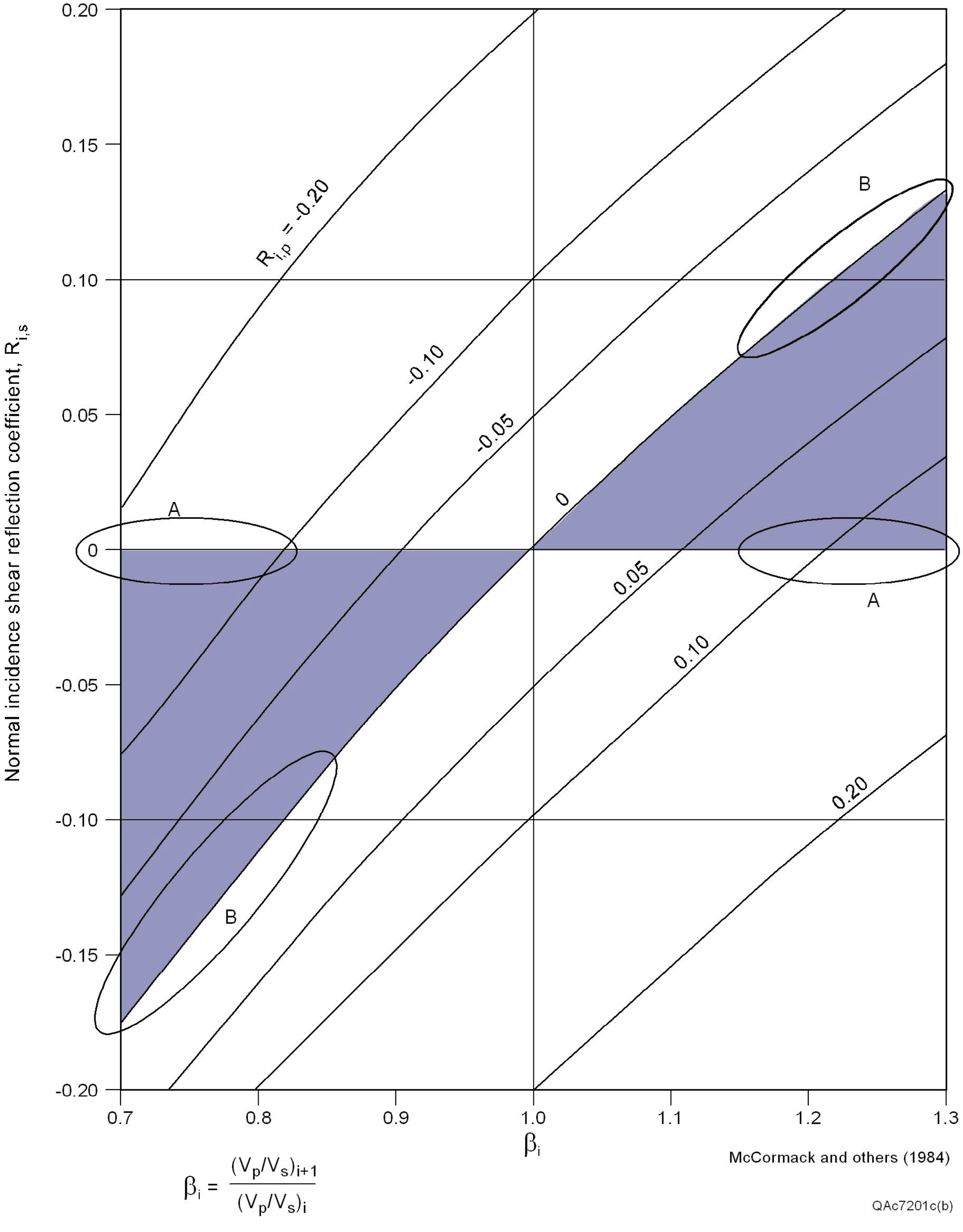

Figure 16. Relationships between normal-incidence S-wave reflectivity $R_{i,S}$ and P-wave reflectivity $R_{i,P}$ for differing contrasts of the V_P/V_S velocity ratio across an interface. For normal incidence, there is no distinction between SH-SH and SV-SV reflectivity. Modified from McCormack and others, 1984.

Second, the reflectivity of each mode of an elastic wavefield at an interface differs from the reflectivities of its companion modes. One example of this principle is illustrated in Figure 16. Vertical axis $R_{i,S}$ in this figure is S-S reflectivity at an interface (the term S-S is used because SH-SH and SV-SV have the same reflectivity for normal incidence), horizontal axis β is the ratio of the velocity ratio V_P/V_S across that interface, and quantity $R_{i,P}$ labeled on each curve is P-P reflectivity at the interface. These curves show that there are interfaces that

1. are invisible to P waves (the curve labeled $R_{i,P} = 0$) but are not invisible to S waves unless β = 1.0,
2. are invisible to S waves (the horizontal line $R_{i,S} = 0$) but are not invisible to P waves unless β = 1.0,
3. cause P-P and S-S reflections to be in phase (shaded parameter regions) and others that cause P-P and S-S reflections to be opposite polarity (unshaded parameter regions), and
4. are robust P-P reflectors but weak S-S reflectors (elliptical domains A) and others that are robust S-S reflectors but weak P-P reflectors (elliptical domains B).

Any combination of P-P and S-S sequences and facies can thus be encountered in elastic wavefield stratigraphy, depending on how the V_P/V_S velocity ratio varies across interfaces illuminated by a multicomponent seismic wavefield.

Data Examples

In our research, we examined P-P seismic sequences and facies across selected target intervals in numerous multicomponent seismic data sets and then compared these sequences and facies with seismic facies and seismic sequences extracted from other modes of the seismic elastic wavefield that imaged the same interval. Our investigation documented situations where one elastic wave mode defined depositional architecture and reservoir lithofacies better than did its companion wave modes. In each instance, we tried to determine the petrophysical and stratigraphic conditions that caused these imaging differences. We did not limit our study geographically; we utilized multicomponent seismic data acquired in several basins and in both marine and onshore environments to illustrate basic principles of elastic wavefield stratigraphy.

Low-Porosity Carbonate System

P and S Sequences and Facies

The West Texas project described here involves 3C3D seismic data. There are thus only two elastic modes to analyze—the P-P mode and the P-SV mode. These data were acquired in Andrews County near Midland, Texas (Fig. 17).

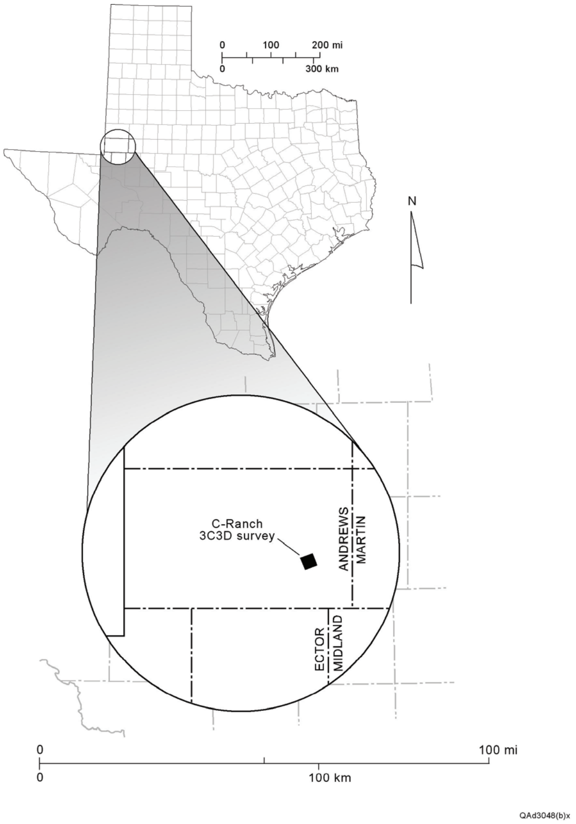

Figure 17. Location of a West Texas 3C3D seismic survey used in elastic wavefield stratigraphy research.

The principal target of interest was the Strawn Formation at a drilling depth of approximately 11,500 ft (~3,500 m). P-P and P-SV images constructed from the 3C3D data were good quality at this target depth. Maps of the top of the Strawn Formation interpreted from the P-P and P-SV data volumes are shown in Figure 18. There are only minor differences in the P-P and P-SV depictions of the structural ridge that plunges northeast across the image space. The equivalence between the structural pictures shown by these two maps indicates that the P-P and P-SV modes have been properly processed and, more importantly, that the P-P and P-SV images have been reasonably adjusted to equivalent depth coordinates (Fig. 14). These maps are an example of depth-registration option 5 (P and S images of geologic structure) listed in the *Depth Registration of P and S Data* section. On the basis of the equivalence of P-P and P-SV depth structure for the top of Strawn horizon, we conclude that comparisons of P-P and P-SV seismic sequences and seismic facies across our interpreted P-P and P-SV Strawn intervals will be comparisons of depth-equivalent stratigraphic intervals. This depth registration of P and S data is perhaps the most essential requirement for any elastic wavefield stratigraphy analysis.

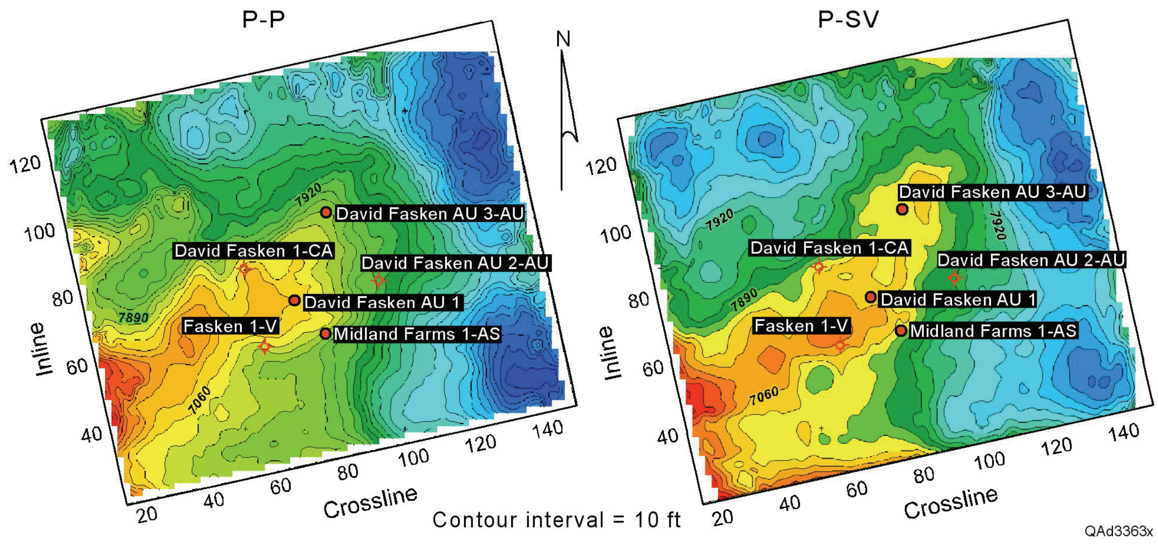

Figure 18. Structural configuration of top of Strawn as interpreted from P-P data (left) and P-SV data (right). Note that some nonproducing wells (open circles) are structurally higher than producing wells (solid circles).

A key message provided by these structure maps is that oil production is not related to the structural position of a well. Six wells were drilled inside the seismic image space before the 3C3D seismic data were acquired. Three wells were producers, and three were nonproducers. Producing wells are indicated by solid circles; nonproducers are labeled with open circles. Inspection of the maps in Figure 18 shows that two of the nonproducing wells are structurally higher than producing wells. The structural relationships among these wells were supported by well logs that confirmed that the structural picture provided by the seismic data is correct. Oil production across this prospect is, therefore, controlled by stratigraphic and facies conditions, not by structure.

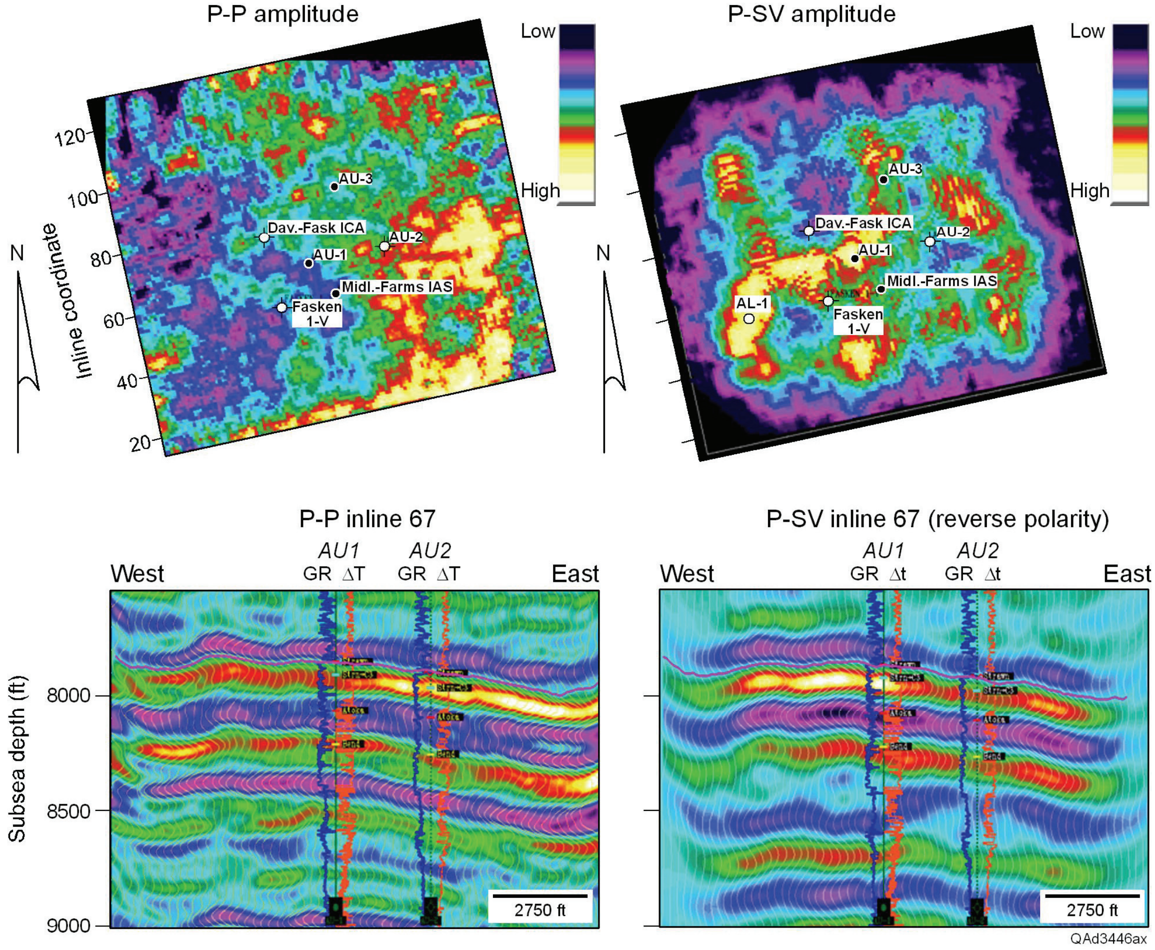

Figure 19. Maps of P-P and P-SV amplitude-based seismic facies (top). Vertical sections through P-P and P-SV data volumes along Inline 67 (bottom) that traverses the center of the maps.

Figure 19 shows one seismic facies (rms amplitude) extracted from narrow, depth-registered windows spanning the reservoir interval across the P-P and P-SV data volumes. The P-P and P-SV data were depth registered using a two-step approach. First, P-P and P-SV structures were adjusted to be approximately depth equivalent (Fig. 18). Second, that registration was then improved by applying a numerical least-squares-minimization technique to more accurately adjust P-SV image time to P-P image time (Fig. 14). The maps in Figure 19 are one example of a modern, computer-generated seismic facies attribute that now replaces the visually determined seismic facies parameters listed in Tables 1 and 2 and that displaces the manual XYZ mapping procedure described in Figure 7. In other West Texas areas, P-P amplitude attributes have successfully delineated productive carbonate reservoirs in the Strawn. Here P-P amplitude facies were not definitive, as an inspection of Figure 19 shows. P-P reflection amplitudes across the image space are random, and P-P amplitudes at nonproducing wells look like P-P amplitudes at producing wells. In contrast, P-SV reflection amplitudes appear to react to productive and nonproductive reservoir conditions.

P-SV data show a sinuous, high-amplitude, seismic facies (yellow/red) that reasonably segregates producing wells from nonproducing wells.

At this prospect, the Strawn reservoir interval is a low-porosity carbonate. Porosity ranges from 1 to 7 percent across the area, and minimum productive porosity is 4 percent. Detecting the narrow porosity range between nonproducing facies (1 to 3 p.u.) and productive facies (4 to 7 p.u.) is beyond seismic detectability for both P-P and the P-SV modes of these particular seismic data. At this prospect, rather than using seismic data to segregate areas of productive porosity from areas of nonproductive porosity, we used P-SV seismic amplitude facies to segregate thicker reservoir intervals from thinner reservoir intervals. The logic was that zones of favorable porosity are more likely to be found across intervals where there is a maximum thickness of the targeted reservoir unit.

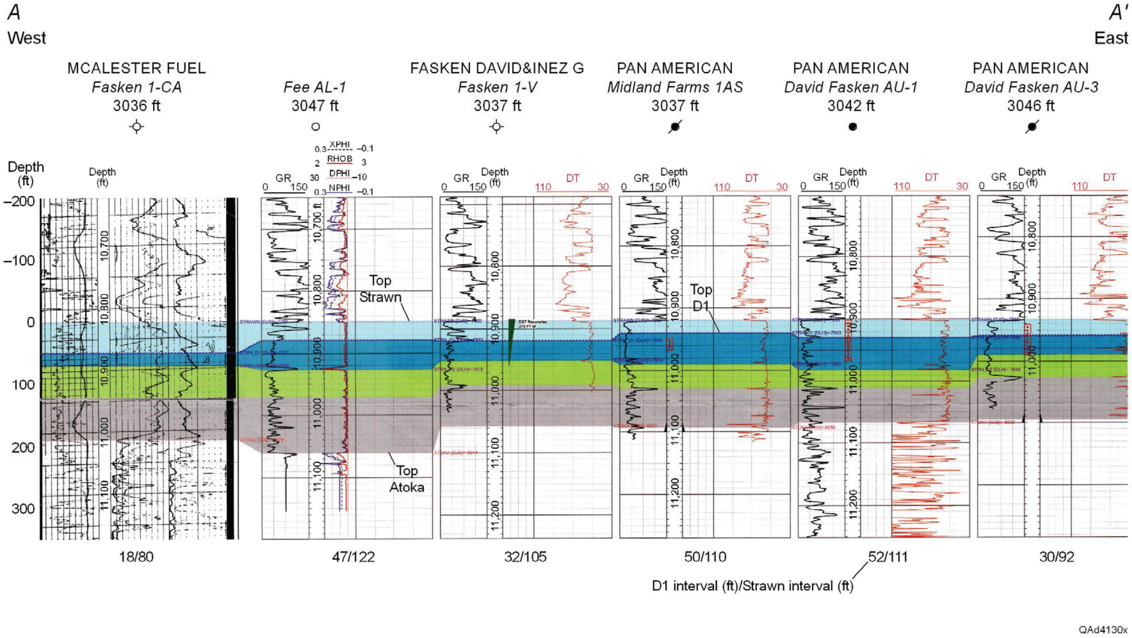

Figure 20. Well log cross section illustrating increased thickness of reservoir facies at well AL-1 (second from left) that was drilled on the basis of elastic wavefield stratigraphy. All log curves are adjusted to a Top Strawn datum. The key facies is dark-blue interval D1. Numbers below each log suite define thicknesses of the D1 unit and the Strawn interval (in feet).

The predictive value of the P-SV seismic amplitude facies was tested by drilling the well labeled AL-1 on the P-SV map (Fig. 19). This well found the thickest reservoir facies (122 ft) of all the wells shown on the map (Fig. 20). From the standpoint of predicting thickness of the reservoir facies, this study supports the use of elastic wavefield stratigraphy for carbonate stratigraphic trap exploration in this particular prospect area in preference to conventional seismic stratigraphy. The P-SV elastic mode defined a maximum-thickness reservoir interval when the P-P seismic mode used in conventional seismic stratigraphy could not. However, even though the P-SV seismic facies successfully predicted an increase in reservoir-interval thickness, the well was still not as productive as desired, showing that there are cutoff limits to reservoir net pay, below which no seismic technology can provide accurate estimates of productive facies.

A second computer-generated P-SV seismic facies is displayed as Figure 21. This attribute is one that numerically matches reflection waveshapes across a defined data window and then defines spatial distributions of look-alike waveforms.

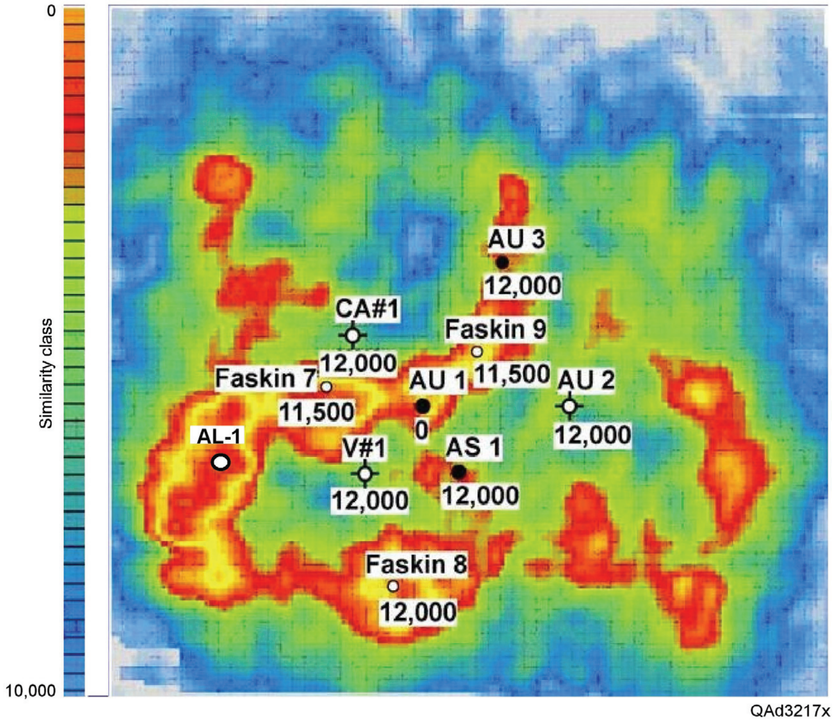

Figure 21. Map of Strawn-interval P-SV reflection waveshapes sorted into similarity classes by commercially available interpretation software. The similarity-class color scale is an arbitrary numbering system. Numerical sorting of reflection waveshapes into distinct waveshape types is a powerful computer-based seismic facies technology. This map emphasizes the trend of P-SV waveshapes that correlate to productive wells (solid circles). Wells CA-1, AU-2, and V-1 are nonproductive wells; wells AS-1, AU-1, and AU-3 are producing wells. Well AL-1 was drilled on the P-SV seismic facies trend; wells 7, 8, and 9 are additional drilling locations being considered.

Algorithms that sort reflection waveshapes into such similarity classes are recent commercial software developments that are of great value in seismic stratigraphy analysis. This attribute map shows that this particular seismic facies (P-SV waveshape at productive wells) segregates productive wells from nonproductive wells better than does the P-SV seismic rms-amplitude facies displayed in Figure 19. The position of Well AL-1 is indicated on the map; wells 7, 8, and 9 are locations where future wells may be drilled.

In this elastic wavefield stratigraphy analysis, we focused on the Strawn carbonate system because that interval was the primary focus of local drilling activity. However, we found marked contrasts between P-P and P-SV seismic sequences and facies across other stratigraphic intervals also. One example at the Wolfcamp level above the Strawn is illustrated in Figure 22. The yellow arrows identify a significant difference between P-P and P-SV reflectivities for the Wolfcamp. We did not make P-P and P-SV seismic facies maps of this interval to determine whether the P-P mode or the P-SV mode provided sequence and facies information that was more valuable than that of its companion mode.

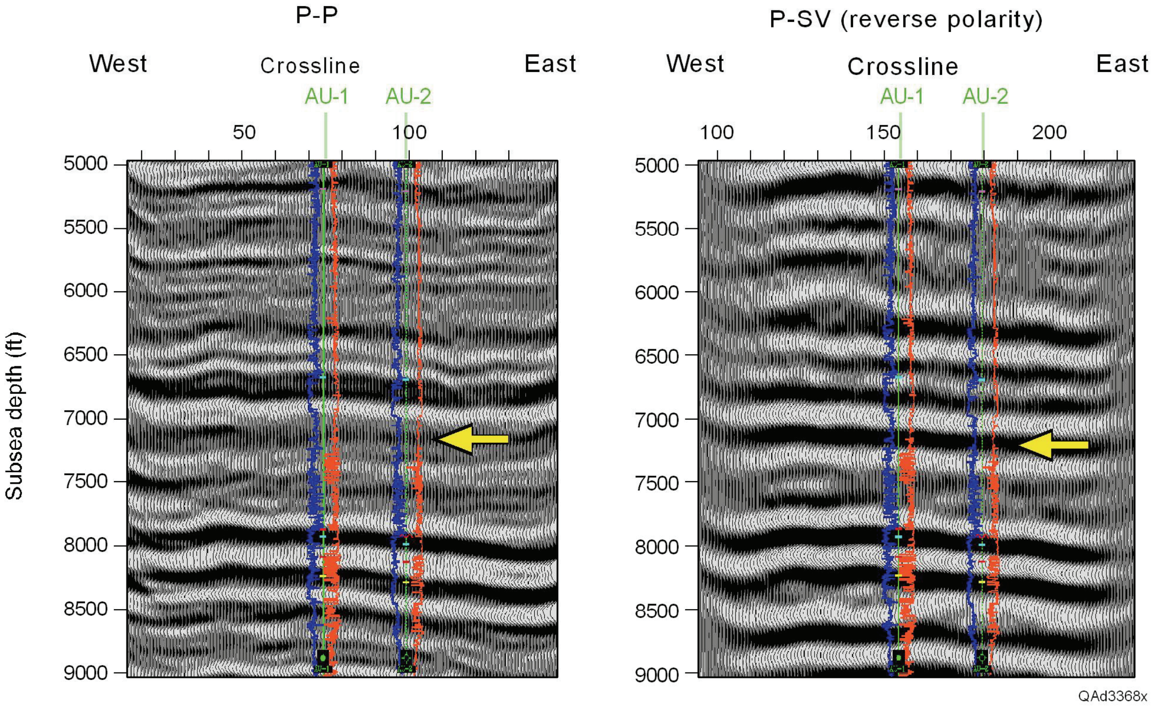

Figure 22. P-P and P-SV images centered on the Wolfcamp (yellow arrows). P-P data exhibit a low-amplitude seismic facies; P-SV data produce a high-amplitude seismic facies.

Both the P-P and the P-SV images across this interval are correct as far as we were able to determine. On the basis of this conclusion, the only principle we wish to document by the data in Figure 22 is that an elastic wavefield stratigraphy analysis (both P-P and P-SV data) will provide a different, and perhaps more valid, geological model of the Wolfcamp than will a conventional seismic stratigraphy analysis (P-P data only). The rock-physics basis for this observed difference in P-P and P-SV reflectivities is explained in Figures 28 and 29.

Rock Physics

Photographs of cores taken from the Strawn interval targeted in this study are shown as Figures 23 and 24. Numerous lithological features, indicators of depositional environments, and effects of diagenetic and tectonic-stress processes are labeled on each core display.

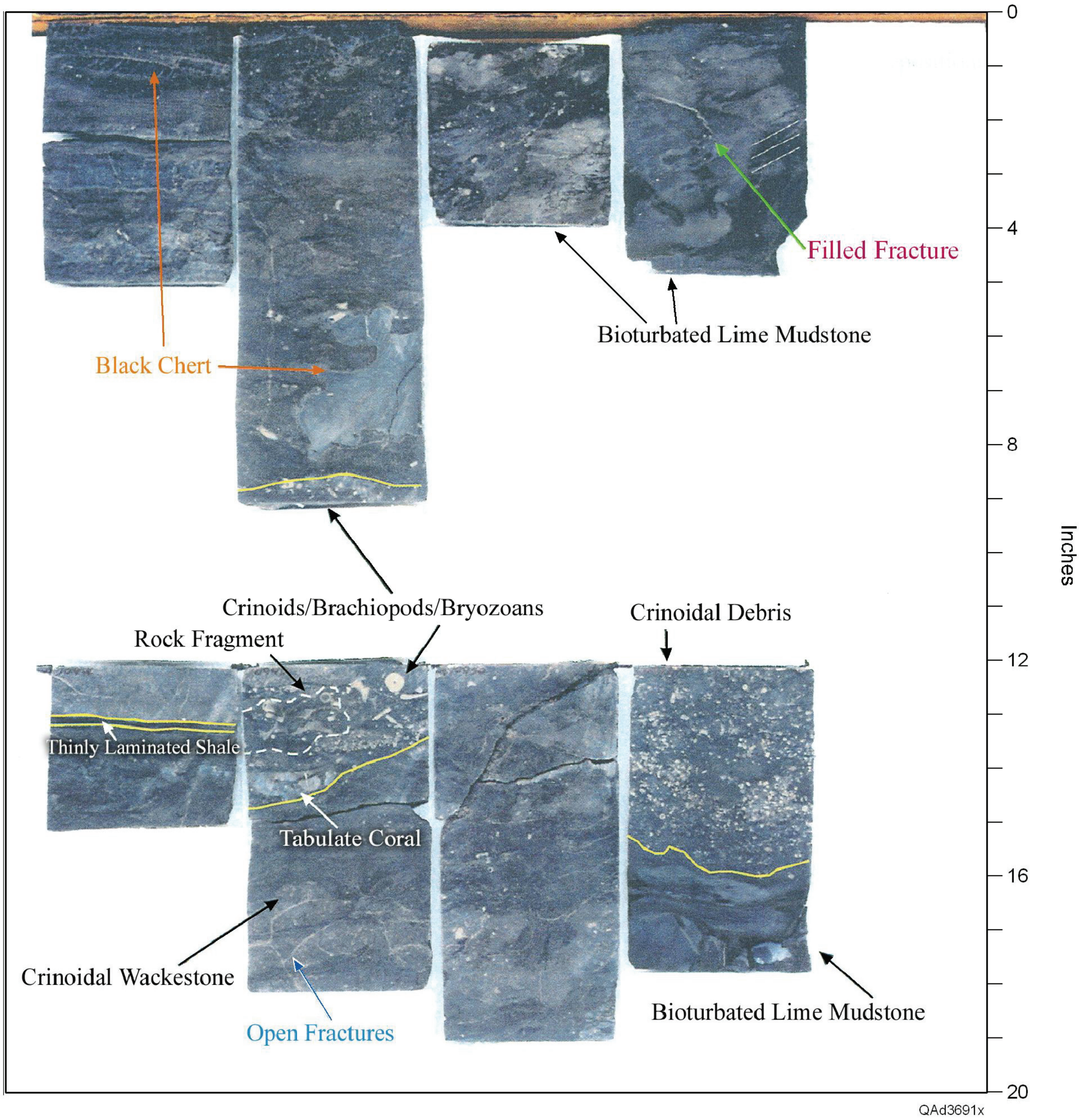

Figure 23. Photographs of Strawn cores across depth interval 10,945 to 10,955 ft of well CA-1. Well location is defined on the maps shown in Figures 18, 19, and 21. Note the length scale along the right margin. Labeled lithofacies interpretations were made by Rotary Laboratories, Inc.

These cores confirm that porosity of the carbonate system is quite low, as stated, and that an appreciable number of fractures, stylolites, and laminations are present across the target interval. Some fractures are open, some are cemented, and others are annealed. These core samples suggest that the fractures are not aligned in a consistent azimuth or dip but are oriented at random angles relative to vertical and to north. Consequently, an isotropic fractured medium, not an orthorhombic medium or a ***horizontal transverse isotropic (HTI)*** medium, seems to be the most appropriate rock-physics model for this Strawn interval.

Taken as a whole, these fractures, stylolites, laminations, and interbedded layers of chert, mudstone, oolites, and other carbonate lithofacies create an anisotropic seismic propagation medium that influences P-P and P-SV reflectivities in different ways, as we will illustrate.

Well logs acquired across the Strawn Formation are displayed as Figure 25. The two S-wave slowness curves Δt_S shown in this log suite are synthetic curves calculated using the equations specified in the figure, together with the P-wave slowness curve Δt_P and gamma-ray curve GR acquired in the AU-1 well (well location shown in Figures 18, 19, and 21). The Δt_S equations were determined by cross-plotting P-wave slowness, S-wave slowness, and gamma-ray data acquired in a well away from the seismic survey area, but which penetrated a lithofacies similar to the Strawn. Actual Δt_S log data were acquired in the AL-1 well, but we used this synthetic Δt_S curve rather than the actual Δt_P curve acquired in the AL-1 well in our rock-physics analysis of P-P and P-SV reflectivities because hole washouts in the AL-1 well affected measured Δt_S values and because the pseudo-Δt_S log was a close match to the real Δt_S log from the AL-1 well across intervals where reliable Δt_S log data were acquired.

Raw log data across the Strawn Formation are shown in Figure 26, with averaged curves superimposed on Δt_P, Δt_S, and ρ_b tracks. Volumetric averaging was used to create the average ρ_b trend; Backus averaging was used to estimate average trends of bulk modulus and shear modulus (Backus, 1962). Resulting interval values of V_P, V_S, and ρ_b were then combined with the Hudson (1981) theory of isotropic fractured media and Zoeppritz's equations (1919) to calculate P-P and P-SV reflectivities. These reflectivity curves are displayed in Figure 27. The analysis shows that for this low-porosity carbonate, isotropic fracturing causes a negligible change in P-P and P-SV reflectivity. Fractured Strawn intervals will have P-P and P-SV seismic facies character identical to the P-P and P-SV seismic facies character of nonfractured Strawn intervals.

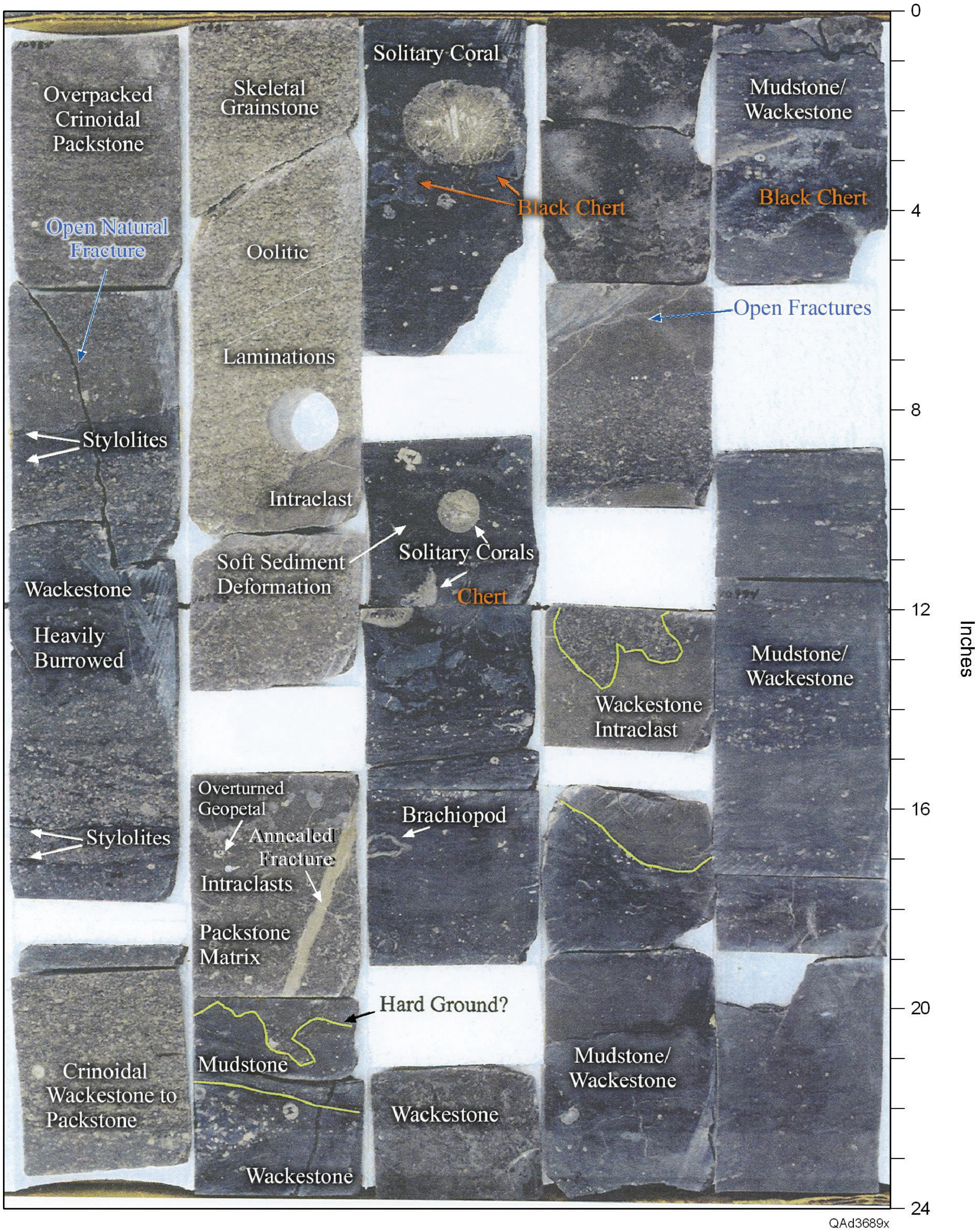

Figure 24. Photographs of Strawn cores across depth interval 10,985 to 10,995 ft of well CA-1. Length scale is shown along the right margin. Labeled lithofacies interpretations were made by Rotary Laboratories, Inc.

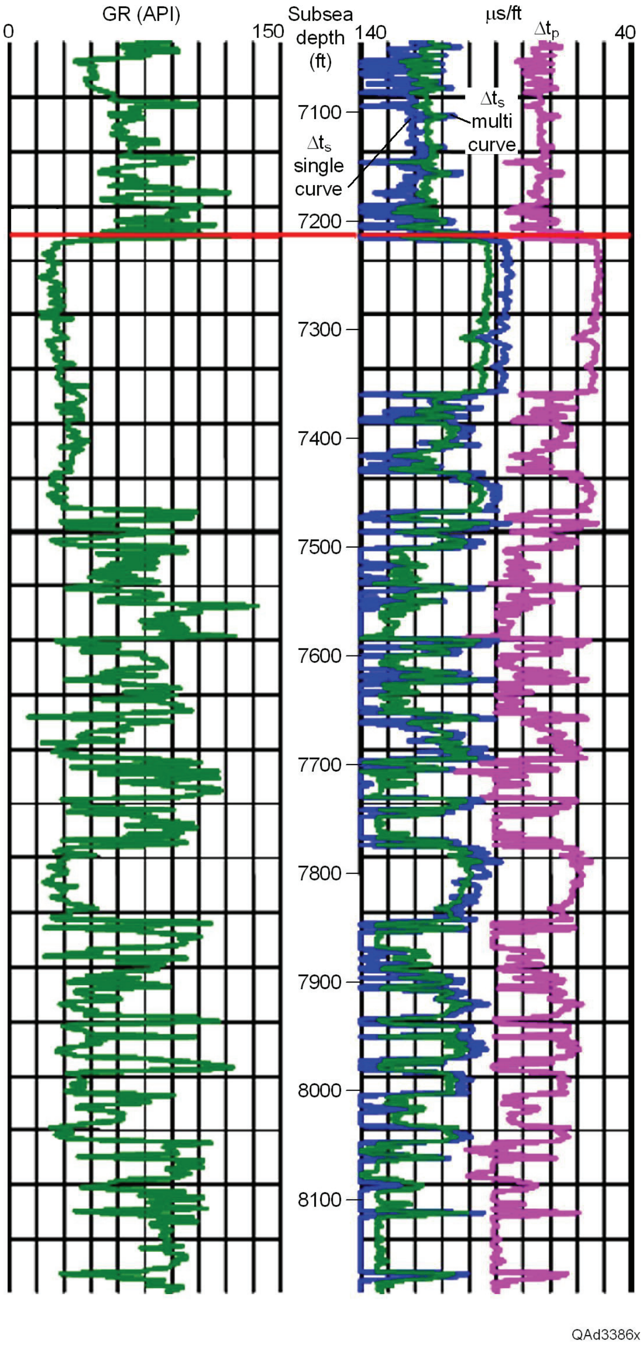

Single curve:
$\Delta t_s = 12.24 + 1.15\,(\Delta t_p) + 0.0086\,(\Delta t_p)^2$ if $GR < 25$
$\Delta t_s = -417.94 + 24.48\,(\Delta t_p) - 0.402\,(\Delta t_p)^2 + 0.0023\,(\Delta t_p)^3$
if $GR \geq 25$

Multi curve:
$\Delta t_s = 46.04 + 1.094\,(\Delta t_p) - 0.017\,(GR)$

Figure 25. Δt$_P$, Δt$_S$, and gamma-ray (GR) log data across the low-porosity Strawn carbonate facies. The two Δt$_S$ log curves were calculated from Δt$_P$ and GR log responses using each of the two equations written beside the log curves.

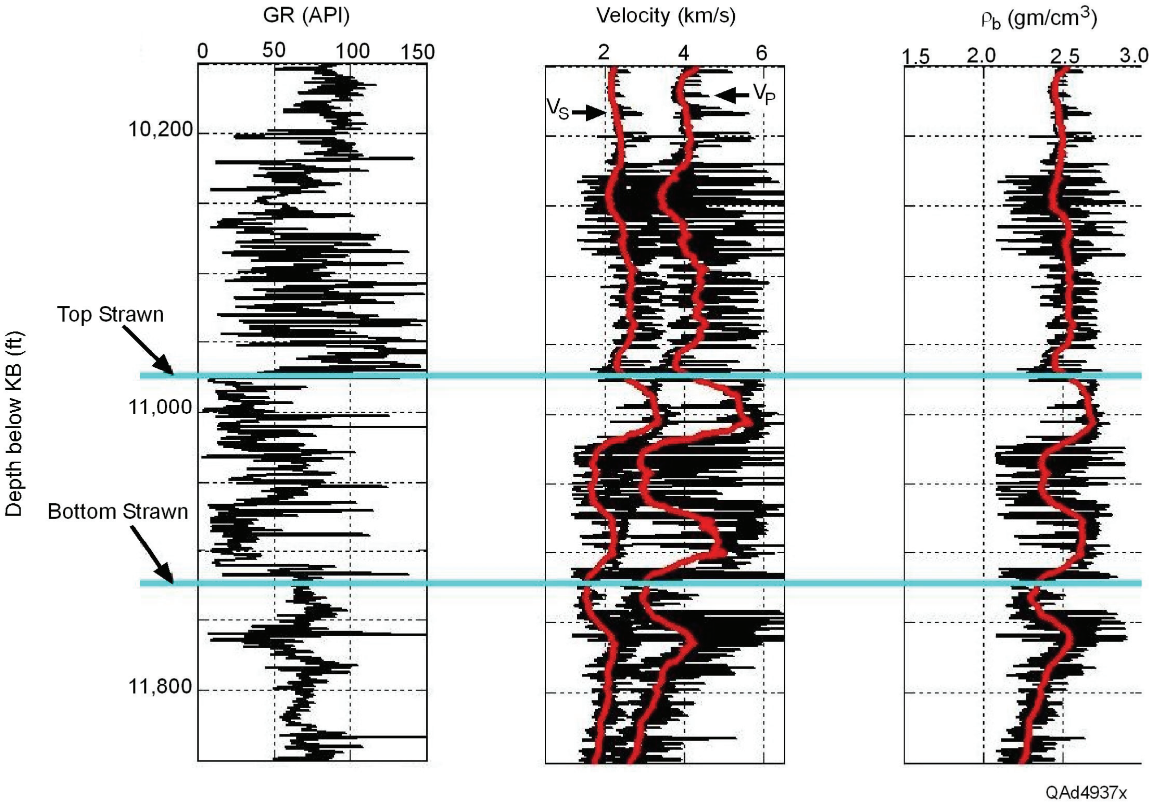

Figure 26. Averaged Δt_P, Δt_S, and ρ_b log curves (red) across the Strawn. Data acquired in the AL-1 well.

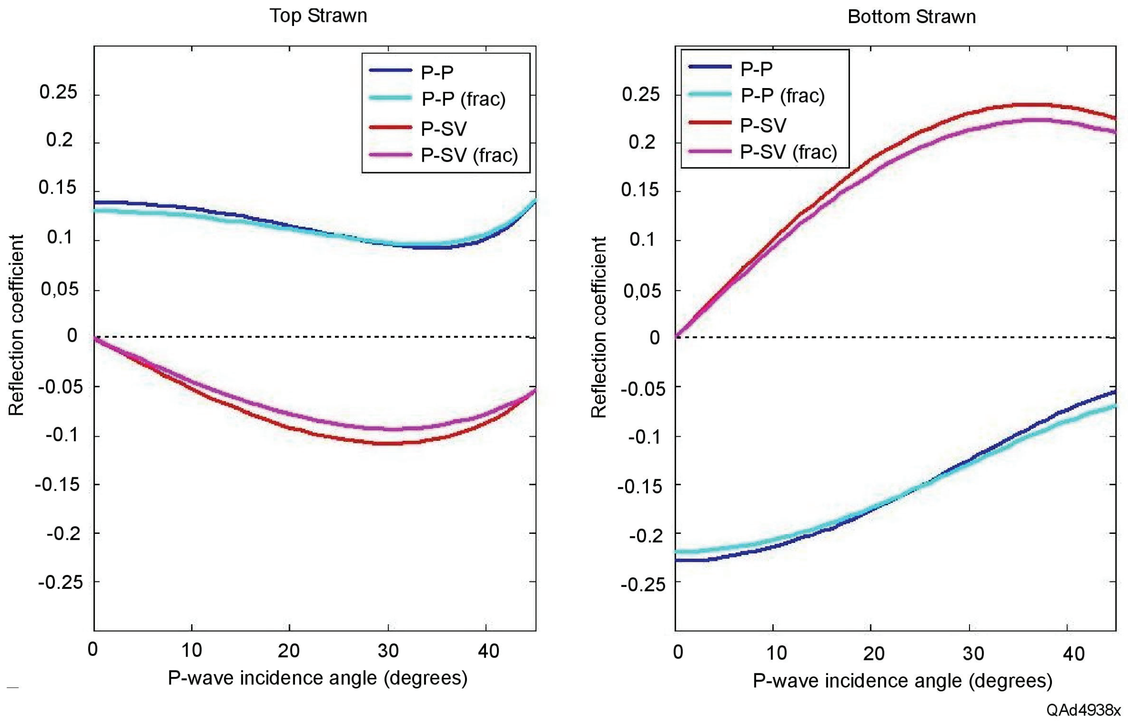

Figure 27. Effect of isotropic fracturing on P-P and P-SV reflectivities from the Strawn interval. Hudson's theory (1981) was used to model the effect of isotropic fracturing.

Well log data across the Wolfcamp interval are displayed in Figure 28. To analyze the difference between P-P and P-SV seismic amplitude facies exhibited by the P-P and P-SV images in Figure 22, we analyzed reflectivity behaviors at the interface shown at a KB depth of approximately 10,300 ft on these log curves. V_P, V_S, and ρ_b values were averaged across the 300-ft intervals immediately above and below this interface, and these average rock properties were then used to calculate the reflectivity curves shown in Figure 29. These curves confirm that P-SV reflectivity is greater than P-P reflectivity when both reflectivity curves are evaluated over all possible incidence angles. For example, P-P reflectivity exceeds 0.04 only for incidence angles between 0 and 15º, but P-SV reflectivity has a magnitude greater than 0.04 for incidence angles between 15º and 45º, an angle range that is twice as large as that of the high-amplitude P-P response. Because the 3C3D seismic data involved in this study were acquired with a full range of incidence angles, the difference in P-P and P-SV amplitude facies shown in Figure 22 has a valid rock-physics basis. P-P amplitudes should be weaker than P-SV amplitudes (Fig. 29), and that behavior is what is exhibited by the data in Figure 22.

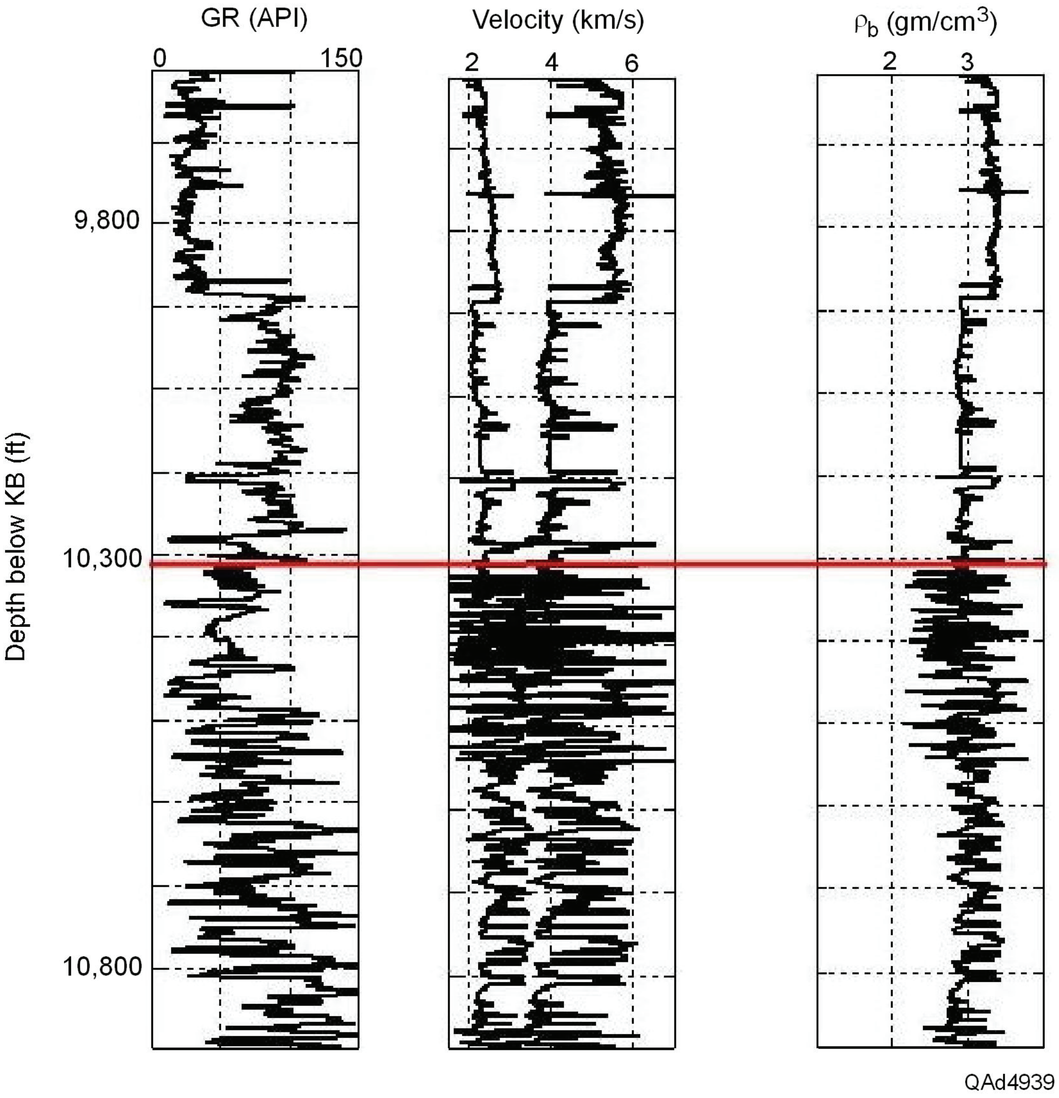

Figure 28. Log data across the Wolfcamp interval in the AU-1 well (9,714 to 10,902 ft KB). Wolfcamp reflectivity was evaluated at the interface drawn at approximately 10,300 ft.

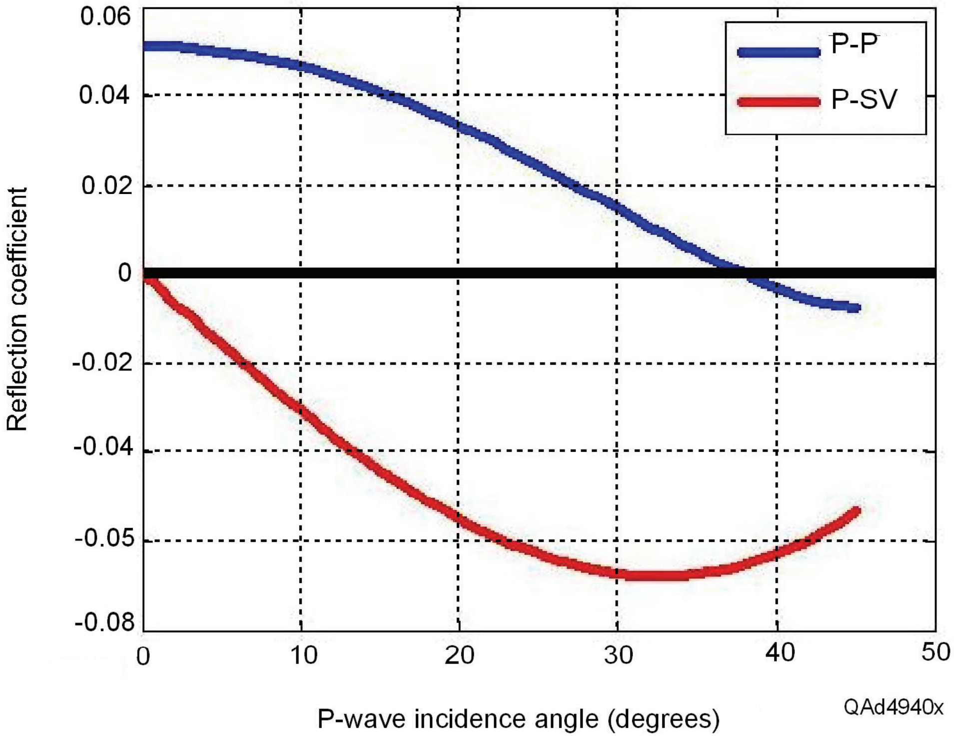

Figure 29. P-P and P-SV reflectivities of the Wolfcamp interface at approximately 10,300 ft, shown in Figure 28.

Fizz-Gas and Commercial-Gas Sandstone Reservoirs

P and S Sequences and Facies

Fizz-gas and commercial-gas reservoirs look identical in stacked or migrated P-P seismic images. The failure of P-wave-based conventional seismic stratigraphy to distinguish between these two gas saturations has frustrated efforts by operators across the Gulf of Mexico to avoid drilling fizz-gas targets for decades. A solution to this problem of segregating fizz-gas reservoirs from commercial-gas reservoirs appears now to be available through the use of elastic wavefield stratigraphy. Specifically, when marine 4C OBC seismic data are used to illuminate gas reservoirs, the P-SV image constructed from these data provides the key seismic amplitude attribute that distinguishes between fizz-gas and commercial-gas reservoirs.

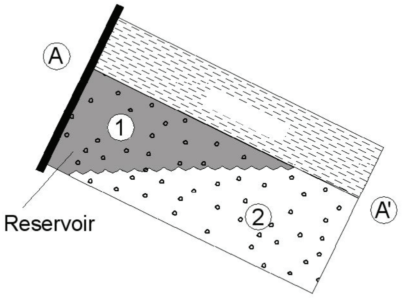

Key lateral changes (A to A'):

$\Delta V_P = V_P(2) - V_P(1)$

$\Delta V_S = V_S(2) - V_S(1)$

$\Delta \rho = \rho(2) - \rho(1)$

Reservoir	ΔV_P	$\Delta \rho$	ΔV_S
No gas (S_w ~ 100%)	Modest	Modest	Modest
Fizz gas (S_w ~ 80%)	Large	Modest	Modest
Commercial gas (S_w ~ 10%)	Large	Large	Modest

QAd4408x

Figure 30. Lateral changes in petrophysical properties that control P-P and P-SV reflectivities across fluid contact boundaries. V_p is P-wave velocity, V_S is S-wave velocity, and ρ is bulk density.

Petrophysical properties that need to be considered when applying 4C OBC seismic technology to gas exploration are summarized in Figure 30. This figure shows a reservoir interval (labeled 1) overlying a water-saturated sandstone (labeled 2). Variations in bulk density ρ and in velocities V_P and V_S are tabulated for three reservoir conditions: water, fizz gas, and commercial gas. Comments in the table describe changes in bulk density and seismic velocity that occur within the target layer as the seismic imaging moves along horizon A-A′ and crosses the fluid contact boundary that separates region 1 (reservoir) from region 2 (nonreservoir).

If equations for P-P and P-SV reflectivities are reduced to their simplest forms, P-P reflectivity is found to be a function of Δρ, ΔV_P, and ΔV_S—parameters listed in Figure 30. In contrast, P-SV reflectivity is a function of only Δρ and ΔV_S (Aki and Richards, 1980). This distinction, that ΔV_P influences P-P reflectivity but not P-SV reflectivity, is important in this application.

Seismic reflectivity along interface A-A′ is critical to interpreting pore fluid conditions within the reservoir unit. For both commercial-gas and fizz-gas conditions, the lateral change in P-P reflectivity along horizon A-A′ will be large where the seismic image transitions from reservoir to nonreservoir conditions because the lateral change ΔV_P in P-wave velocity is large across the fluid-contact boundary for both high- and low-gas saturations (table in Figure 30). As a result, both commercial-gas and fizz-gas targets look identically bright in stacked and migrated P-P seismic images used in conventional seismic stratigraphy. Keeping in mind that P-SV reflectivity is influenced by only Δρ and ΔV_S (Aki and Richards, 1980), note that a second concept documented in Figure 30 is that the lateral change in P-SV reflectivity will be rather large across the fluid-contact boundary only if the reservoir contains a commercial saturation of gas because $\Delta\rho$ is large only in this situation. Of the three reservoir options listed in Figure 30, a significant lateral change in bulk density occurs across the fluid-contact boundary only for a high-gas-saturation condition. For a fizz-gas reservoir, the lateral variation in P-SV reflectivity will be small or nonexistent because neither bulk density ρ nor S-wave velocity V_S varies significantly as the pore-fluid conditions change laterally from fizz water to 100-percent pore water. In elastic wavefield stratigraphy, commercial gas should thus appear brighter in P-SV images than fizz gas does.

To confirm these principles, P-P and P-SV images across a commercial-gas reservoir and a fizz-gas reservoir are shown in a side-by-side display in Figure 31. The fizz-gas reservoir (panel b) is a bright spot in the P-P image, compared with the P-P image background, but there is no corresponding anomaly in the P-SV image. The commercial-gas reservoir (panel a) is also a bright spot in the P-P image when compared to the image background, illustrating that it is impossible to use the P-P images of Figure 31 (conventional seismic stratigraphy) to distinguish fizz gas from commercial gas. However, the commercial-gas reservoir in Figure 31a creates a modest amplitude anomaly in P-SV image space compared with the background reflectivity. This P-SV reflectivity behavior is predicted by the large lateral variation in bulk density $\Delta\rho$ listed for a commercial-gas target in Figure 30. The difference between the P-SV seismic amplitude facies across a commercial-gas reservoir and the P-SV seismic amplitude facies across a fizz-gas reservoir shown in Figure 31 allows fizz-gas targets to be distinguished from commercial-gas targets rather successfully when elastic wavefield stratigraphy is used rather than conventional seismic stratigraphy.

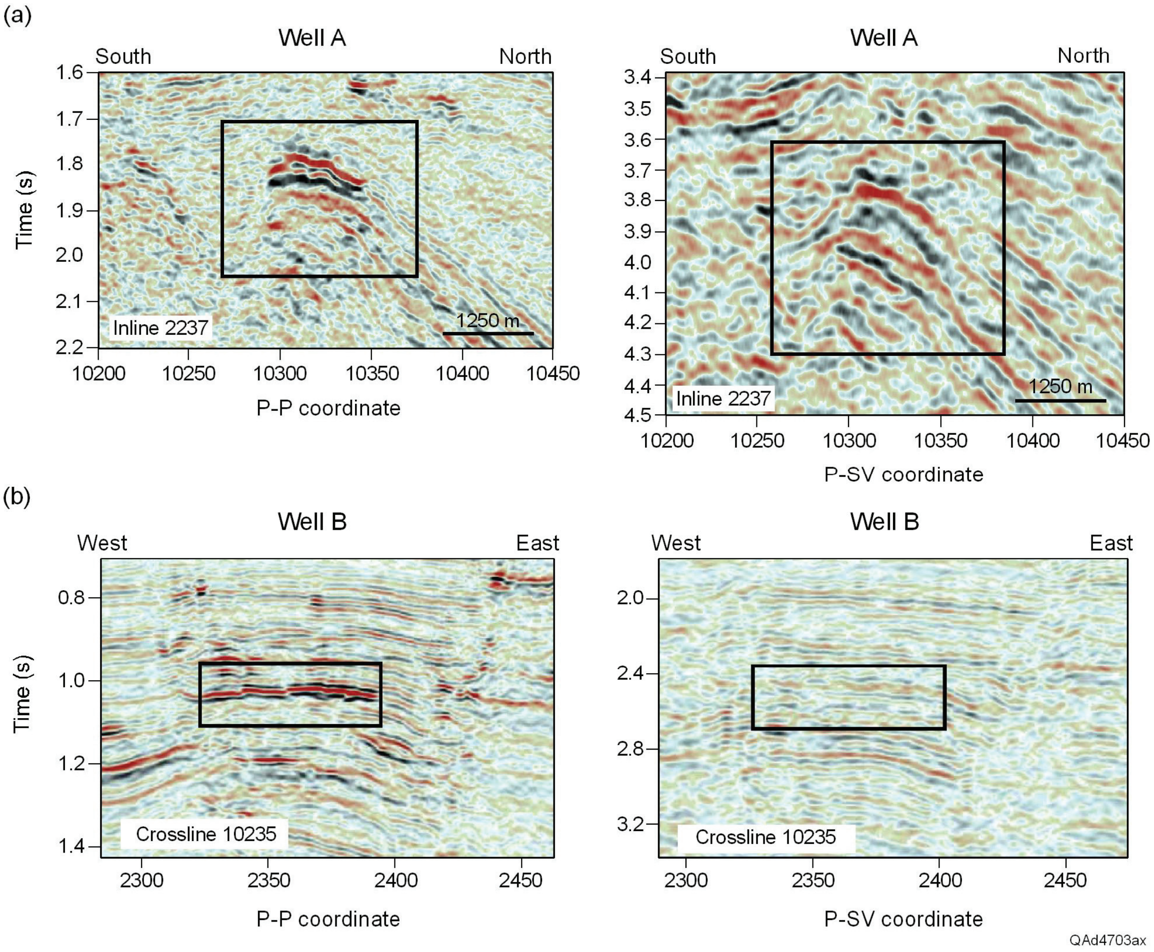

Figure 31. Comparisons of P-P (left) and P-SV (right) reflectivities across (a) a commercial-gas reservoir that was producing at the time the seismic data were acquired and (b) a fizz-gas reservoir drilled after the seismic survey was completed. Rectangular windows are centered on the reservoirs.

During this study, we applied these principles of elastic wavefield stratigraphy across several Gulf of Mexico gas reservoirs and found the results documented in Figure 31 to be consistent in all cases. A second example of one of our elastic wavefield stratigraphy studies of commercial-gas and fizz-gas reservoirs is illustrated in Figure 32.

Rock Physics

Effects of fluid substitution on log data acquired in a well that penetrated one of the commercial reservoirs shown in these two examples are illustrated in Figure 33. All fluid substitutions were done in sand intervals using Gassman's theory (1951) to adjust the logs. Three pore-fluid conditions were constructed for the sands:

1. brine (S_w = 100 percent),
2. commercial gas (S_W = 15 percent), and
3. fizz gas (S_w = 85 percent).

Inspection of saturation-dependent log curves shows that V_P and V_S do not change, or change by only a minor amount, as gas concentration varies from 85 to 15 percent. In contrast, bulk density is significantly different for fizz-gas and commercial-gas saturations but varies in only a minor way when fizz-gas replaces brine water. These log behaviors support the ΔV_P, ΔV_S, and $\Delta\rho$ principles summarized in the table of Figure 30.

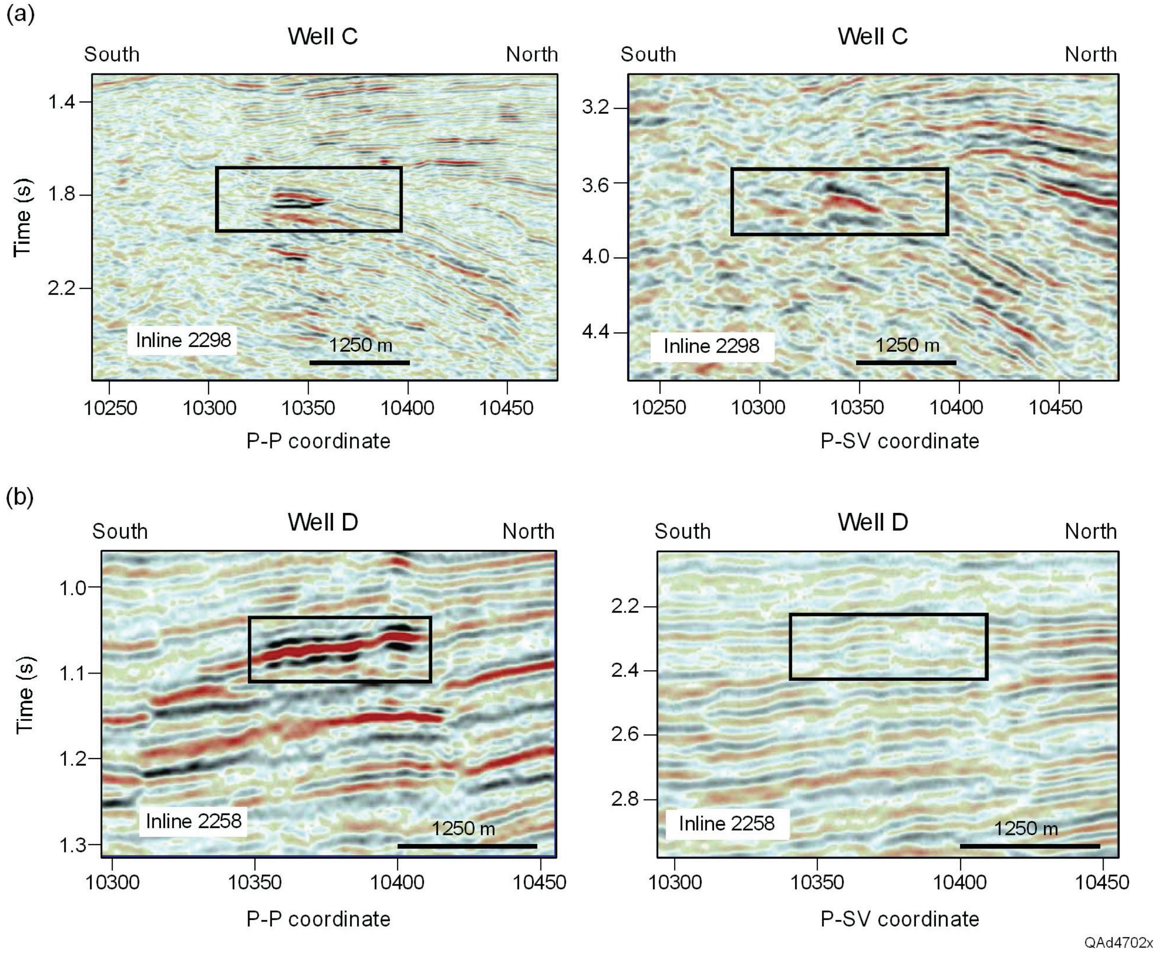

Figure 32. A second example of comparisons between P-P (left) and P-SV (right) reflectivities across (a) a commercial-gas reservoir that was producing at the time the seismic data were acquired and (b) a fizz-gas reservoir drilled after the seismic survey was completed. Both commercial- and fizz-gas reservoirs create P-P anomalies (left column). Only a commercial-gas reservoir creates a P-SV anomaly (right).

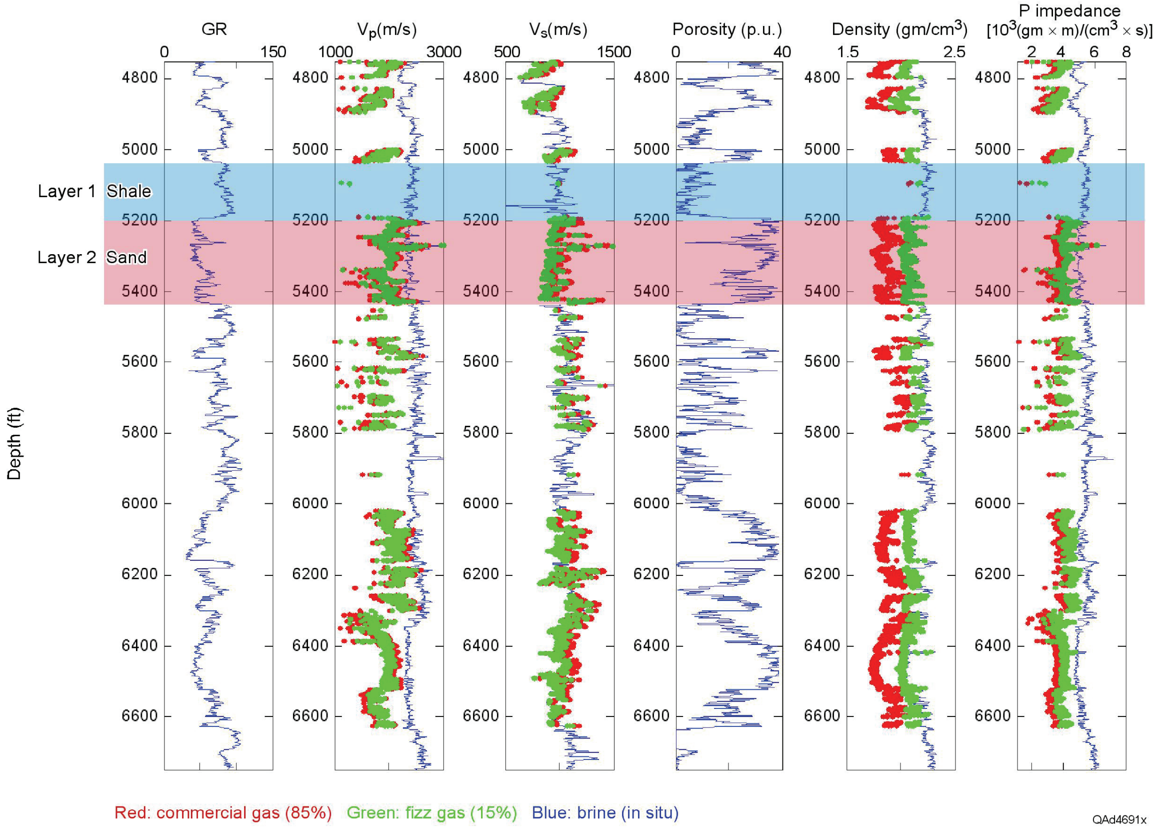

Figure 33. Fluid-substitution adjustments of sand intervals penetrated by a well on one of the profiles shown as Figures 31 and 32. Red = commercial gas (S_W = 15 percent), green = fizz gas (S_W = 85 percent), and blue = brine water (S_W = 100 percent). Data from Layers 1 and 2 were used to model AVA behaviors for P-P and P-SV modes that illuminate commercial-gas and fizz-gas reservoirs.

Two data windows labeled *Layer 1* and *Layer 2* are identified across the log curves in Figure 33. Layer 1 is a shale interval; Layer 2 is a sand interval. Rock property variations across the interface between these two layers were used to calculate AVA behaviors for commercial-gas and fizz-gas reservoirs. AVA reflectivity curves for the P-P and P-SV modes are shown in Figure 34. In these calculations, water saturation was assumed to be 10 percent for commercial gas and 90 percent for fizz gas rather than 15 and 85 percent, as was used in the fluid substitutions in Figure 33. It was also assumed that the shale in Layer 1 was isotropic.

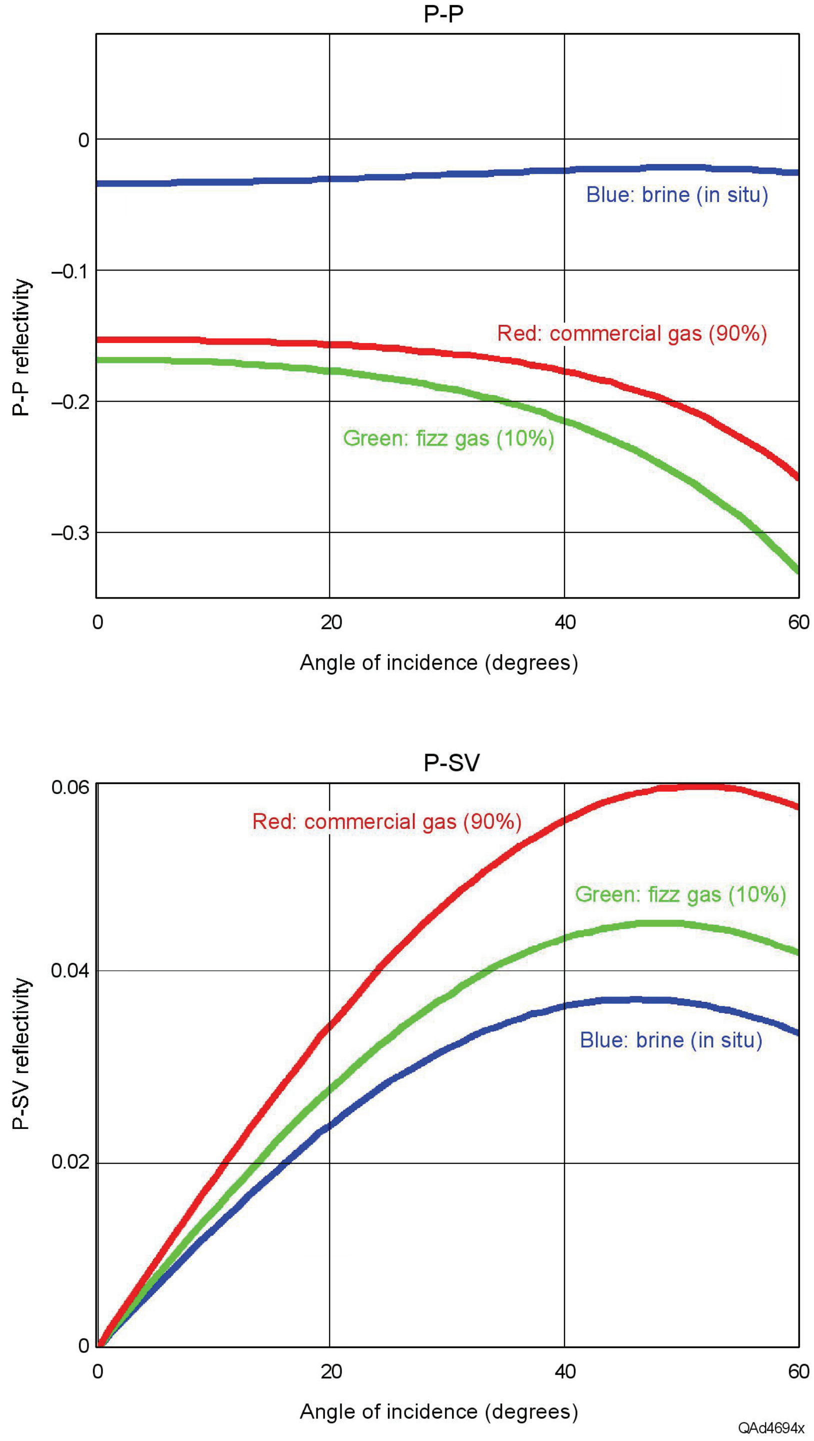

Figure 34. Comparison of AVA behaviors for P-P and P-SV modes. Algebraic signs of P-P and P-SV reflectivity are opposite for the Layer1/Layer 2 interface, as is the situation across most interfaces. Note the opposing behavior of P-P and P-SV reflectivity at large angles of incidence. For the P-P mode, a fizz-gas target is slightly brighter than a commercial-gas target, but the opposite is true for the P-SV mode, where a commercial-gas target is slightly brighter than a fizz-gas target.

These curves explain the principles of elastic wavefield stratigraphy illustrated in Figures 31 and 32. Note that P-P reflectivity (top panel) increases significantly when any amount of gas concentration is present, which is why P-P amplitude anomalies occur for both gas saturations in Figures 31 and 32. Note also that P-SV reflectivity (bottom panel) for a commercial-gas target is greater than P-SV reflectivity for a fizz-gas target, causing P-SV images of a commercial-gas reservoir to exhibit a modest amplitude anomaly, but a fizz-gas reservoir to have a lesser anomaly (Figs. 31, 32).

There are other important differences between the P-P and P-SV reflectivities. First, P-P and P-SV reflection coefficients have opposite algebraic signs, which is the common behavior of P-P and P-SV reflectivities at most interfaces. Second, P-SV reflectivity is always zero at normal incidence, but P-P reflectivity is not. Third, P-SV reflectivity at large angles of incidence differs from P-P reflectivity in that in P-SV data, commercial-gas reservoirs are slightly brighter than fizz-gas reservoirs, but in P-P data, the opposite effect occurs and a fizz-gas reservoir is slightly brighter than a commercial-gas reservoir. Thus, AVA behaviors involved in elastic wavefield stratigraphy are significantly different than those in conventional seismic stratigraphy (P-P data only).

Fracture Systems

P and S Sequences and Facies

Most rocks are anisotropic, meaning that their elastic properties are different when measured in different directions. For example, elastic moduli measured perpendicular to bedding differ from elastic moduli measured parallel to bedding (Fig. 15), and moduli measured parallel to elongated and aligned grains differ from moduli measured perpendicular to that grain axis. Because elastic moduli affect seismic propagation velocity, seismic wave modes react to rock anisotropy by exhibiting direction-dependent velocity, which in turn creates direction-dependent reflectivity.

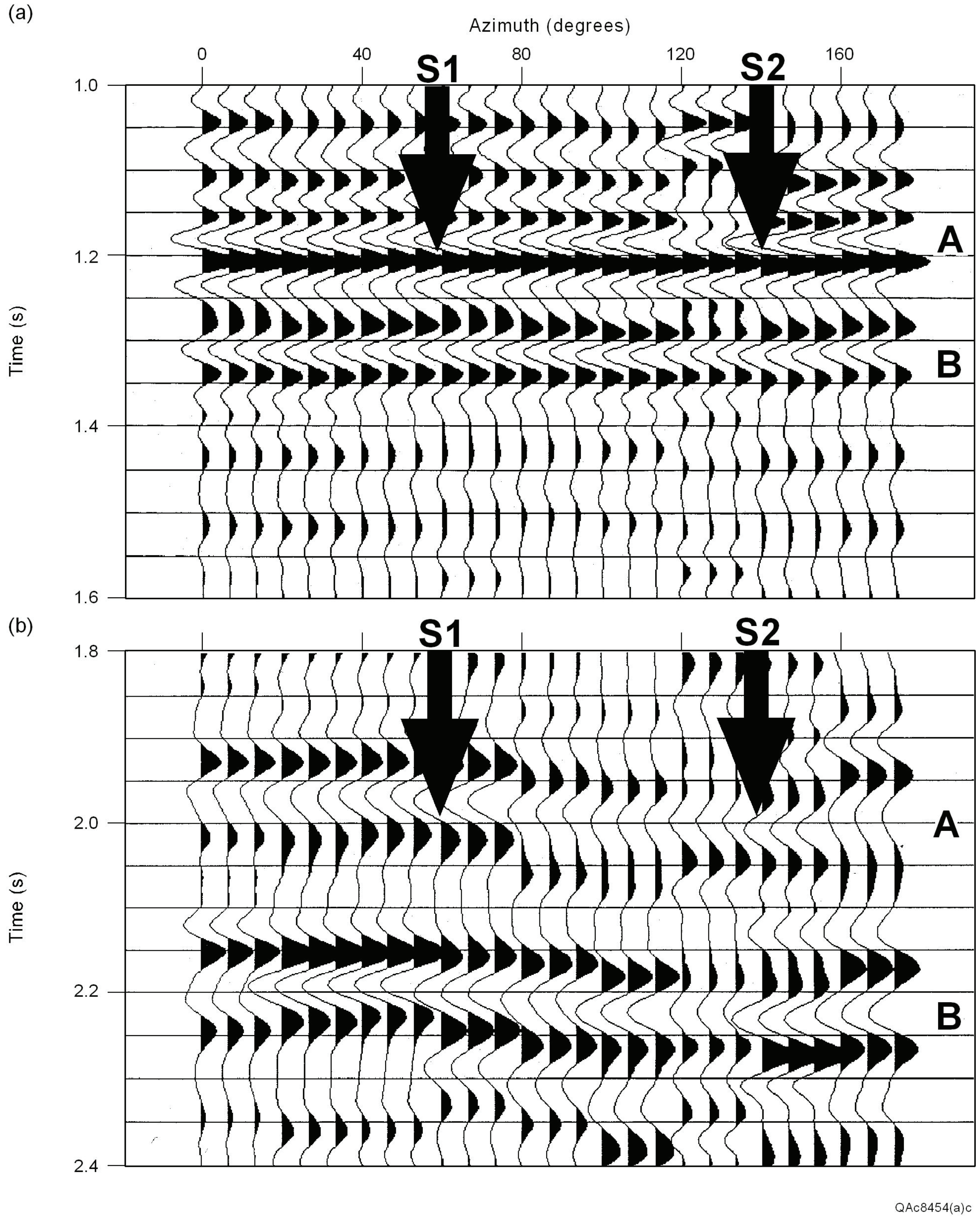

Figure 35. (Top) Azimuth-dependent P-P arrival time and reflectivity from fracture targets **A** and **B**. (Bottom) Azimuth-dependent P-SV arrival time and reflectivity from the same targets. P-P reflectivity changes little with azimuth; P-SV reflectivity varies significantly. P-P arrival time changes by 4 ms between azimuths 50° and 140°, whereas P-SV arrival time changes by 50 ms. Azimuth 50° is the fast-S mode (S1); azimuth 140° is the slow-S mode (S2).

Tests by numerous people have shown that shear (S) waves have greater sensitivity to rock anisotropy than do compressional (P) waves (for example, Lynn, 2004). One of our research objectives is to cause elastic wavefield stratigraphy to be used to evaluate fracture systems, one of the most common types of rock anisotropy.

The prospect investigated in our study described here involved two fractured carbonate intervals at a depth of a little more than 1,800 m (6,000 ft). A small 5.75-km^2 (2.25-mi^2) 3-component 3D (3C3D) seismic survey was acquired to determine whether P-P and P-SV data could be used to determine fracture orientation for optimal positioning of a horizontal well. Figure 35 shows a P-P and P-SV azimuth-dependent data analysis done in a superbin near the center of this survey. At this superbin location, common-azimuth gathers of P-P and P-SV data extending from 0 to 2000-m offsets were made in narrow, overlapping, 20º azimuth corridors. In each of these azimuth corridors, the far-offset traces were excellent quality and were summed to make a single trace, showing arrival times and amplitudes of the reflection waveforms from the two fracture target intervals **A** and **B**. To aid in visually assessing the character of these far-offset summed traces, each summed trace is repeated three times inside its azimuth corridor range in the display format used in Figure 35.

Inspection of these azimuth-dependent data shows two important facts: (1) P-SV waves arrive earliest in the azimuth corridor centered about 50º east of north (the fast-S mode, S1) and latest in an azimuth direction about 140º east of north (the slow-S mode, S2) and (2) P-SV waves exhibit a greater variation in arrival times and amplitudes than do their companion P-P waves. For example, P-P reflectivity from interval **A** is practically constant in all azimuth directions, whereas P-SV reflectivity varies significantly with azimuth. Likewise, P-P arrival time of event **A** changes by only 4 ms between azimuth directions 50º and 140º, but P-SV arrival times change by almost 50 ms, an order of magnitude greater than the variation in P-P arrival times.

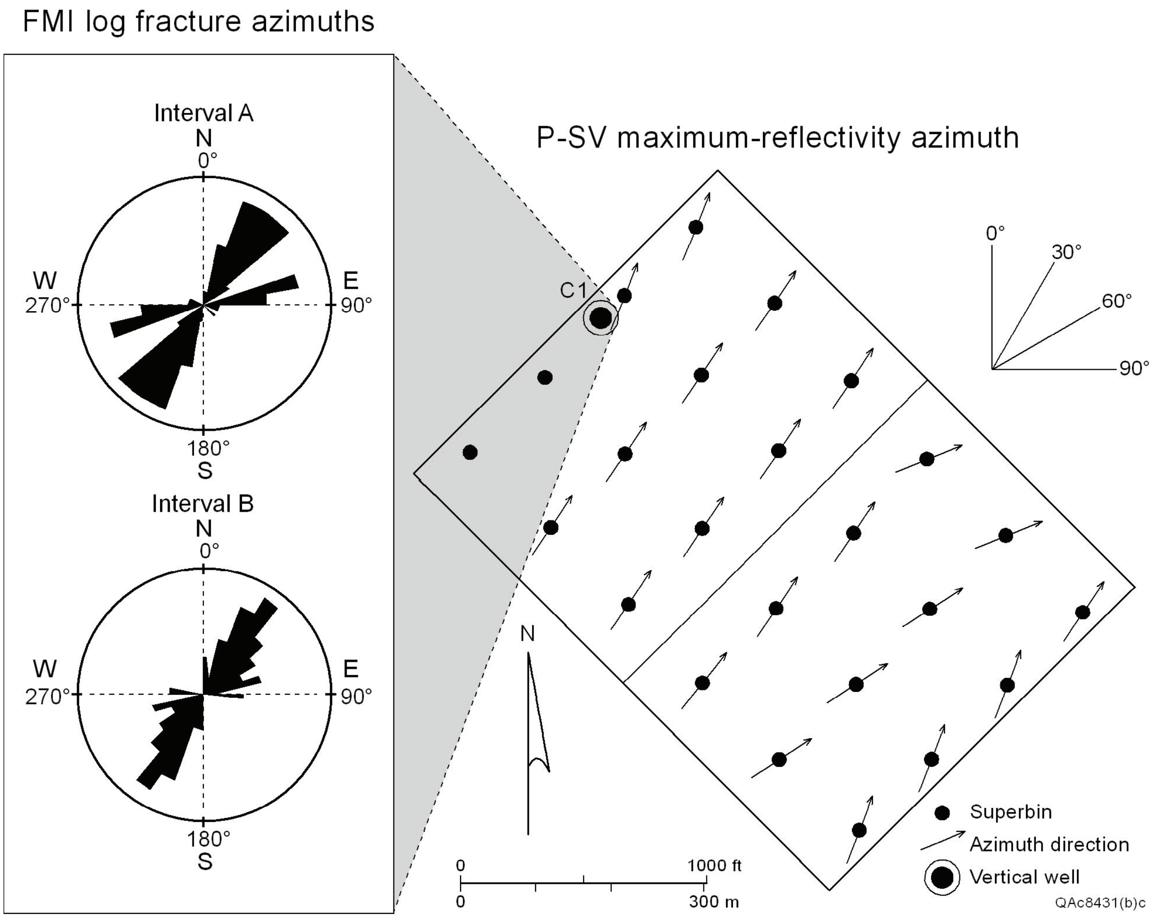

Figure 36. An azimuth-dependent analysis of P-SV data similar to that shown in Figure 35 was done at each location having a solid circle with an accompanying short arrow. Each arrow shows the local azimuth in which P-SV reflectivity from interval **A** was a maximum. Rose diagrams show fracture azimuths across intervals **A** and **B** as interpreted from FMI log data acquired in well C1. S-wave-based fracture azimuths agree closely with FMI-based fracture azimuths and allow fracture orientation to be extended across seismic image space.

Azimuth-dependent trace gathers like these were created at many locations across the seismic image space, and azimuths in which P-SV reflection amplitudes from fracture intervals **A** and **B** were maximal were determined at each analysis location to estimate fracture orientation for each interval. A map of S-wave-based azimuth reflection behavior for interval **A** in the vicinity of calibration well C1 is displayed as Figure 36. Shown as rose diagrams beside this map are fracture orientations across the two reservoir intervals as interpreted by a service company using ***Formation Multi-Imaging (FMI)*** log data acquired in well C1. S-wave estimates of fracture orientations are shown as short arrows at analysis sites near the well. This S-wave-generated map indicates the same fracture orientations interpreted from the FMI log data.

On the basis of the close correspondence between FMI and S-wave estimates of fracture orientation, the operator used S-wave estimates of fracture azimuths across the total seismic image space (an area ~8 times larger than the area shown in Fig. 36) to position and orient a horizontal well trending perpendicular to seismic-based fracture orientation. This well found the S-wave estimates of fracture orientation to be accurate across a drilled lateral distance of approximately 1,000 m and serves as a real-world example of the value of elastic wavefield stratigraphy for evaluating fracture prospects. In this instance, elastic wavefield stratigraphy provided fracture information that could not be extracted from P-wave data used in conventional seismic stratigraphy (Fig. 35). We conclude that application of elastic wavefield stratigraphy technology across fracture prospects should be widely practiced.

Figure 35 shows that in a fractured medium, a P-SV mode segregates into S1 and S2 modes and that the azimuth directions in which these S1 and S2 modes orient their displacement vectors differ by 90º. Knowing the polarization directions of these modes across this prospect area, we processed the 3C3D seismic data to create 3D S1 and S2 data volumes. Procedures used to segregate the 3C3D data into these two elastic wavefield volumes will not be discussed.

We show as Figure 37 a vertical slice from the S1 volume and the corresponding vertical slice from the S2 volume. The two fractured carbonate intervals **A** and **B** are labeled on each display, as well as several horizons interpreted near these two reservoir intervals. Differences between these elastic wavefield images follow.

1. Reflection events **A** and **B** arrive approximately 50 ms earlier in the S1 domain than they do in the S2 domain.
2. At certain image coordinates, there are differences between magnitudes of S1 and S2 reflection amplitudes from targets **A** and **B**. Two obvious examples are labeled SR1 and SR2. The units that bound fracture intervals **A** and **B** have seismic impedances that are less than the impedances of units **A** and **B**. This statement applies to most fractured targets and their bounding units. S1 and S2 reflectivities across targets **A** and **B** are controlled by magnitudes of the differences in impedances across the top and bottom boundaries of **A** and **B**. When fracture intensity and fracture openness increase locally, the difference between S2 and S1 velocities increases. S1 velocity changes little (usually not at all) when fracture intensity increases, but S2 velocity decreases and becomes closer to the magnitude of the S-wave velocity of its lower-impedance bounding unit. As a result, S2 reflectivity diminishes, but S1 reflectivity does not when fracture intensity increases. To define locations where relative fracture intensity increases, we thus searched the S1 and S2 volumes to find coordinates where S2 reflection amplitudes diminish but S1 amplitudes change little or not at all. Two image coordinates where this type of reflectivity behavior occurs are shown in Figure 37 (intervals SR1 and SR2). Common interpretation of these differences in S1 and S2 reflectivities is that a relative increase in fracture intensity and/or fracture openness occurs at locations SR1 and SR2. These principles of elastic

wavefield stratigraphy led us to create ratios of S1 seismic amplitude facies and S2 seismic amplitude facies to define areas of increased fracture intensity. Larger values of the ratio (S1 amplitude:S2 amplitude) appear to indicate higher fracture density.

3. The S1 time thicknesses across intervals **A** and **B** expand and contract in ways that differ from the expansion and contraction pattern of S2 **A** and **B** interval-time thicknesses. Some of these relative time-thickness changes are difficult to see by visual inspection of Figure 37, but numerical analyses of the isochron intervals between interpreted horizons reveal numerous examples of such behavior. Two locations where time thickness of a reflection wavelet expands more in S2 image space than it does in S1 image space are labeled T1 and T2. When the S2 interval time between horizons **aa** and **cc** (Fig. 37b) increases, two possible explanations are that (1) thickness of reservoir **A** has increased or (2) reservoir **A** has a constant thickness, but S2 velocity has lowered because of an increase in fracture intensity. Other arguments may be proposed in different geological settings, but at this prospect, these two explanations were the most plausible. Option 1 can be verified by measuring S1 interval time between horizons **aa** and **cc** (Fig. 37a). If the reservoir interval thickens, S1 interval time should increase. If S1 interval time changes little or not at all, then option 2 (increased fracture intensity) is accepted as the explanation for increase in S2 time thickness. The two image coordinates T1 and T2, where S2 time thickness increases more than does S1 time thickness, suggest that increased fracture intensity is expected at each of these locations. Elastic wavefield stratigraphy now introduces an additional set of seismic facies, interval values of S1 and S2 velocities, that can be utilized to evaluate fracture systems. Larger values of the ratio T2:T1, which is a ratio of S1 interval velocity:S2 interval velocity, appear to indicate higher fracture density.

In summary, multicomponent seismic data and elastic wavefield stratigraphy provide more geologic information about fractured-rock systems than do P-wave data and conventional seismic stratigraphy. Specifically, an elastic wavefield stratigraphy approach to prospect evaluation provides

1. fracture orientation by determining the polarization direction of the S1 mode (Fig. 36) and
2. qualitative estimates of fracture density by calculating ratios of S1 and S2 amplitudes and ratios of S1 and S2 interval-time thicknesses (Fig. 37).

Fracture orientation and fracture density are difficult (usually impossible) to interpret from P-wave seismic data alone. These advantages of multicomponent seismic data and elastic wavefield stratigraphy are emphasized in the rock-physics analyses that follow.

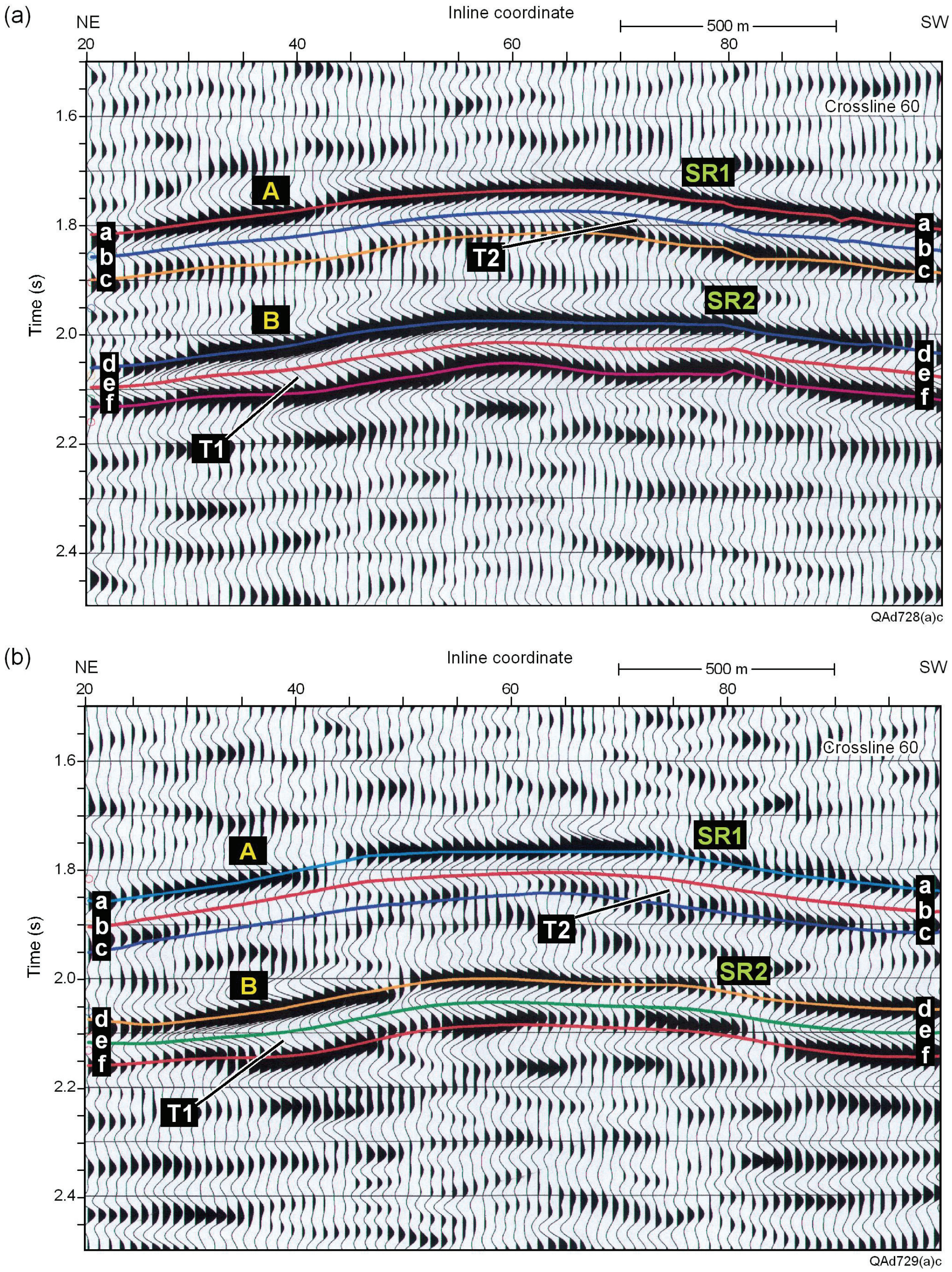

Figure 37. (a) Vertical slice from fast-S volume. (b) Equivalent vertical slice from companion slow-S volume. **A** and **B** are reflections from targeted fractured-carbonate reservoirs. Horizons **aa** through **ff** are used to measure fast-S and slow-S time thicknesses and amplitude attributes across intervals **A** and **B**. SR1 and SR2 define image coordinates where slow-S reflectivity diminishes but fast-S reflectivity does not. T1 and T2 define locations where a fractured interval shows an increase in time thickness in slow-S space that is not observed in fast-S space.

Rock Physics

The rock physics model that we used to analyze elastic wavefield propagation in a vertical-fracture medium is illustrated in Figure 38. Fracture planes 1 through 6 are part of a single set of vertical fractures that form a ***horizontal-transverse-isotropy (HTI)*** medium having a horizontal symmetry axis **AA** (with the shaded vertical plane passing through **AA** being a symmetry-axis plane) and a vertical isotropy plane **BB**. The top of this fracture system is horizontal interface **CCDD**. The layer above interface **CCDD** is not shown, but for modeling purposes, this caprock layer was assigned these properties: V_P = 4000 m/s, V_S = 2200 m/s, and ρ_b = 2.4 gm/cm^3.

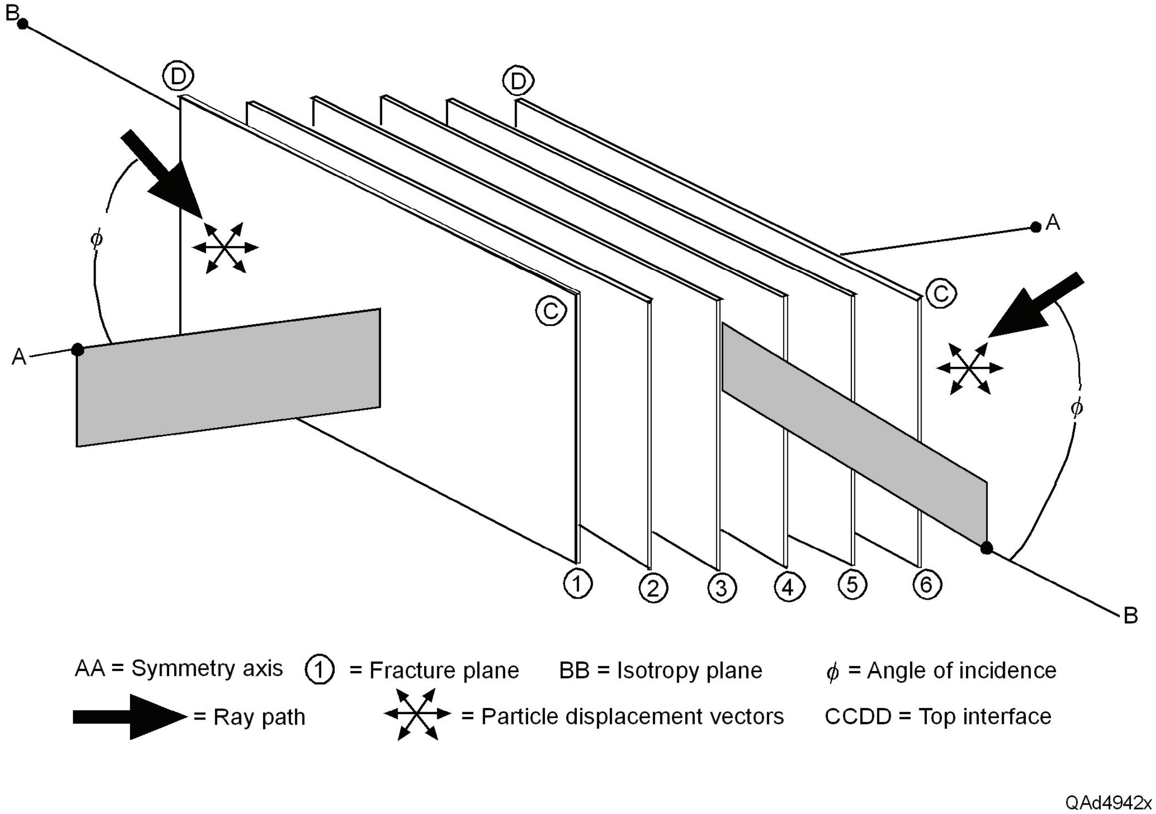

Figure 38. Model used to describe elastic wave propagation in an HTI medium.

For simplicity, downward-traveling elastic waves arrive at interface **CCDD** from only two azimuth directions: (1) in the direction of vertical symmetry-axis plane **AA** or (2) in the direction of vertical isotropy plane **BB**. Using the Hudson theory (1981), we assigned the fracture layer the following properties:

- Fast V_P = 5390 m/s, Slow V_P = 5385 m/s
- Fast V_S = 2970 m/s, Slow V_S = 2618 m/s
- ρ_b = 2.59 gm/cm^3, Fracture density = 0.1
- Aspect ratio of fractures = 0.0001.

These petrophysical properties, combined with the anisotropic reflectivity analyses of Ruger (2002), result in the reflectivity responses plotted in Figure 39. In the subscript notation used in this plot, A and B are the symmetry and isotropy directions used in Figure 38. These curves show three principles that support the azimuth-dependent P-P and P-SV data displayed in Figure 35:

1. P-P reflectivity does not change with azimuth (curves PP_A and PP_B are identical), and P-P data in the top display of Figure 35 show no amplitude variation with azimuth.
2. P-SV reflectivity does vary with the azimuth approach direction of the incident P wave relative to vertical fractures (curves PSV_A and PSV_B differ), and P-SV data in the lower display of Figure 35 change amplitude as azimuth changes.
3. P-SV reflectivity is less when the incident P wave is approaching normal to fractures (slow-S direction) than it is when the P wave approaches parallel to fractures (fast-S direction). This effect is well documented for fracture reflection B in Figure 35b.

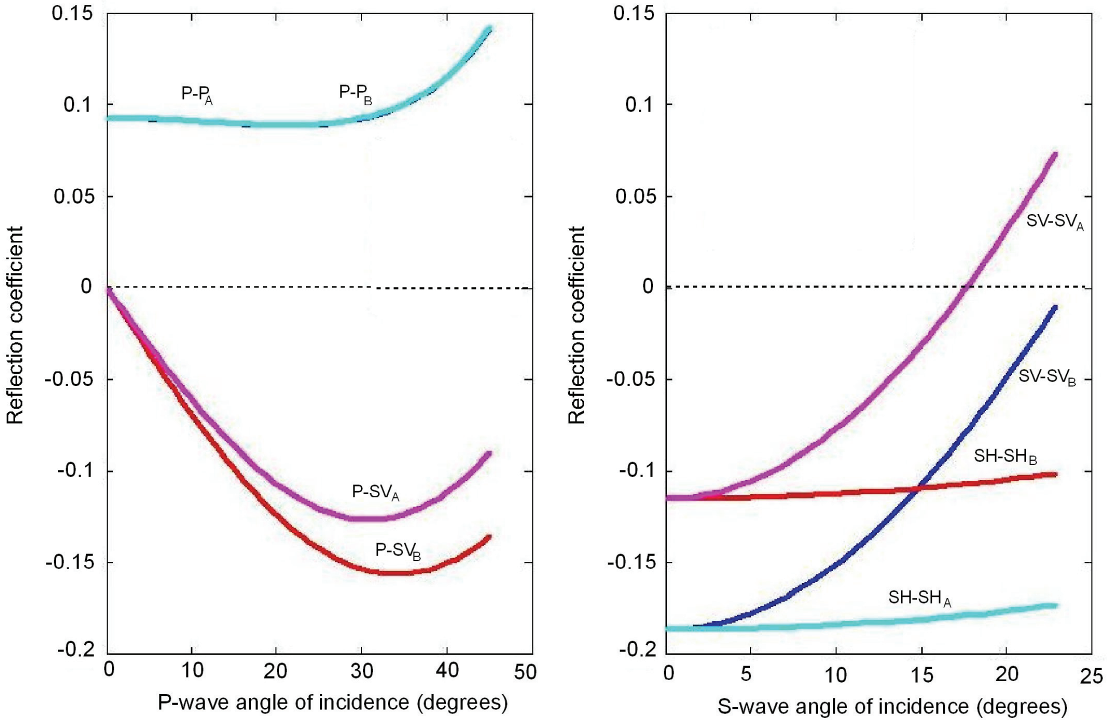

A,B = Axis of raypath direction

p = Component parallel to fractures
n = Component normal to fractures

QA4936x

Figure 39. P-P and P-SV reflectivities (left) and S-S reflectivities (right) for waves propagating in a brine-filled HTI medium as defined in Figure 38. Subscript A indicates the raypath is confined to symmetry plane AA. Subscript B indicates the raypath is confined to isotropy plane BB (Fig. 38).

The model results in Figure 39 assume that the fractures are filled with brine and that the fracture density is 0.1. Different reflectivities occur if the fracture-filling fluid is gas rather than brine and/or if fracture density varies. For completeness of the analysis, curves in Figure 40 illustrate the types of reflectivity variations that can be encountered when (1) fractures are isotropic and not aligned as in Figure 38, (2) fracture density varies, and (3) fractures are filled with brine or gas.

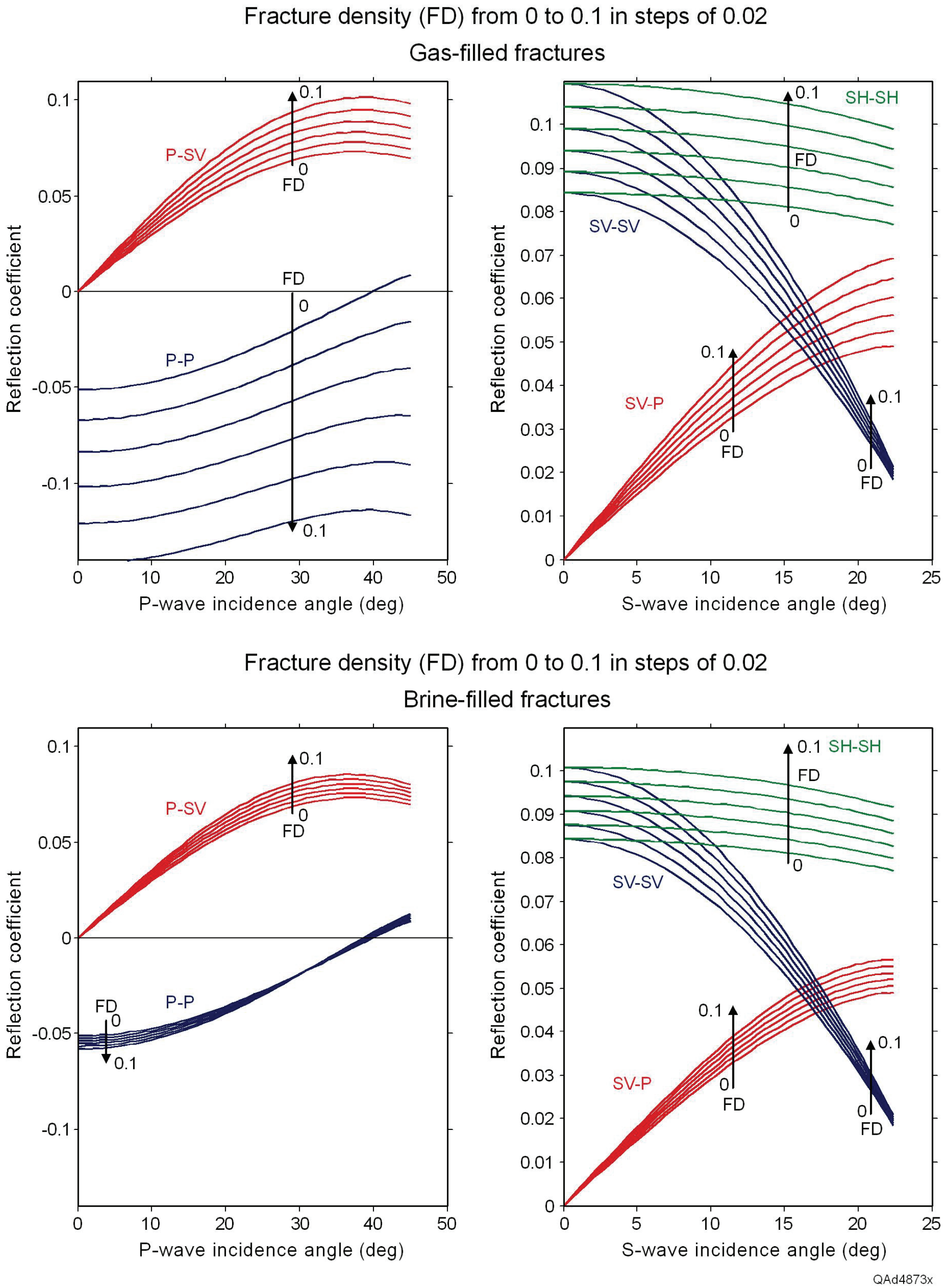

Figure 40. Effects of fracture density and fracture-filling fluid on reflectivity of each component of a seismic elastic wavefield from an isotropic-fractured layer. (Top) Reflectivities for gas-filled fractures. (Bottom) Reflectivities for brine-filled fractures. Fracture density FD is defined as FD = $N(Q^3/V)$, where V is a unit volume, Q is the effective radius of a fracture, and N is the number of fractures in volume V. Gas-filled and brine-filled fractures have the same P-SV, S-S, and SV-P reflectivities, but P-P reflectivity differs for the two fluids.

Deep-Water, Near-Seafloor Geology

P and S Sequences and Facies

There is increasing industry interest in applying multicomponent seismic technology in marine environments. Consequently, some of the elastic wavefield stratigraphy research in this project focused on interpretation of deep-water P-P and P-SV data acquired using 4-component ocean-bottom-cable (4-C OBC) technology. We illustrate here our P-P and P-SV processing of 4-C OBC data acquired in water depths of 800 to 900 m in the Gulf of Mexico (GOM) and our interpretation of P-P and P-SV seismic sequences and seismic facies observed in near-seafloor strata. The V_P/V_S velocity ratio in these strata is quite high, ranging from 5 at subseafloor depths of a few hundred meters to as much as 60 in the first 2 to 3 m of sediment. These high values of V_P/V_S are caused by anomalous low V_S velocities that cause dramatic differences in P-P and P-SV reflection responses. One objective of our research was to document the differences between P-P seismic sequences and facies and P-SV seismic sequences and facies observed in deep-water, near-seafloor environments associated with gas hydrate systems.

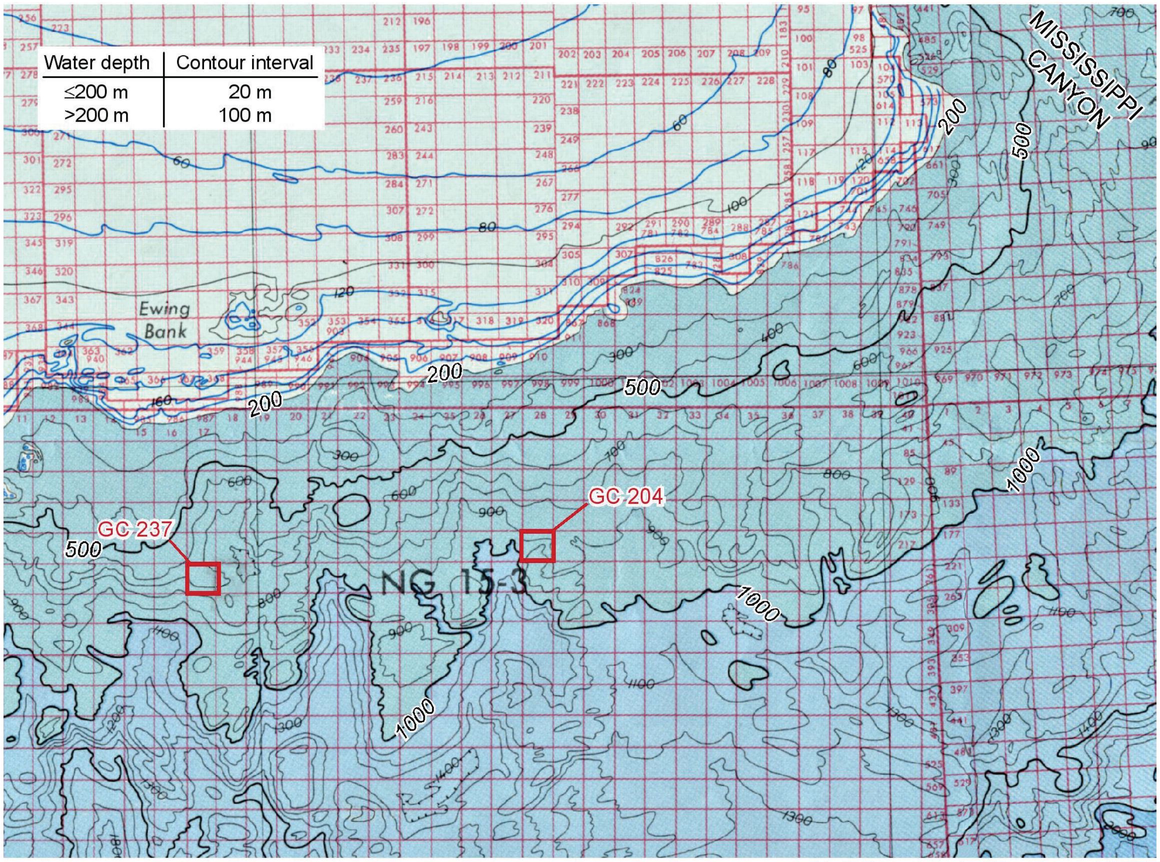

U. S. Department of Commerce (1986)

QAd3453x

Figure 41. Seafloor topography and water depth across Green Canyon Blocks 204 and 237.

We selected 4C OBC seismic profiles across two blocks of the Green Canyon area (Blocks GC 237 and GC 204), offshore Louisiana, where WesternGeco acquired a large 4C OBC seismic survey. Locations of these blocks are shown on a local seafloor topography map in Figure 41. We will first describe our analysis of 4-C OBC data across Block GC 237. In our processing of the P-SV data, we created images of only the radial component of the P-SV wavefield because the amount of seismic energy appearing on the transverse horizontal geophone over the shallow data window we studied was small. At deeper data windows, appreciable energy is often found on the transverse horizontal geophone.

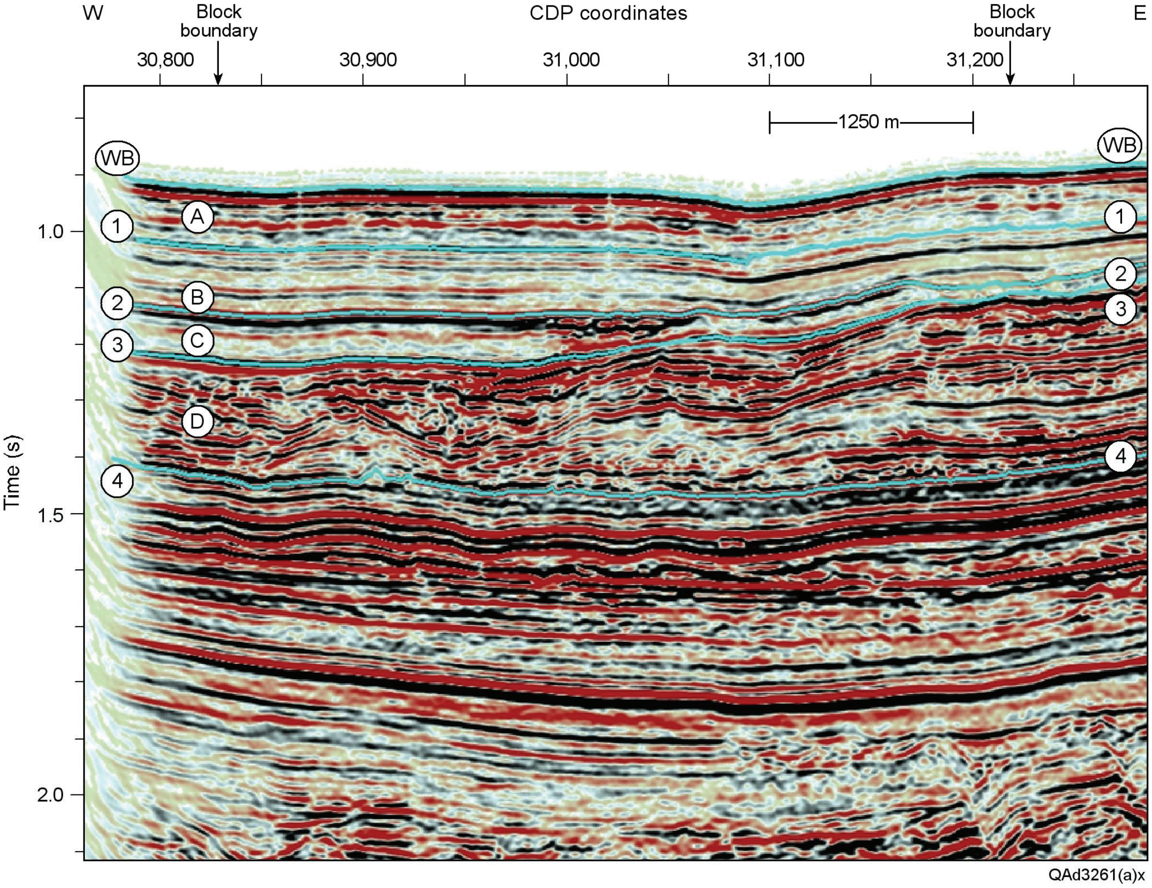

Figure 42. P-P profile along OBC Line 288. **WB** is the water bottom. Surfaces **1** through **4** are interpreted sequence boundaries. **A**, **B**, **C**, and **D** are interpreted sequences.

The P-P image along Line 288 of Block GC237 is displayed as Figure 42. Several interpreted horizons are shown that define the seismic sequences immediately below the seafloor. Horizon **WB** is the water bottom. Horizons **1** through **4** are successively deeper sequence boundaries. The seismic sequences defined by these boundaries are labeled **A**, **B**, **C**, and **D**.

The radial P-SV image along this same profile is shown in Figure 43. Labeled horizons are interpreted to be depth equivalent to horizons shown in the P-P image (Fig. 42). Horizons occur at different image times than do the P-P horizons because of the difference in V_P and V_S propagation velocities through the strata. Reflections from the zone near the water bottom are not imaged with these particular P-SV data because of the data muting technique that was used in data processing. In later figures, we use a different data-processing strategy that produces P-SV images starting essentially at the seafloor.

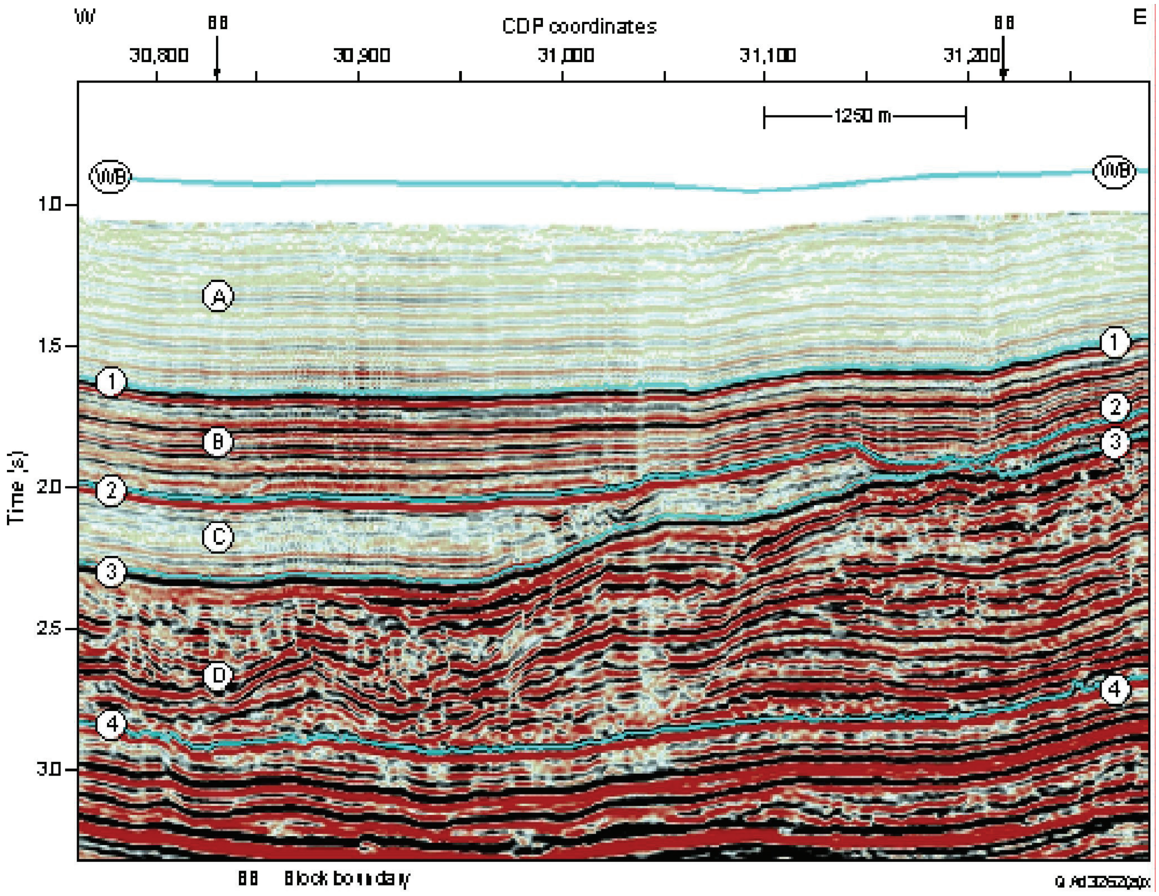

Figure 43. P-SV profile along OBC Line 288. **WB** is the water bottom. Surfaces **1** through **4** and sequences **A** through **D** are depth equivalent to the same features in the P-P image (Fig. 42).

Because the seafloor is not imaged in Figure 43, horizon **WB** from the P-P image is transferred onto the P-SV image. P-SV sequences **A**, **B**, **C**, **D** are interpreted to be depth equivalent to P-P sequences **A**, **B**, **C**, **D**.

One obvious difference between these P-P and P-SV images is that the P-SV data show a more detailed picture of the internal fabric of the shallowest strata. The difference between P-P and P-SV images is most pronounced for sequences **A** and **B**. The primary reason for the difference in vertical resolution is that the V_P/V_S velocity ratio is unusually high for these near-seafloor, deep-water sediments, as we have emphasized. Our measurements of V_P/V_S within sequence **A** ranged from 10 to 15 across Block GC 237, with a value of 12 being a reasonable average value for that part of Line 288 shown in Figures 42 and 43.

To see the effect of this velocity ratio on seismic resolution, consider the fundamental definition of wavelength λ, which is

(1) $\lambda = V/f$,

where f is frequency and V is velocity. For each frequency component of the downgoing illuminating P wavefield, a V_P/V_S velocity ratio of 12 means that the wavelength in the reflected SV wavefield is 12 times shorter than the corresponding wavelength in the reflected P wavefield. Shorter wavelengths result in better spatial resolution. Because all downgoing P-wave frequencies are in the backscattered SV wavefield for shallow penetration depths, P-SV sequence **A** has a spatial resolution that is approximately an order of magnitude better than the spatial resolution of P-P sequence **A**.

The V_P/V_S velocity ratio decreases to about 8 in sequence **B**, to about 6 in sequence **C**, and then to about 4 in sequence **D**. The contrast between P-P and P-SV resolution diminishes with increasing depth below the seafloor because

1. V_S increases more rapidly than does V_P and
2. higher frequency components appear to be more attenuated in backscattered P-SV wavefield than in backscattered P-P wavefield as raypaths lengthen.

Both of these factors cause the wavelengths in the P-SV data to increase, which reduces resolution of the P-SV data in deeper sequences.

There is a large difference between P-P and P-SV seismic amplitude facies, particularly for sequences **A** and **B**. There is almost no contrast between the P-P amplitude facies in sequence **A** and the P-P amplitude facies in sequence **B** (Fig. 42). In fact there is no obvious reason to introduce sequence boundary **1** into the P-P image if the data interpretation is restricted to only the P-P response. In contrast, there is a significant difference between the P-SV amplitude facies in sequence **A** and the P-SV amplitude facies in sequence **B** (Fig. 43). An interpreter is compelled to introduce a sequence boundary (horizon **1**) into the P-SV image to segregate P-SV facies **A** from P-SV facies **B**. Once this sequence boundary was defined in P-SV image space, we then interpreted its depth-equivalent horizon in P-P image space, even though a sequence boundary is not obvious between sequences **A** and **B** in the P-P image.

The major support for interpreting these strata using an elastic wavefield stratigraphy approach rather than a conventional P-P seismic stratigraphy approach is the contribution made to geologic understanding by the stark difference between the P-P and P-SV seismic facies. Once sequence boundary **1** is introduced into the P-P image, the geometrical configuration of P-P sequences **A**, **B**, **C**, **D** are similar to the geometrical configurations of P-SV sequences **A**, **B**, **C**, **D**. Either suite of sequences, P-P or P-SV, infers the same depositional architecture. In contrast, the P-SV amplitude facies in sequences **A** and **B** imply a lithofacies distribution that is significantly different from what is inferred by the P-P seismic facies within sequences **A** and **B**.

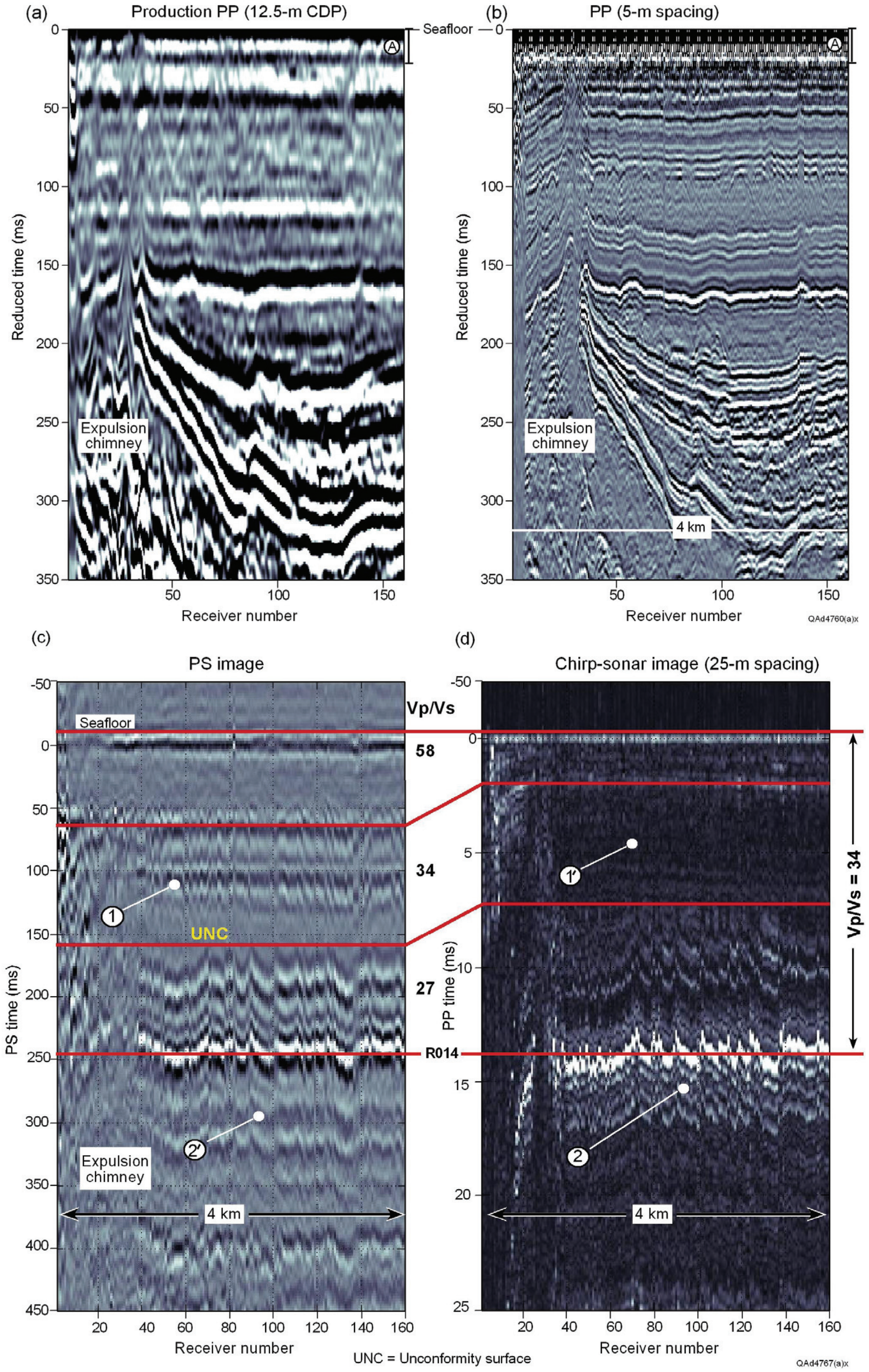

Figure 44. (a) Standard P-P production processing of deep-water 4C OBC seismic data. (b) Improved P-P resolution of near-seafloor geology and (c) P-SV image produced by specialized data-processing procedures (Backus and others, 2006). (d) High-resolution P-P image obtained with AUV chirp-sonar system. All images flattened to the seafloor. OBC P-SV data (c) provide resolution equivalent to 2-8 kHz chirp-sonar data (d) across upper 20 m of sediment. V_P/V_S velocity ratios labeled across selected depth intervals of c and d. **1** and **2** identify strata seen in one image space and not in its companion image space. **1′** and **2′** show where numbered features should appear in the companion image space. Images c and d span only the 25-ms interval **A** labeled at top of a and b.

A second data example from Block GC204 is illustrated as Figure 44. If deep-water strata are illuminated with conventional air gun sources towed at the sea surface, we can use special data-processing procedures to improve upon conventional P-P imaging, as illustrated in panels a and b (Backus and others, 2006). However, P-P resolution is still limited by the frequency spectrum of the air gun data, which have a frequency spectrum spanning from 10 to almost 120 Hz. An approach now used to acquire short-wavelength P-P data for studying near-seafloor geology in deep water is to use an ***Autonomous Underwater Vehicle (AUV)*** system. An AUV travels approximately 50 m above the seafloor and illuminates subseafloor strata with chirp-sonar pulses having a frequency bandwidth of 2 to 8 kHz. This increase in signal frequency shortens P-P wavelengths by a factor of almost 100, compared with the wavelengths of a conventional air-gun signal. The result is an illuminating wavefield having wavelengths that are only a fraction of a meter long when near-seafloor velocity V_P is 1,500 to 1,600 m/s, a common range of V_P for deep-water, near-seafloor sediments across the GOM. An example of an AUV chirp-sonar image acquired along the same profile as the OBC data is shown in Figure 44d.

The illuminating wavefield that created the P-SV data shown in panel c was a 10- to120-Hz P wavefield produced by a conventional air-gun array positioned at the sea surface, the same source that produced the P-P images in panels a and b. Because V_S in the shallowest near-seafloor sediment along this OBC profile is less than 100 m/s, the P-SV data have wavelengths less than 1 m in length, just as do the high-frequency AUV chirp-sonar data in panel d, even though the P-SV data are low frequency.

In Figure 44, a reflection event generated 1.5 m below the seafloor appears at 2 ms on the P-P chirp-sonar section (panel d) and at 60 ms on the P-SV image (panel c), suggesting a V_P/V_S ratio of approximately 60. The chirp-sonar reflection at 2 ms is faint and somewhat hidden beneath the first horizon drawn across this particular chirp-sonar image. Reflections from an interface 10 m below the seafloor appear at 14 ms on the P-P chirp-sonar and at 250 ms on the P-SV image. The unconformity ***UNC*** at about 160 ms on the P-SV image ties to an image coordinate at 7.5 ms on the P-P chirp-sonar data. Unfortunately these high-resolution P-SV images cannot be extended to great subseafloor depths. P-SV wavelengths increase, and P-SV resolution thus decreases with increasing depth. At this location, the V_P/V_S ratio decreases sharply below 20 m, to about 8, and reduces to 4 and less below 150 m, where P-SV and P-P resolutions are more comparable. However, for deep-water GOM strata close to the seafloor, spatial resolution of low-frequency P-SV data is most impressive.

To fully appreciate the resolution of P-SV data (panel a), note that this P-SV image is depth equivalent to the 25-ms P-P image in panel d, and then compare both panels c and d with the 25-ms interval labeled **A** at the top of the OBC P-P images (panels a and b). Different P-P and P-SV reflection responses are noted in panels c and d by the labels **1**, **1′**, **2**, and **2′**. It is difficult to decide whether these particular P-P and P-SV modes are detecting different sequences and facies at these image coordinates, or whether these variations in reflectivity are caused by the P-P imaging wavelet being distinctly different from the P-SV imaging wavelet. Different imaging wavelets will create different seismic sequences and facies, as documented by Figures 3 through 5. Without question, the P-P wavelet in panel d is not the same wavelet that created the P-SV image in panel c. In panel c, the P-SV image is constructed with a short, compact, zero-phase wavelet similar to the wavelets created in all marine seismic data imaging. In contrast, the P-P chirp-sonar data in panel d are not constructed from a wiggle-trace-type wavelet but from an energy-envelope function, which makes the data have only positive values and to have no positive/negative wiggle-trace-like behavior. Until we have a better understanding of how a P-P chirp-sonar energy envelope should be numerically related to a P-SV wiggle-trace wavelet, we do not wish to claim that either features **1** and **1′** or features **2** and **2′** in panels c and d define different sequences or facies.

Rock Physics

In an analysis of deep-water gas hydrate systems, Sava and Hardage (2006) considered four rock-physics models for the deep-water, unconsolidated sediments that are imaged by the seismic data shown in Figures 42 through 44. These sediment-hydrate-fluid models are illustrated in Figure 45. Model **A** assumes that gas hydrates are uniformly disseminated throughout the whole volume of sediment and act as a part of the load-bearing frame of the host sediments. Model **B** assumes that gas hydrates are also disseminated throughout the whole volume of sediment, but that they fill only the porous space and do not affect the dry mineral frame of their host sediments. Model **C** assumes an anisotropic, thin-layered medium having layers of pure gas hydrate intercalated with layers of unconsolidated sediments saturated with brine. Model **D** is also an anisotropic, thin-layered medium. However, in this model, gas hydrates are disseminated in thin layers of sediments, occupying 99 percent of the porous space of these layers, and act as part of the load-bearing frame. These hydrate-bearing beds are intercalated with layers of unconsolidated sediments saturated with brine. The key input parameter in all of these models is gas-hydrate concentration c_{gh}.

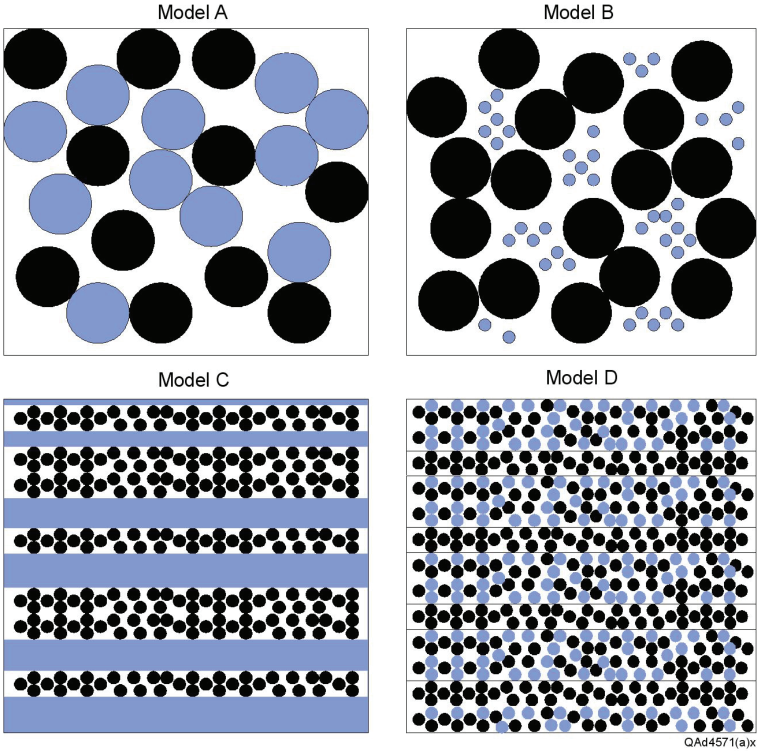

Figure 45. Possible gas hydrate models. (Model A): load-bearing gas hydrates. (Model B): pore-filling gas hydrates. (Model C): thin layers of pure gas hydrate intercalated with unconsolidated sediment. (Model D): thin layers of disseminated load-bearing hydrate intercalated with unconsolidated sediment. Hydrates are shown in blue and sediment is black.

Figure 46 presents modeling results for P-wave velocity (V_P) and S-wave velocity (V_S) as a function of gas hydrate concentration (c_{gh}) for these four rock-physics models. In each model, the host sediment is assumed to be clay, the porosity of the host sediment is assumed to be 0.37, and the effective pressure is 0.01 MPa. If any of these medium properties (grain type, porosity, or effective pressure) is changed, these V_P and V_S curves shift in this display coordinate space. For the two anisotropic layered models (**C** and **D**), two curves are shown: one corresponding to waves polarized parallel to the layering (solid line) and one describing waves polarized orthogonal to the layers (dotted line). These results show that relations between seismic velocities and gas hydrate concentration depend not only on the environmental constraints of the host medium (grain, type, porosity, effective pressure), but, more importantly, they depend on the geometrical details of how gas hydrates are distributed in their host sediments.

In each rock-physics model, an increase in gas hydrate concentration increases P-wave velocity in the sediments. The smallest increase in P-wave velocity occurs for the thin-bedded model having layers of pure gas hydrates (Model **C**), whereas the largest increase in P-wave velocity is obtained for models having disseminated, load-bearing gas hydrates (Models **A** and **D**). These rock-physics models show that any value of V_P measured across a hydrate-bearing interval can be related to hydrate concentration only if a specific hydrate-to-sediment morphology is assigned to that interval.

S-wave velocity does not vary with gas hydrate concentration for the model in which hydrates fill the porous space of the sediments (Model **B**). However, a large, almost linear, increase in S-wave velocity occurs when S-waves are polarized parallel to the layers of a medium having thin beds of disseminated, load-bearing gas hydrates (Model **D**, solid line). The S-wave anisotropy in this model is large, as shown by the difference between S-wave velocities polarized parallel (Model **D**, solid line) and orthogonal (Model **D**, dotted line) to layers of disseminated, load-bearing gas hydrates. S-wave anisotropy for a system of thin layers of pure gas hydrates (Model **C**) is also large. These calculations again emphasize that the correct geometrical distribution of hydrate within the host sediment must be known before a measured value of V_S can be interpreted in terms of hydrate concentration.

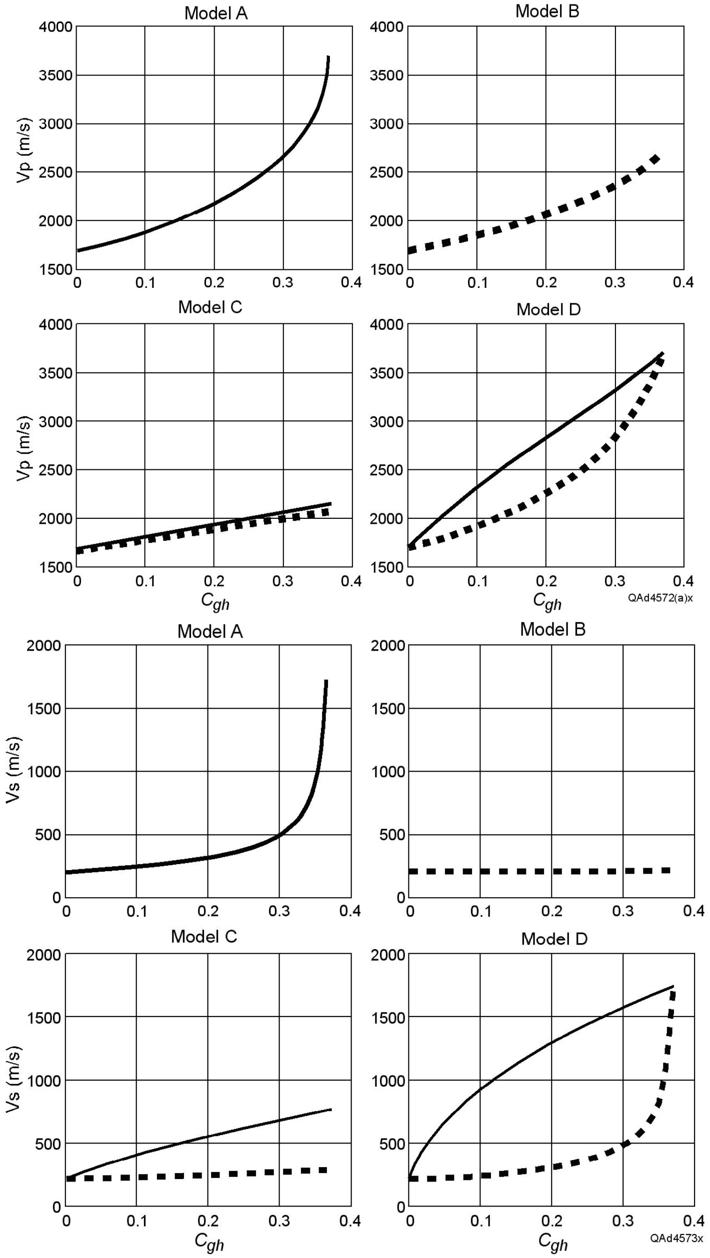

Figure 46. P-wave and S-wave velocities as a function of the volumetric fraction of hydrate in the sediment (C_{gh}) for each of the four models defined in Figure 45.

To illustrate why P-P and P-SV images of deep-water, near-seafloor geology display different seismic sequences and seismic facies, we calculated representative P-P and P-SV reflectivities for an interface between unconsolidated clay having a hydrate concentration of zero and unconsolidated sand having a variable hydrate concentration. Typical response curves are shown in Figure 47 for hydrate morphologies defined as Model A and Model B in Figure 45. P-P reflectivity is approximately the same for load-bearing and pore-filling hydrate morphologies, but P-SV reflectivity is not. These reflectivity behaviors suggest that it will be difficult to determine whether one part of a deep-water hydrate system is a load-bearing morphology and another part is a pore-filling morphology if only P-P seismic data are available (conventional seismic stratigraphy). They also suggest, however, that such a morphology change should be detectable if both P-P and P-SV data are available (elastic wavefield stratigraphy).

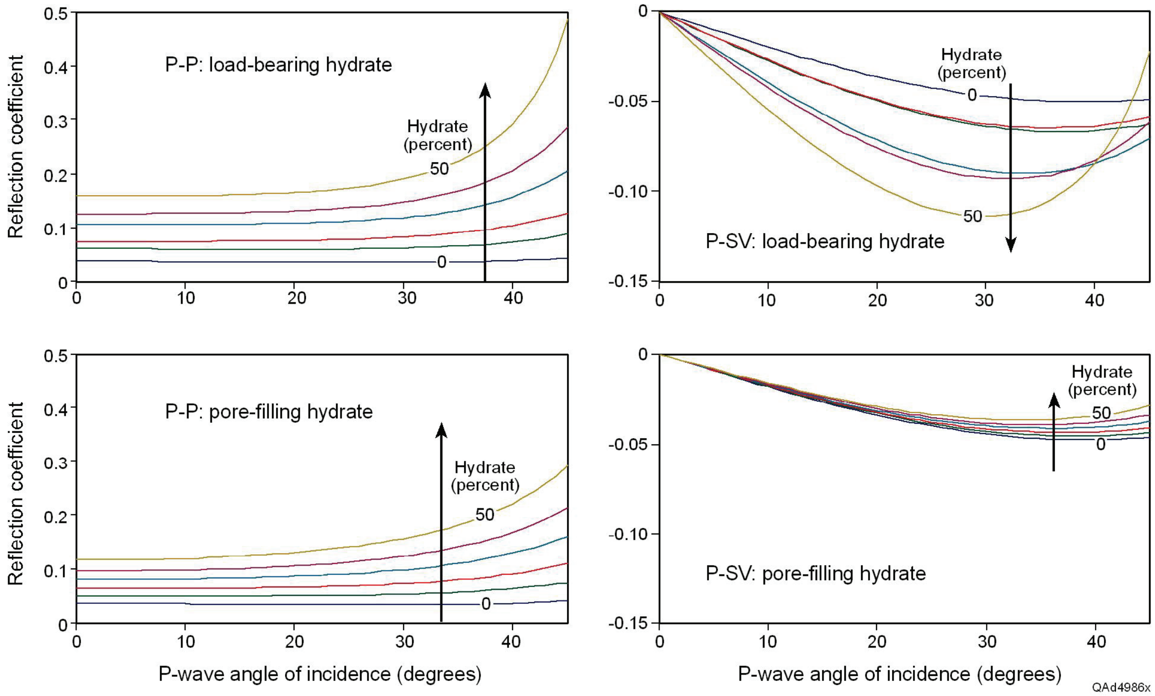

Figure 47. P-P and P-SV reflectivities for gas hydrates. (Top) Load-bearing hydrate. (Bottom) Pore-filling hydrate.

Deep Geology: Northern Shelf of the Gulf of Mexico

P and S Sequences and Facies

Examples of P-P and P-SV images of deep geologic targets across the northern shelf of the GOM are illustrated here as side-by-side displays, with P-SV data *warped* to P-P image-time coordinates. This ***time warping*** is a first-order depth registration of P-P and P-SV images implemented by using a single, averaged, V_P/V_S velocity ratio function to adjust P-SV image time to P-P image time over a large study area. Although not 100-percent precise, this first-order adjustment of P-SV image time to P-P image time is sufficiently accurate to allow equivalent geology to be identified in side-by-side comparisons of P-P and P-SV images.

The first example, displayed as Figure 48, extends to a depth of approximately 5.5 km (~18,000 ft). The dipping strata labeled **A** in each image space are interpreted to be depth-equivalent geology. In this instance, the regional time-warping function positions feature **A** about 200 ms earlier in time-warped P-SV image space than where it is positioned in P-P image space. Even though the time warping is not precise, depth-equivalent P-P and P-SV structure and stratigraphy can be identified between the two image spaces. Interval **1** indicates sequences and facies that are imaged by the P-P mode and not as well imaged by the P-SV mode. Events **2** through **5** represent sequences and facies that are imaged by the P-SV mode and poorly imaged by the P-P mode.

This image comparison shows that in this local area, P-SV data image deep targets as well as do P-P data, and P-P and P-SV data have equivalent resolution. This latter observation is important because equivalent image resolution indicates that the basic P-P and P-SV wavelets are reacting to bed thickness, bed spacing, and target overlap in the same way. The modeling in Figures 3 through 5 suggest that any differences in P-P and P-SV images will then be caused by rock and fluid properties that affect P-P and P-SV reflectivities, not by the fact that wavelets with different dominant wavelengths react to bed thickness and bed spacing in different ways.

The different sequences and facies seen in these particular P-P and P-SV image spaces are thus caused by geology and are not wavelet-induced artifacts. To emphasize the differences between P-P and P-SV sequences and facies, positions of the numbered P-SV sequences and facies are transposed to P-P image space and labeled with corresponding primed (yellow circle) numbers, which will aid in visually comparing P-P and P-SV responses. Similarly, positions of numbered P-P sequences and facies are transposed to P-SV space and indicated by primed numbers (yellow circles). Comparing the seismic facies at primed and unprimed number locations shows that each elastic wave mode provides different, but equally valid, sequence and facies information, which is a fundamental principle of elastic wavefield stratigraphy.

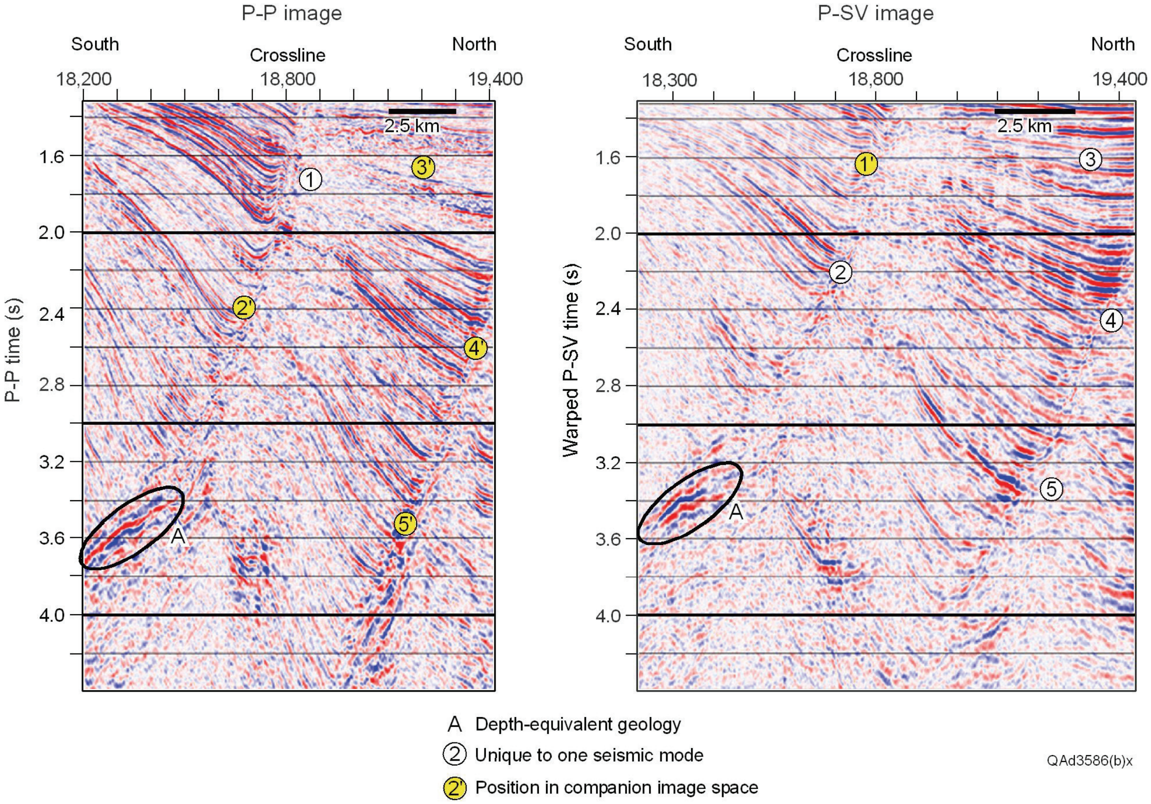

Figure 48. Example 1 of depth-equivalent P-P and P-SV images of deep GOM geology. **A** defines depth-equivalent geology. Numbers **1**, **2**, . . . indicate a sequence or a facies in one image space that is not seen in the companion image space. Prime numbers **1′**, **2′**, . . . show where numbered sequence or facies should appear in the companion image space.

Example 2 in Figure 49 again images GOM geology to a depth of about 5.5 km (~18,000 ft). Reflection package **A** labeled on each image is interpreted to be depth-equivalent geology. In this instance, the regional time-warping function is locally correct, and reflection package **A** is at the same image-time coordinates in both elastic-mode image spaces. Event **1** in P-P image space is caused by a lateral variation in pore fluid and is absent in P-SV image space, as it should be. Stratal packages **2** through **5** are examples of P-SV data imaging deep sequences and facies different from, and better than, P-P data do. Again, sequences and facies seen in one image space are transposed to its companion image space using primed numbers (yellow circles) to show where the features should be observed. Both images are correct; each elastic wave mode simply emphasizes unique suites of sequences and facies across some stratigraphic intervals that differ from those emphasized by its companion wave mode. If an interpreter relied totally on conventional seismic stratigraphy, only P-P sequences and facies could be utilized. In elastic wavefield stratigraphy, all sequences and facies labeled in the figure can be used in an interpretation. In this instance, P-SV sequences **2** through **5** (elastic wavefield stratigraphy) suggest a cyclic deposition that is more difficult to see in P-P image space (conventional seismic stratigraphy).

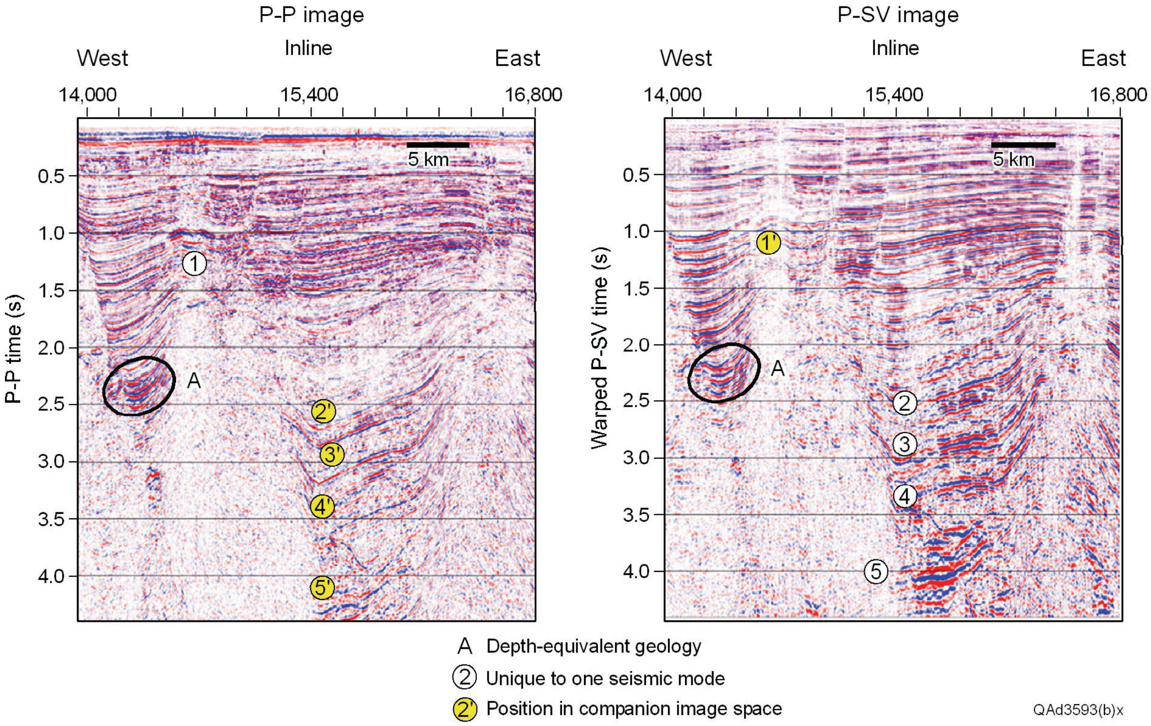

Figure 49. Example 2 of depth-equivalent P-P and P-SV images of deep GOM geology. **A** defines depth-equivalent geology. Numbers **1**, **2**, . . . indicate a sequence or a facies in one image space that is not seen in the companion image space. Prime numbers **1′**, **2′**, . . . show where numbered sequence or facies should appear in the companion image space.

Example 3 (Fig. 50) is a deeper data window that extends to a depth of about 6.3 km (~21,000 ft). The small anticlinelike feature defined by reflection package **A** in each image space is interpreted to be depth-equivalent geology. This data example is important because it shows a difference in P-P and P-SV images that is not related to geology or to differences in the dominant wavelength of illuminating wavelets, but is an artifact of data processing.

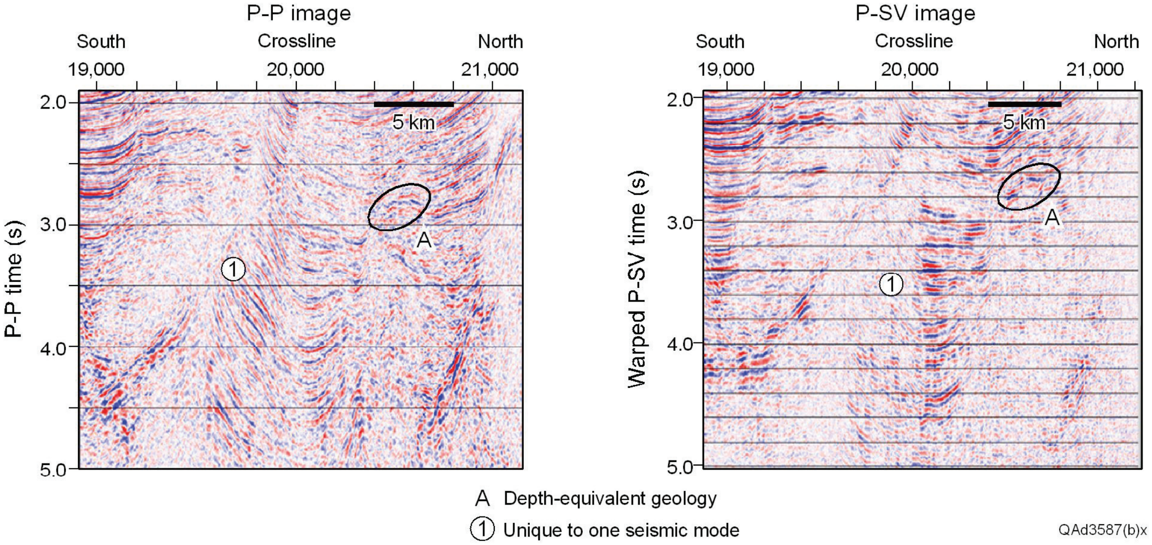

Figure 50. Example 3 of depth-equivalent P-P and P-SV images of deep GOM geology. **A** defines depth-equivalent geology. Numbers **1**, **2**, . . . indicate a sequence or a facies in one image space that is not seen in the companion image space.

The time-warping function places event **A** in P-SV image space about 200 ms earlier than where it is in P-P image space. The interval labeled **1** demonstrates an important aspect of P-P and P-SV wave physics for steep-dip imaging. Positive-offset P-SV data often provide an image of steep-dip strata that differs from the image provided by negative-offset P-SV data. In the processing of P-SV data, positive-offset data and negative-offset data are processed separately and imaged separately. Near the end of the P-SV data-processing sequence, positive-offset and negative-offset P-SV images are summed to make a total-offset P-SV image. It is not uncommon for one of these half-offset P-SV data volumes, either the positive-offset or the negative-offset data, to image some steep-dip strata better than the other half-offset image does. Neither is it uncommon for this particular half-offset image to show the steep-dip target better than the total-offset image does. All P-SV images used in this discussion are total-offset images. Reflection interval **1** in Figure 50 is an example in which a total-offset P-SV image does not depict steep dips in the same way as do P-P data. For a more acceptable depiction of structural dip to be inserted into P-SV image space at position **1**, the solution is sometimes as simple as inspecting the positive-offset P-SV image and the negative-offset P-SV image and selecting the half-offset image that optimizes the P-SV imaging of the steep-dip strata. This example may cause some interpreters to assume that CMP-based P-P data provide a more reliable image of dipping strata than do CCP-based P-SV data. However, other image comparisons can be documented that demonstrate situations where P-SV data show dipping strata better than P-P data do. The key point is that the principal difference between P-P interval **1** and P-SV interval **1** in this example is caused by a data-processing artifact that can complicate the use of elastic wavefield stratigraphy if the imaging principles of P-SV data are not considered during data interpretation.

Example 4 is shown in Figure 51. The base of this data window is about 5.5 km (~18,000 ft). Reflection packages **A** and **B** are interpreted to be depth-equivalent geology. Here time warping places **A** and **B** in P-SV time-warp space within 100 ms of their positions in P-P image space. Interval **1** indicates sequence geometry that is better seen by the P-P data than by the P-SV data. Reflection sequences **2** and **3** are important examples because they document a situation in which P-SV data image deep geology better than P-P data do, as shown by the yellow, primed numbers **2′** and **3′** in P-P image space and their equivalent geologic features **2** and **3** in P-SV image space. Rock-physics theory that explains why P-P and P-SV seismic modes exhibit different reflectivities in these types of siliciclastic rocks is explained in Figures 53 and 54.

Example 5 is a data window (Fig. 52) that extends to almost 7.5 km (~25,000 ft). Structural features **A** and **B** are interpreted to be depth equivalent. The time-warping process positions **A** and **B** in time-warped P-SV space to within 100 ms of their positions in P-P image space. A narrow, vertical salt structure blanks out both P-P and P-SV images approximately midway between CDP coordinates 19,600 and 21,000. Features **1** through **4** on the P-SV image indicate a cyclic depositional process that is not obvious in the P-P image (prime numbers **1′** through **4′**). Feature **5** is an example of P-SV data showing strata that are not present in the P-P data (position **5′**). Feature **6** is an example of the P-P mode providing a better image of high-dip strata than does the P-SV mode (event **6′**). These distinctive P-P and P-SV reflectivity behaviors are described by the following rock-physics theory.

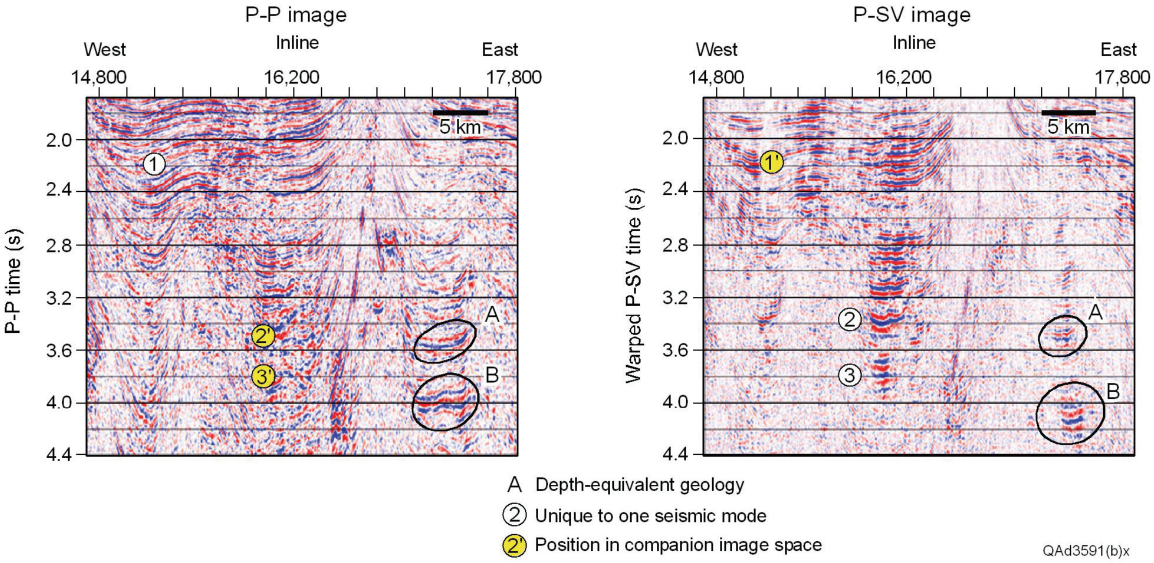

Figure 51. Example 4 of depth-equivalent P-P and P-SV images of deep GOM geology. **A** and **B** define depth-equivalent geology. Numbers **1**, **2**, . . . indicate a sequence or a facies in one image space that is not seen in the companion image space. Prime numbers **1′**, **2′**, . . . show where numbered sequence or facies should appear in the companion image space.

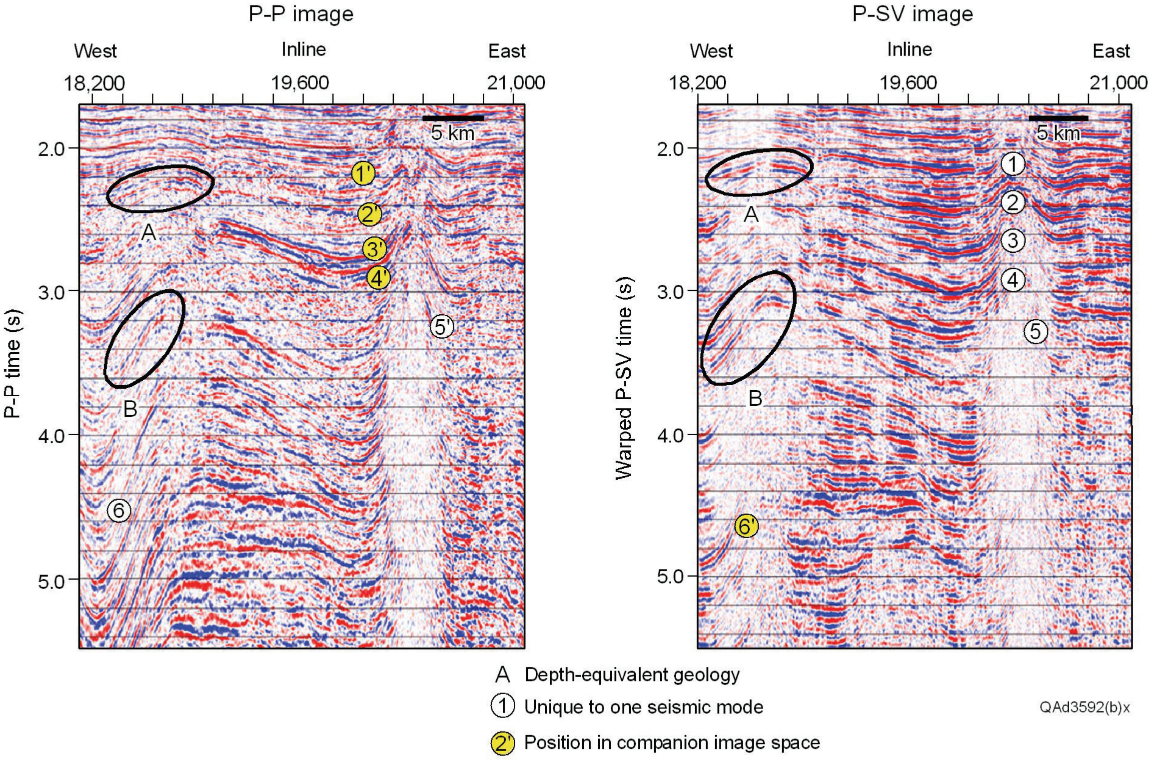

Figure 52. Example 5 of depth-equivalent P-P and P-SV images of deep GOM geology. **A** and **B** define depth-equivalent geology. Numbers **1**, **2**, . . . indicate a sequence or a facies in one image space that is not seen in the companion image space. Prime numbers **1′**, **2′**, . . . show where numbered sequence or facies should appear in the companion image space.

Rock Physics

Work by Han and others (1986) provides a rock-physics theory that is helpful in understanding P-P and P-SV reflection phenomena that occur in the clay-dominated lithofacies that are imaged in Figures 48 through 52. Han did a detailed laboratory analysis of 70 samples of consolidated rocks obtained from deep GOM cores. His core measurements established the following relationships between seismic velocities (V_P and V_S), porosity, and clay content:

(2) $V_P = 5.59 – 6.93\Phi – 2.18c$, and

(3) $V_S = 3.52 – 4.91\Phi – 1.89c$.

In these equations, V_P is P-wave velocity (in km/s), V_S is S-wave velocity (in km/s), Φ is porosity, and c is clay content ($0<c<1$). Constants in the equations are appropriate for rocks subjected to an effective pressure of 40 MPa or more, which would be pressure regimes of targets such as are shown in Figures 48 through 52. To calculate example reflectivities across super-deep data windows, we set Φ equal to 4 and 10 percent. Coupling these velocity equations with the density equation

$$(4)\quad \rho = [c\rho_{cl} + (1 - c)\rho_Q](1 - \Phi) + \rho_{fl}\Phi,$$

where ρ_{cl} is the density of clay, ρ_Q is the density of quartz, and ρ_{fl} is the density of the pore fluid, allows P-P and P-SV reflectivities at deep interfaces to be analyzed for targets having variable clay content.

These rock-physics equations are important because (a) they are based on real laboratory measurements made on real rocks and are not synthetic models, (b) rock samples come from geology imaged by the seismic data in Figures 48 through 52, and (c) rocks that were analyzed had a wide range of clay content. To illustrate the value of this rock-physics theory, we used a simple, two-layer Earth model (Fig. 53) to represent deep-target conditions across the northern shelf of the GOM.

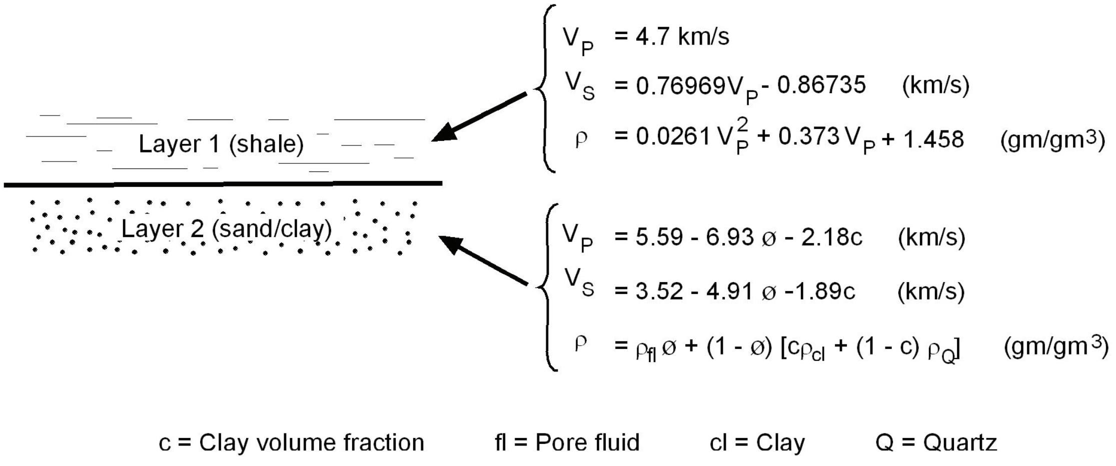

QAd4941x

Figure 53. Earth model used to demonstrate effect of clay content on P-P and P-SV reflectivities. Equations used to specify properties of Layer 1 (shale) come from Castagna and others (1993). Those used to specify properties of Layer 2 are from Han and others (1986).

We kept properties of the upper layer of this model constant, using values defined by equations in the figure, whereas clay content and pore fluid were varied in the lower layer. Resulting reflectivities from the two-layer interface, assuming a porosity of 4 percent for a super-deep sandstone reservoir, are displayed in Figure 54 for all elastic wave modes, including P-P, P-SV, SH-SH, SV-SV, and SV-P.

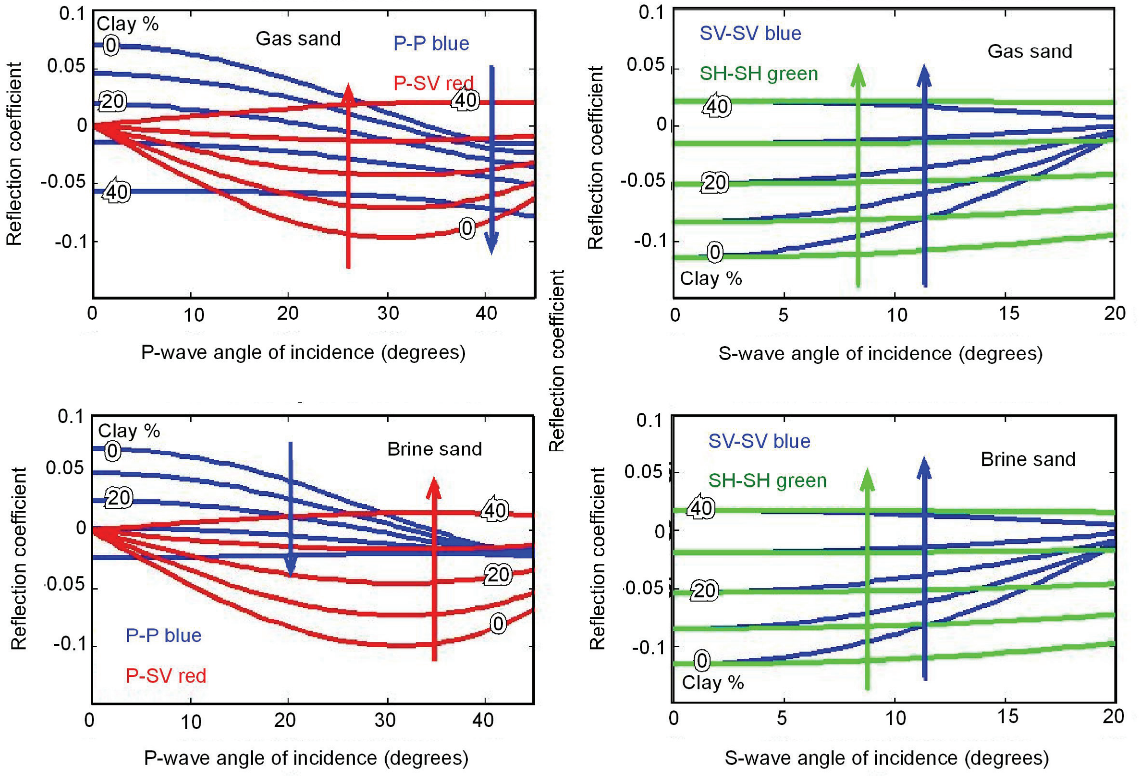

QAd4934x

Figure 54. P-P and P-SV AVA behaviors for varying clay content in a target layer. Layer 2 is assumed to be a super-deep unit with a porosity of only 4 percent. (Top) Pore fluid is 100 percent gas. (Bottom) Pore fluid is 100 percent brine.

Only P-P and P-SV reflectivities shown in the two panels on the left are needed to explain distinctions between P-P and P-SV images exhibited in Figures 48 to 52. These reflectivity curves provide an important message concerning P-P and P-SV images of siliciclastic rocks having variable clay content:

- For certain clay-content concentrations (c) within a gas-bearing layer (upper-left panel), the target layer is practically invisible to the P-P seismic mode but generates a strong P-SV reflection. For example, when c = 20 percent, P-P reflectivity is small and changes algebraic sign near an incidence angle of 20º. These two reflectivity characteristics are classic examples of a reflection event that is minor, and probably invisible, in a final-processed P-P image. In contrast, P-SV reflectivity for c = 20 percent is reasonably robust and has a constant algebraic sign at all incidence angles. This P-SV reflectivity behavior should create a significant P-SV reflection event.
- At other clay-content concentrations within a brine-saturated interval (lower-left panel), the target layer is a poor P-SV reflector but a robust P-P reflector. For example, when c = 40 percent, P-P reflectivity is 2 to 3 percent across the total angle range, but P-SV reflectivity does not reach a 2 percent value until the incidence angle is 20º.

Variations of clay content in sandstone lithofacies that have any amount of gas saturation can thus explain why certain intervals in depth-registered P-P and P-SV data show significant differences between P-P and P-SV reflection character. Data displayed in Figures 48 through 52 are examples of such reflectivity behaviors.

Curves in Figure 54 also suggest a strategy for segregating low-clay, brine-sandstone targets from low-clay, gas-sandstone targets. For a gas sandstone (upper left panel),

- P-SV reflectivity is relatively large when clay content is low (P-SV curves for c = 10 and 20 percent), but
- P-P reflectivity is smaller and undergoes a phase change between incidence angles of 20º and 25º for these same clay-content conditions (P-P curves for c = 10 and 20 percent).

For a brine sandstone (lower left panel),

- P-SV reflectivity is the same magnitude as it is for a gas sandstone of low clay content (P-SV curves for c = 10 and 20 percent), but
- P-P reflectivity is larger than it is for a gas sandstone and does not undergo a phase change until the incidence angle exceeds 30º (P-P curves c = 10 and 20 percent).

This rock-physics theory provides one explanation for the differences in deep-target P-P and P-SV reflectivities that were observed in our analysis of long-offset 4C OBC data (Figs. 48 through 52) and also establishes a logic that will help in identifying favorable and unfavorable reservoir facies for companies that elect to use elastic wavefield stratigraphy to evaluate deep gas targets.

Class 2 Reservoirs

Gas reservoirs across the GOM have been designated as Class 1, 2, 3, or 4 depending on their P-P amplitude-versus-angle (AVA) response (Rutherford and Williams, 1989; Castagna and others, 1998; Roden and others, 2005). The P-P AVA behaviors on which this classification scheme is based are shown as generalized curves in Figure 55. Although this reservoir terminology originated in the GOM and was initially applied only to sandstone reservoirs (Rutherford and Williams, 1989), the nomenclature is now used across basins worldwide and applied to reservoir lithofacies other than sandstones.

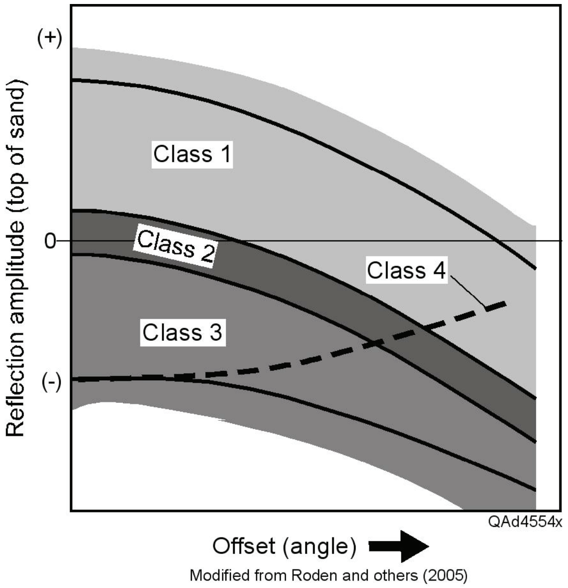

Figure 55. Domains of P-P AVA responses for Class 1, 2, 3, and 4 reservoirs. Typical P-P reflectivity curves are drawn for each P-wave AVA reservoir class.

Inspection of Figure 55 shows that a Class 1 reservoir exhibits a strong, positive P-P reflection response at normal incidence, and that response then decreases as the angle of incidence increases. A Class 2 reservoir has a small P-P response (either positive [Class 2A] or negative [Class 2B] polarity) at normal incidence, and its P-P response becomes more negative as the angle of incidence increases. A Class 3 reservoir has a strong, negative P-P response at normal incidence that becomes more negative as the angle of incidence increases. A Class 4 reservoir has a strong, negative response at normal incidence, just as does a Class 3 reservoir, but its P-P response decreases (becomes less negative) with increasing angle of incidence.

P and S Sequences and Facies

Only Class 2 reservoirs are considered in this discussion because Class 2 reservoirs are often faint, low-amplitude P-P events and sometimes are almost invisible in P-P data. One Class 2 reservoir that has been widely publicized is the Alba reservoir in the UK sector of the North Sea. P-P and P-SV seismic images across this particular reservoir have become classic data examples among the geoscience community and are used in this discussion rather than utilizing a Class 2 reservoir example from the multicomponent data available for our study. P-P and P-SV profiles across Alba are displayed as Figure 56 and show that the Alba target produces a minor response in P-P image space but creates a bold reflection package in P-SV image space (Duranti and others, 2000). This example illustrates that Class 2 reservoir interpretation can be difficult in a conventional seismic stratigraphy study that uses only P-P seismic data but can be on a much sounder foundation when both P-wave and S-wave data are available and elastic wavefield stratigraphy is utilized. By using P-SV images of

Alba (elastic wavefield stratigraphy), Hanson and others (2003) were able to develop a reservoir geometry that agreed with drilling results much better than did the models suggested by P-P data (conventional seismic stratigraphy).

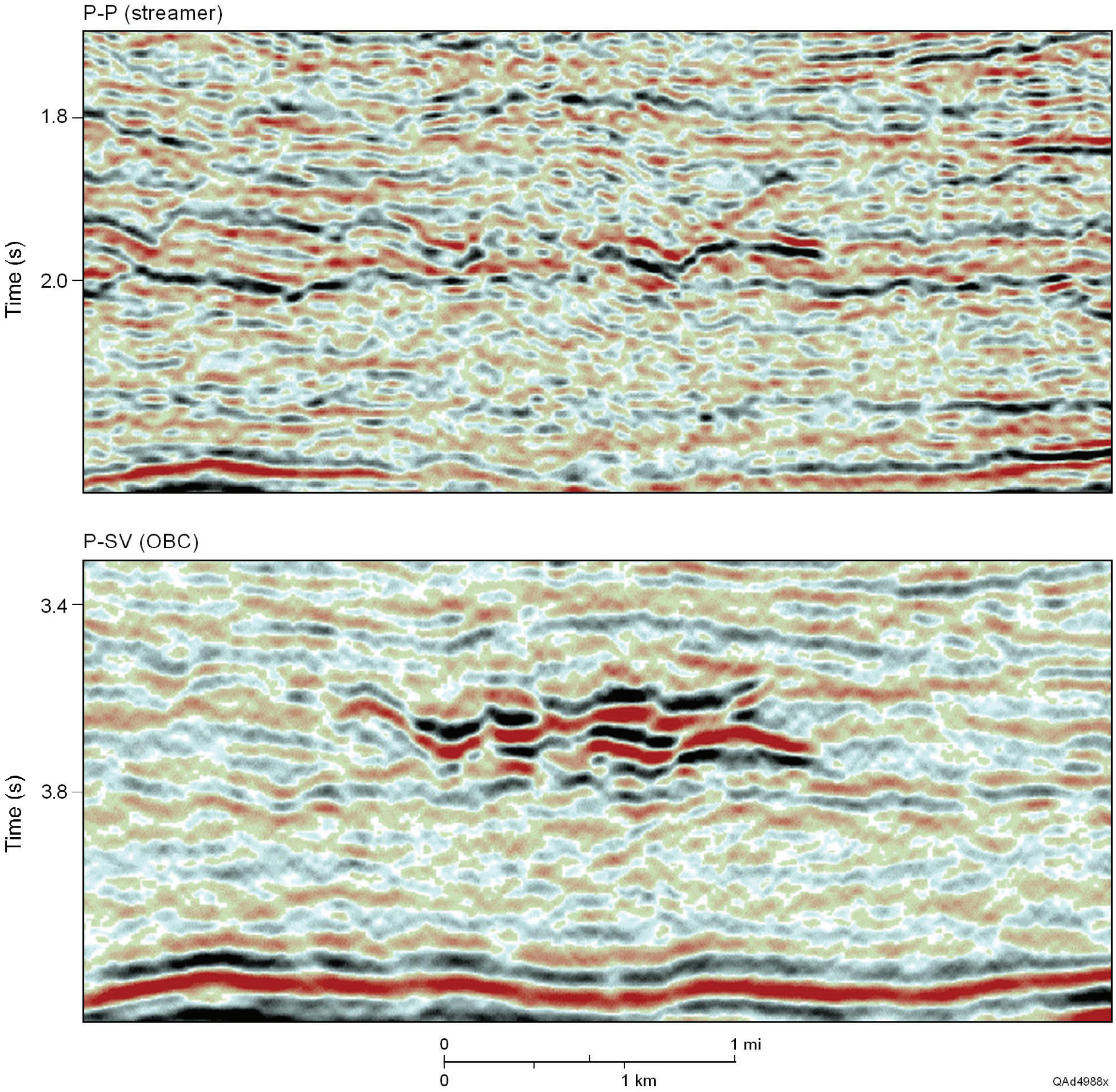

Figure 56. P-P and P-SV profiles across Alba field, North Sea. Modified from MacLeod and others (1999).

Some explorationists are now learning that multicomponent seismic data and elastic wavefield stratigraphy concepts are essential for imaging Class 2 reservoirs. A recent example of such an application is the 4C seismic survey done by Petrobras across its deep-water Roncador field in which P-SV data allowed an important Class 2 reservoir that could not be seen using P-P data to be exploited (Cafarelli and others, 2006).

Rock Physics

Well log data across the Alba reservoir target are displayed in Figure 57. To illustrate P-P and P-SV reflectivities associated with this target, we represented the reservoir by a two-layer Earth model defined by averaging these log data. The upper seal layer of the reservoir was assigned log-averaged properties: V_P = 2,470 m/s, V_S = 915 m/s, and ρ_b = 2.16 gm/cm^3. The reservoir interval was assigned log-averaged properties: V_P = 2,560 m/s, V_S = 1,370 m/s, and ρ_b = 2.10 gm/cm^3. Resulting reflectivity responses are shown in Figure 58.

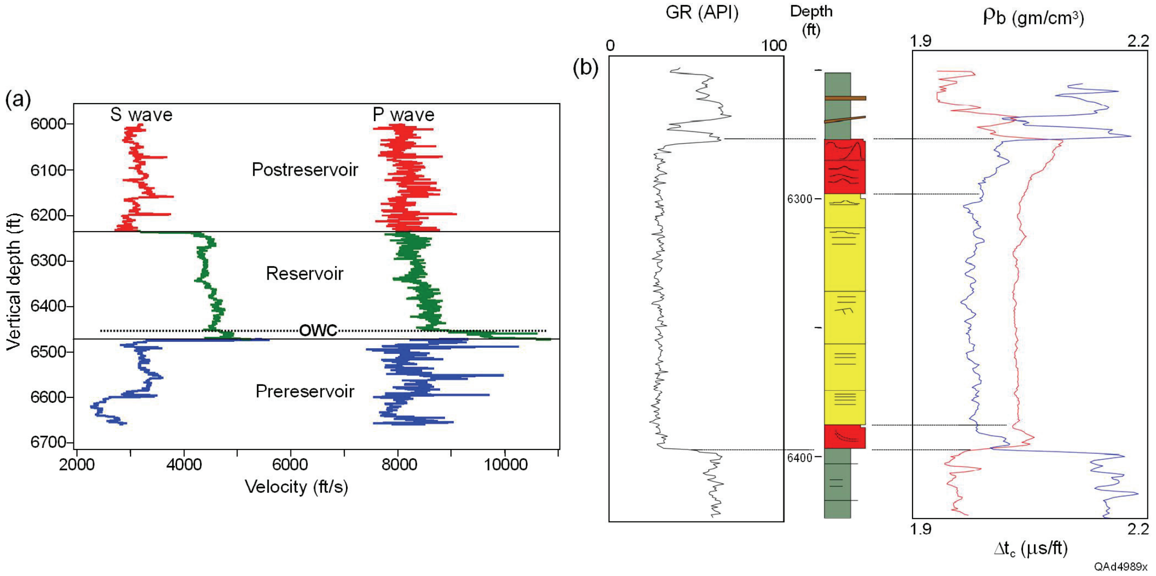

Figure 57. Well log data across the Alba reservoir interval. (a) V_P and V_S velocity logs from MacLeod and others (1999). (b) Density log from Duranti and others (2000).

The P-P and P-SV reflectivity curves have near-zero and zero values, respectively, at normal incidence and then slope toward negative values. As the incidence angle increases, P-SV reflectivity reaches a magnitude of -5 percent quickly at an incidence angle of approximately 8° and continues to increase to almost -15 percent at an incidence angle of approximately 30°. In contrast, P-P reflectivity does not reach a magnitude of -5 percent until the incidence angle is almost 30°. The implication is that P-SV reflections from the Alba reservoir (and from all Class 2 reservoirs in general) are much more robust than P-P reflections at all angles of incidence (Fig. 56). Cafarelli and others (2006) reported this same P-P and P-SV imaging behavior across Roncador field, offshore Brazil. An important conclusion is that elastic wavefield stratigraphy allows exploitation of Class 2 reservoirs that cannot be exploited using conventional (P-P) seismic stratigraphy.

Note that P-P and P-SV reflectivities in Figure 58 have the same algebraic sign. This behavior is atypical. Usually P-P and P-SV reflectivities have opposite algebraic signs (Figures 27, 29, 34, 39, 40, 54). This wave physics allows some Class 2 reservoirs to be mapped using elastic wavefield stratigraphy by first depth equalizing P-P and P-SV images to define a stratigraphic interval where Class 2 reservoirs are expected and then mapping areas (1) where P-P and P-SV reflections are the same polarity (a Class 2 target) and (2) where P-P and P-SV reflections are opposite polarities (non-Class 2 conditions). This approach to exploiting Class 2 reservoirs cannot be done in conventional seismic stratigraphy.

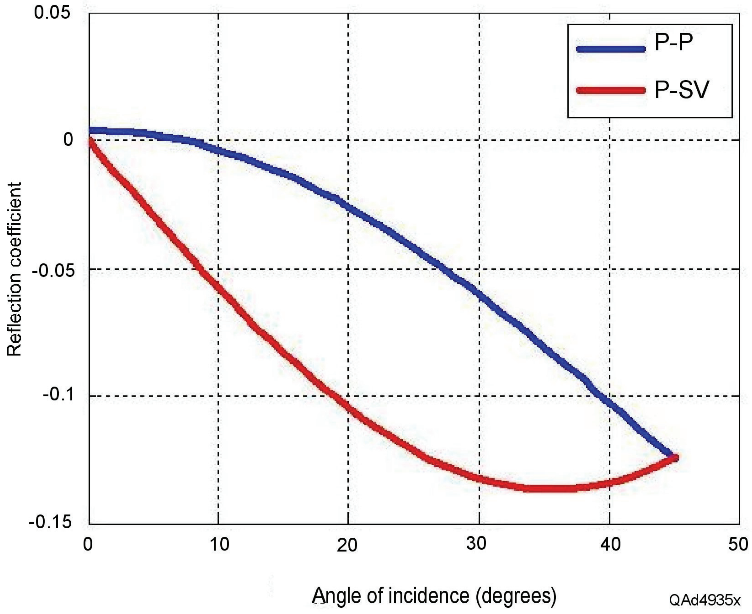

Figure 58. P-P and P-SV AVA responses across the top of the Alba reservoir.

Gas-Charged Sediments

One hydrocarbon exploration application that has caused multicomponent seismic data to be acquired across several offshore areas is the ability of the S-wave mode to image geology inside broad, thick intervals of gas-charged sediment where P-P seismic data show no usable reflections. The term ***P-wave wipeout zone*** is often used to describe this imaging problem. Numerous examples of P-wave and S-wave images across P-wave wipeout zones have been published, but the rock-physics cause of the P-P imaging problem has not been adequately documented. This report would not be a proper discussion of advantages of elastic wavefield stratigraphy over conventional seismic stratigraphy if we did not include comments on applications of elastic wavefield stratigraphy to geological interpretations across intervals of thick, gas-charged sediments. We take a different tack in this discussion than what appears in the literature in that (1) we analyze the rock-physics basis causing differences observed in P and S imaging through gas-charged layers, and (2) we consider two types of gas-charged targets: (a) one in which sediment remains lithified and stratified and (b) one in which the sediment is mobilized.

P and S Sequences and Facies

Lithified and stratified sediment

To date, published examples of differences between P-P and P-SV images of gas-charged sediment have illustrated situations in which sediment within the wipeout zone is lithified and stratified. An example of such imaging from one of the 4C OBC surveys available for this study is shown as Figure 59.

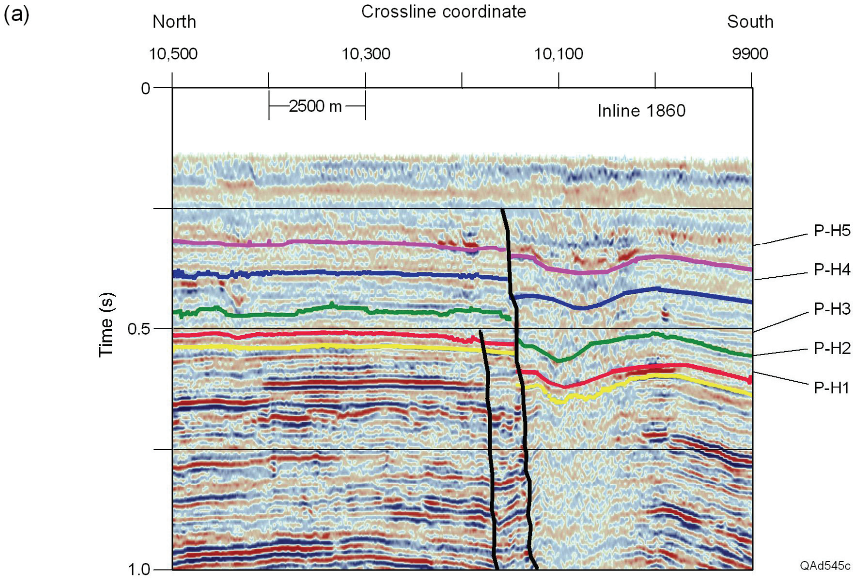

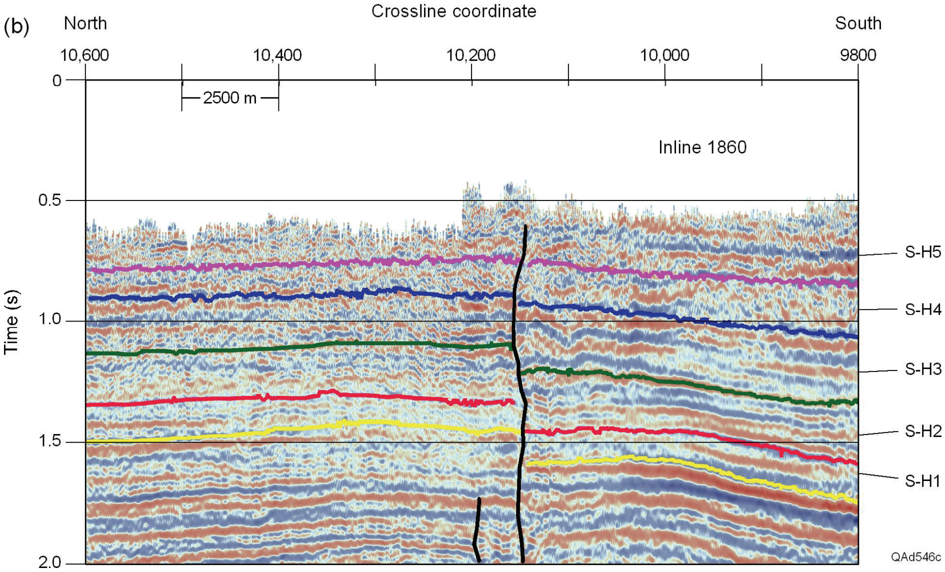

Figure 59. (a) P-P image and (b) P-SV image across gas-charged GOM sediments that are lithified and stratified. P-P horizons P-H1 through P-H5 are interpreted to be depth equivalent to P-SV horizons S-H1 through S-H5. The P-SV data image stratigraphy inside the P-wave wipeout zone extending from CDP coordinates 10,000 to 10,150.

Visual inspection of these images shows that the P-P mode provides poor, limited information about geological structure, depositional sequences, and sedimentary facies inside the image space dominated by gas-charged sediment (CDP coordinates 10,000 to 10,150). Conventional seismic stratigraphy (P-P mode only) would have little success in analyzing geological conditions within this poor-quality P-P image area. In contrast, the P-SV mode provides an image that is sufficient for structural mapping, as well as for analyzing seismic sequences and seismic facies. Both of these interpretation options are obvious advantages of elastic wavefield stratigraphy over conventional seismic stratigraphy in areas having gas-charged sediment.

Mobilized sediment

At numerous locations across the GOM, there is a second type of P-wave wipeout zone that involves gas-charged sediment that is fluidized and mobilized, not lithified and stratified. An example of a volume of mobilized gas-charged sediment is labeled *Expulsion chimney* in Figure 44. In this example, both P-P and P-SV mode fail to image parts of this vertical feature in which gas-charged sediment is continuously moving up to the seafloor and forming localized seafloor mounds and debris flows. In those regions of this gas-charged sediment where the P-SV mode fails to produce an image, the seismic propagation medium is assumed to be homogeneous and to have no stratal surfaces that can produce a reflection event. For this particular type of gas-charged sediment, elastic wavefield stratigraphy has no advantage over conventional seismic stratigraphy. Both seismic interpretation methods fail because no elastic mode propagating through sediment that is continuously moving and repeatedly destroying its internal stratal surfaces can produce usable reflection signals from the interior of the mobile sediment.

Rock Physics

Our evaluation of published attenuation theories for propagating P-P and P-SV modes has not shown a dramatic difference between P-P and P-SV attenuations in gas-charged sediments. Developing appropriate attenuation models will be ongoing research. For the present, we conclude that standard reflectivity analysis is sufficient to explain why P-P modes provide poor images in gas-charged sediment but P-SV modes do not.

A simple Earth model consisting of a shale layer atop a sand layer was used to evaluate P-P and P-SV reflectivity behaviors for types of siliciclastic rocks that occur in the GOM where P-wave wipeout zones are common (Fig. 59). Two pore-fluid situations were modeled: (1) both layers had 100 percent brine saturation, and (2) both layers had a mixed pore fluid of 80 percent brine and 20 percent gas. The theory described by Castagna and others (1993) was used to develop V_P-to-V_S and V_P-to-ρ_b relationships for the 100 percent brine situation. Gassmann's (1951) theory was then used to alter pore fluid from 100 percent brine to a homogeneous 80/20 mix of brine and gas. Specific petrophysical properties used in the modeling were

	Shale (100% brine)	Shale (20% gas)	Sand (100% brine)	Sand (20% gas)
V_P	3534 m/s	3188 m/s	3500 m/s	3370 m/s
V_S	1990 m/s	1994 m/s	1827 m/s	1847 m/s
ρ_b	2.45 gm/cm^3	2.44 gm/cm^3	2.207 gm/cm^3	2.16 gm/cm^3

P-P and P-SV reflectivity curves for these two pore-fluid conditions are shown in Figure 60. When pore fluid is 100 percent brine, P-P and P-SV reflectivities are approximately the same average magnitude (~5 percent) for incidence angles ranging from 0 to 25° (panel a). When pore fluid changes to 20 percent gas (panel b), P-SV reflectivity is unchanged, but P-P reflectivity has a smaller magnitude and undergoes a phase reversal that essentially eliminates P-P response across the first 25° of the incidence-angle range. P-SV imaging is thus not affected by the gas-charged sediment, but P-P imaging is seriously degraded. The effect would be similar to that exhibited by the data in Figure 59. In summary, elastic wavefield stratigraphy is not just helpful for studying geological conditions across P-wave wipeout zones, but is essential.

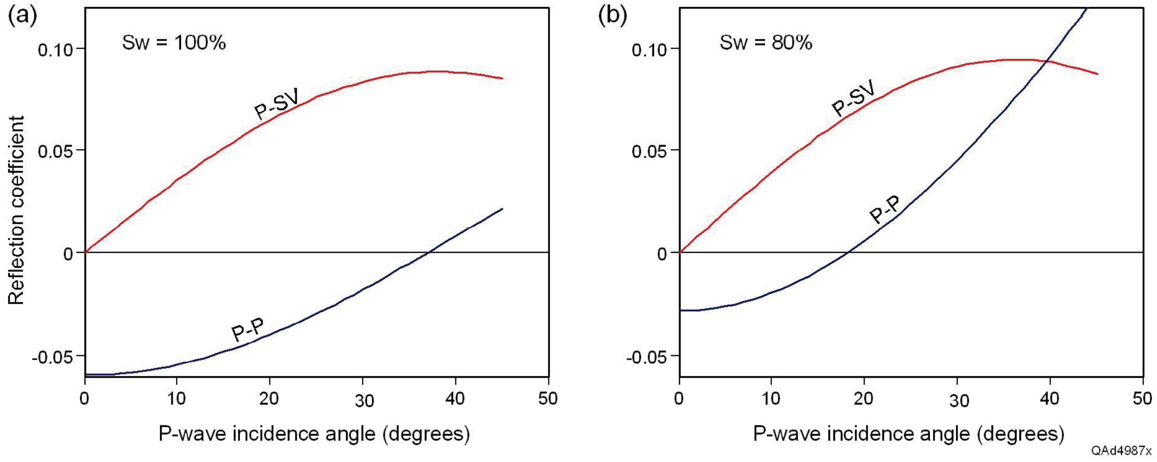

Figure 60. P-P and P-SV reflectivities for (a) brine-filled and (b) gas-charged sediments.

Conclusion

The importance of seismic stratigraphy in oil and gas applications cannot be overstressed. Concepts that seismic reflection events image stratal surfaces and that these stratal surfaces then allow geologically and geophysically distinct sequences and facies to be interpreted and mapped are practiced daily by the worldwide geoscience community. Although seismic stratigraphy is a well-structured science and is practiced throughout industry and academe, use of the technology has suffered from the fact that seismic stratigraphy concepts have been applied by many seismic interpreters only to conventional P-P seismic data.

Technology developed in this research expands seismic stratigraphy to the full elastic wavefield and provides interpreters more information about rock and pore-fluid facies. In elastic wavefield stratigraphy, a partial elastic wavefield involves only 3-component or 4-component seismic data and requires an interpretation of only P-P and P-SV modes. In contrast, a full elastic wavefield requires 9-component seismic data and consists of P-P, P-SV, SH-SH, SV-SV, and SV-P events. The elastic wavefield stratigraphy technology described here demonstrates that each of these reflected wave modes (P-P, P-SV, SH-SH, SV-SV, and SV-P) has equal value for seismic stratigraphy analyses and that the seismic sequences and seismic facies associated with each seismic mode often provide rock and pore-fluid information not found in the other wave modes.

We have made our investigation as comprehensive as possible by interpreting elastic wavefield data acquired in both marine and onshore environments, considering 3C, 4C, and 9C multicomponent seismic data, analyzing both deep and shallow targets, and studying both carbonate and siliciclastic systems. Each example of an elastic wavefield stratigraphy application that we have presented is supported by rock-physics analysis that illustrates how seismic wave modes react to that particular rock facies. Principles established by these rock-physics models are essential to our understanding of the increased geological information provided by elastic waves other than the P-P mode.

Acknowledgments

Seismic data used in this study were provided by WesternGeco, Devon, Seitel Data, Fasken Oil and Ranch, and Vecta Technology.

References

Aki, K., and Richards, P. G., 1980, Quantitative seismology—theory and methods: San Francisco, W. H. Freeman and Co., 700 p.

Backus, G., 1962, Long-wave elastic anisotropy produced by horizontal layering: Journal of Geophysical Research, v. 76, p. 4427–4440.

Backus, M. M., Murray, P. E., Hardage, B. A., and Graebner, R. J., 2006, High-resolution multicomponent seismic imaging of deepwater gas-hydrate systems: The Leading Edge, v. 25, No. 5, p. 578–596.

Bates, R. L., and Jackson, J. A., 1980, Glossary of geology: American Geological Institute, 749 p.

Berg, O. R., and Woolverton, D. G. eds., 1985, Seismic stratigraphy II—an integrated approach: American Association of Petroleum Geologists Memoir 39, 276 p.

Brown, L. F., and Fisher, W. L., 1977, Seismic stratigraphic interpretation of depositional systems—examples from Brazilian rift and pull-apart basins, *in* American Association of Petroleum Geologists Memoir 26, p. 213–248.

Cafarelli, B., Randazzo, S., Campbell, S., Fernandes Sobreira, J., Gallotti Guimaraes, M., Rodriguez, C., Johann, P., and Theodoro, C., 2006, Ultra-deep 4C offshore Brazil: The Leading Edge, v. 25, p. 474–477.

Castagna, J. P., Batzle, M. L., and Kan, T. K., 1993, Rock-physics—the link between the rock properties and AVO response, *in* Castagna, J. P., and Backus, M. M., eds., Offset-dependent reflectivity-theory and practice of AVO analysis: Tulsa, Society of Exploration Geophysicists.

Castagna, J. P., Swan, H.W., and Foster, D. J., 1998, Framework for AVO gradient and intercept interpretation: Geophysics, v. 63, p. 948–956

Davis, T. L., 1984, Seismic stratigraphic facies models: Geoscience Canada, Reprint Series 1, p. 311–317.

DeAngelo, M., Backus, M., Hardage, B., Murray, P., and Knapp, S., 2003, Depth registration of P-wave and C-wave seismic data for shallow marine sediment characterization, Gulf of Mexico: The Leading Edge, v. 22, no. 2, p. 96–105.

Duranti, D., Hurst, A., Hanson, R., Bell, C., and McLeod, M., 2000, Reservoir characterization of a remobilized sand-rich turbidite reservoir—the Alba field, *in* EAGE 62nd Conference and Technical Exhibition, Expanded Abstracts, Glasgow, Scotland.

Ensley, R. A., 1984, Comparison of P- and S-wave seismic data—a new method for detecting gas reservoirs: Geophysics, v. 49, p. 1420–1431.

Ensley, R. A., 1985, Evaluation of direct hydrocarbon indicators through comparison of compressional and shear wave seismic data—a case study of the Myrnam gas field, Alberta: Geophysics, v. 50, p. 37–48.

Fomel, S., Backus, M., DeAngelo, M., Murray, P., and Hardage, B., 2003, Multicomponent seismic data registration for subsurface characterization in the shallow Gulf of Mexico, *in* Offshore Technology Conference, Paper OTC 15117, Houston, May.

Gassmann, F., 1951, On the elasticity of porous media: Vier. Der Natur. Geslischft in Zurich, v. 96, p. 1–23.

Han, D. H., Nur, A., and Morgan, D., 1986, Effects of porosity and clay content on wave velocities in sandstones: Geophysics, v. 51, p. 2093–2107.

Hanson, R., Condon, P., Behrens, R., Groves, S., and MacLeod, M., 2003, Analysis of time-lapse data from the Alba field 4C/4D seismic survey: Petrological Geoscience, v. 9, no. 1, p. 103–111.

Hardage, B. A., 1987, Seismic stratigraphy: Amsterdam, Elsevier Science, 432 p.

Hardage, B. A., DeAngelo, M., and Murray, P. E., 2003, Defining P-wave and S-wave stratal surfaces with nine-component VSPs: The Leading Edge, v. 22, no. 8, p. 720–729.

Hudson, J. A., 1981, Wave speeds and attenuation of elastic waves in materials containing cracks: Geophysical Journal of the Royal Astronomical Society, v. 64, p. 133–150.

Lynn, H. B., 2004, The winds of change—anisotropic rocks—their preferred direction of fluid flow and their associated seismic signatures, part 1 and part 2: The Leading Edge, v. 23, no. 11, p. 1156–1162 (part 1) and v. 23, no. 12, p. 1258–1268 (part 2).

MacLeod, M. K., Hanson, R. A., Bell, C. R., and McHugo, S., 1999, The Alba field ocean bottom cable seismic survey: impact on development, *in* Offshore European Conference, SPE 56977.

McCormack, M. D., Dunbar, J. A., and Sharp, W. W., 1984, A case study of stratigraphic interpretation using shear and compressional seismic data: Geophysics, v. 49, p. 509–520.

McCormack, M. D., Justice, M. G., and Sharp, W. W., 1985, A stratigraphic interpretation of shear and compressional wave seismic data for the Pennsylvanian Morrow formation of southeastern New Mexico: American Association of Petroleum Geologists, Memoir 39, p. 225–239

Meissner, R. and Hegazy, M. A., 1981, The ratio of the PP to the SS reflection coefficient as a possible future method to estimate oil and gas reservoirs: Geophysical Prospecting, v. 29, p. 533–540.

Mitchum, R. M., Jr., 1977, Seismic stratigraphy and global changes of sea level, part 11, glossary of terms used in seismic stratigraphy: American Association of Petroleum Geologists, Memoir 26, p. 205–212.

Mitchum, R. M. and Vail, P. R., 1977, Seismic stratigraphy and global changes of sea level, part 7, Seismic stratigraphic interpretation procedure: American Association of Petroleum Geologists, Memoir 26, p. 135–144.

Mitchum, R. M., Jr., Vail, P. R., and Sangree, J. B., 1977a, Seismic stratigraphy and global changes in sea level, part 6, Stratigraphic interpretation of seismic reflection patterns in depositional sequences: American Association of Petroleum Geologists, Memoir 26, p. 117–133.

Mitchum, R. M., Vail, P. R., and Thompson, S., 1977b, Seismic stratigraphy and global changes of sea level, part 2, The depositional sequence as a basic unit for stratigraphic analysis: American Association of Petroleum Geologists, Memoir 26, p. 53–62.

Payton, C. E., ed., 1977, Seismic stratigraphy—applications to hydrocarbon exploration: American Association of Petroleum Geologists, Memoir 26, 516 p.

Roden, R., Forrest, M., and Holeywell, R., 2005, The impact of seismic amplitudes on prospect risk analysis: The Leading Edge, v. 24, p. 706–711.

Roksandic, M. M., 1978, Seismic facies analysis concepts: Geophysical Prospecting, v. 26, p. 383–398.

Ruger, A., 2002, Reflection coefficients and azimuthal AVO analysis in anisotropic media: Geophysical Monograph Series Number 10 (series editor D. V. Fitterman; volume editors K. Larner and I. Tsvankin): Tulsa, Society of Exploration Geophysicists, 189 p.

Rutherford, S. R. and Williams, R. H., 1989, Amplitude-versus-offset variations in gas sands: Geophysics, v. 54, p. 680–688.

Sangree, J. B. and Widmier, J. M., 1977, Seismic stratigraphy and global changes of sea level, part 9, Seismic interpretation of clastic depositional facies: American Association of Petroleum Geologists, Memoir 26, p. 165–184

Sangree, J. B. and Widmier, J. M., 1979, Interpretation of depositional facies from seismic data: Geophysics, v. 44, p. 616–619.

Sava, D., and Hardage, B., 2006, Rock physics characterization of hydrate-bearing deepwater sediments: The Leading Edge, v. 25, p. 616–619.

Sheriff, R. E., 1980, Seismic stratigraphy: Boston, International Human Resources Development Corp., 277 p.

Tipper, J. C., 1993, Do seismic reflections necessarily have chronostratigraphic significance?: Geological Magazine, v. 130, p. 47–55.

Vail, P. R., Todd, R. G., and Sangree, J. B., 1977, Seismic stratigraphy and global changes of sea level, part 5, Chronostratigraphic significance of seismic reflections: American Association of Petroleum Geologists, Memoir 26, p. 99–116.

Zeng, H., 2001, From seismic stratigraphy to seismic sedimentology: a sensible transition: Gulf Coast Association of Geological Societies Transactions, v. 51, p. 412–420.

Zeng, H., 2006, Stratal slicing makes seismic imaging of depositional systems easier: AAPG Explorer, v. 27, no. 6, p. 26–27.

Zoeppritz, K., 1919, Erdbebenwellen VIIIB, On the reflection and propagation of seismic waves: Gottinger Nachrichten, I, p. 66–84.